NCNR Highlights 2007

The New BT-7 Thermal Triple Axis Spectrometer

J. W. Lynn, Y. Chen, M. Murbach, C. Wrenn, C. Brocker, N. Maliszewskyj, J. Ziegler[1]

A major milestone was achieved in the modernization of the NCNR's thermal neutron instruments with the installation and commissioning of the new multi-mode analyzer system on the thermal triple-axis spectrometer (TAS) at the BT-7 beam port. The installation of the new analyzer system completes the basic construction of the new instrument, which is shown in operation in Fig. 1.

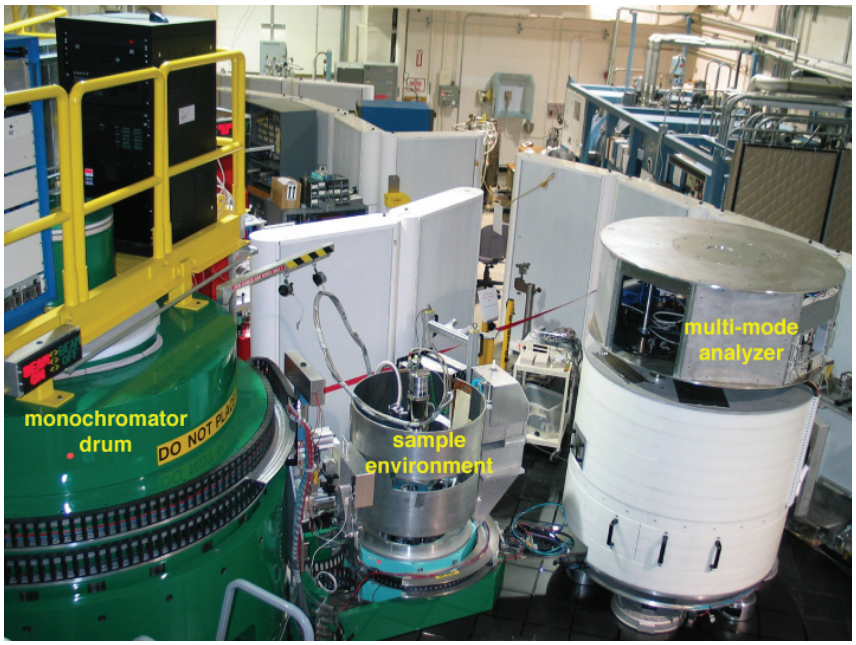

FIGURE 1: Picture of the BT-7 thermal triple axis instrument in operation.

The green drum houses the double focusing monochromator system, with a choice of PG(002) or Cu(220) crystals that provide a continuous incident energy range from 5 meV to 500 meV. The 400 cm^2 reflecting area of each monochromator yields as much as an order-of-magnitude gain of neutrons onto the sample compared with other thermal triple-axis spectrometers at the NCNR. The reactor beam and post monochromatic beam elements (collimators, slits, and filters) offer a wide range of choices to optimize the resolution and intensity of the instrument, with flux onto the sample as high as $2 \cdot 10^8$ $n/cm^2/s$. The sample stage allows a wide variety of sample environments to be used—refrigerators, cryostats, furnaces, and magnets. The instrument includes two coaxial rotary tables, one for sample rotation and one for the independent rotation of magnetic field coils, and a computer-controlled sample goniometer and elevator.

The white drum is the new analyzer, which is shown schematically in Fig. 2. The pyrolitic graphite (PG) crystal (002) analyzer array consists of 13 individual blades that can be used in flat or horizontally focusing configurations in combination with a linear position sensitive detector or conventional Söller collimators. An array of 11 detectors embedded in the door behind the analyzer continuously monitors the neutron flux entering the analyzer to check for intense scattering from the sample that might give rise to a spurious count rate in the detector.

The analyzer system has five basic modes of operation that are computer-controlled and can be selected and interchanged by the experimenter without requiring any mechanical reconfiguration or hands-on user intervention inside the analyzer housing. The simplest mode places a separate diffraction detector in front of the crystal analyzer, to align the scattering angle or to make conventional Bragg peak intensity measurements.

A second mode is the "standard" triple-axis configuration in which the analyzer is used in the flat configuration with Söller collimators before and after the analyzer. One additional feature is that the door detectors can then

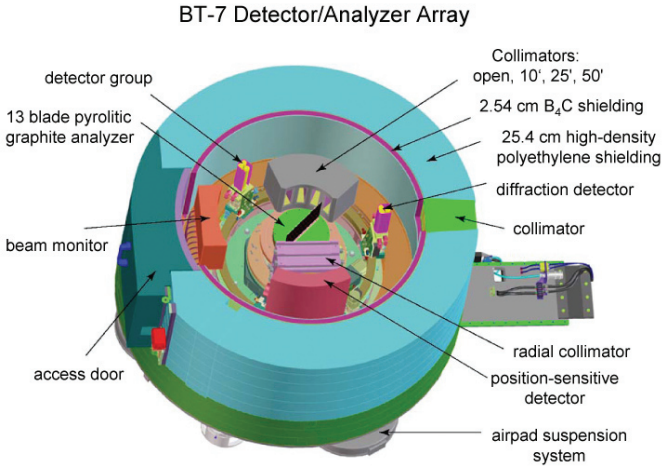

FIGURE 2: Schematic diagram of the new analyzer system for the BT-7 thermal triple axis spectrometer.

[1]NIST Center for Neutron Research, National Institute of Standards and Technology, Gaithersburg, MD 20899

be used to simultaneously determine the instantaneous correlation function. A third mode (manually) places a radial collimator in the sample-to-analyzer (S-A) position and the position-sensitive detector (PSD) in the straight-through position to provide a simultaneous measurement of the scattering along an arc in reciprocal space for single crystal specimens, which will greatly accelerate making maps of diffuse scattering, for example, or may be used to monitor the intensity and position of a Bragg peak associated with a magnetic or structural phase transition.

Alternatively, for a powder specimen a measurement of the diffraction pattern over a range of angles can be obtained simultaneously. This will greatly reduce the time to obtain a (coarse resolution) diffraction pattern, or can be used to quickly measure the integrated intensity of a Bragg peak associated with a magnetic or structural phase transition.

A fourth option is to use a radial S-A collimator and the PG array in horizontal energy focusing mode with either the single detector or PSD depending of the measurement needs. For problems where the analyzer resolution can be relaxed this can more than triple the signal. Analyzer configurations other then energy focusing are also possible.

The fifth mode is to use open S-A collimation, a flat PG array, radial collimator after the crystal analyzer and the PSD to measure a range of ($\boldsymbol{Q}$, E) simultaneously. These five measurement capabilities provided by the new analyzer system greatly increase flexibility for the experimenter. Finally, we note that all these configurations can be utilized with ^{3}He polarizers before and after the sample, along with computer controlled polarization direction at the sample, to enable measurements of all eight of the conventional polarized neutron cross sections.

The electronic systems for the new instrument are distributed among its components. Controls for the primary spectrometer (beam conditioning, sample table, monochromator drum, double focusing monochromator, scattering angle) reside atop the monochromator drum. All controls for the secondary spectrometer (analyzer motors, detector electronics, airpad controls), on the other hand, are housed in an enclosure on the analyzer itself. The only physical connections of the analyzer system to the rest of the instrument are a mechanical coupling, compressed air (for the air-pad system), electrical power, and ethernet communications. The distributed nature of the electronics and the simple linkage of the analyzer to the primary spectrometer are designed to both alleviate heavy cabling burdens and to facilitate interchangeability of the analyzer. In particular, if a different type of analyzer capability is required, such as a double focusing array with a detector buried in shielding, an analyzer with a different crystal choice, or a multi-crystal/multi-detector array, then the separate analyzer can be installed by floating it in on air pads, attaching it to the scattering angle arm, and simply connecting power, air, and communications. The future development of additional types of analyzers will add

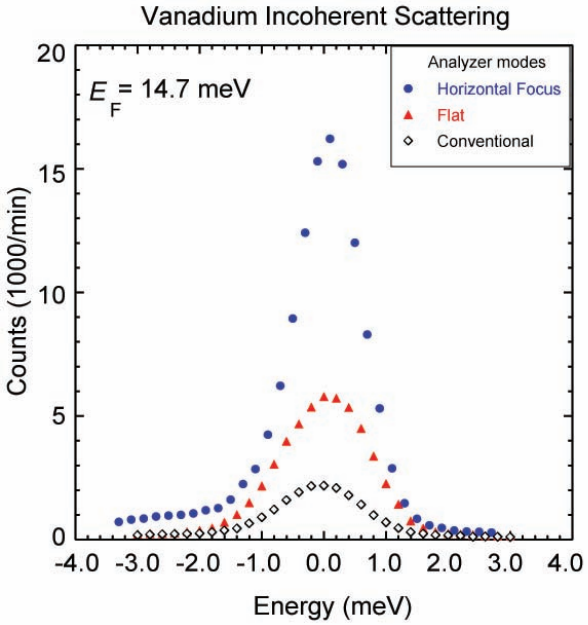

FIGURE 3: Energy scan through the incoherent scattering of a vanadium calibration sample, comparing the conventional analyzer with the new analyzer in flat mode, and with horizontal focusing.

important measurement capabilities both for the thermal as well as for the cold triple axis instruments.

Because of the high demand for thermal TAS measurement capability in the U. S. combined with the dearth of available instruments both in the U.S. as well as Europe during the last few years, the new instrument was pushed into service early by installing a conventional analyzer system to make the instrument operational as a triple-axis spectrometer in the interim. This affords a ready comparison to the dramatic improvement in performance with the new analyzer, as shown in Fig. 3.

With conventional Söller collimators before and after the analyzer, the improvement in performance is ≈ 2.4, which comes primarily from the increased analyzer/detector height. Relaxing the angular divergence by employing horizontal focusing mode provides a factor of 6.2 gain in signal. Overall improvement in performance of the entire instrument is one to two orders-of-magnitude in signal compared with traditional thermal triple axis spectrometers, depending on the type of measurement being performed. In addition, the fast-neutron background for the new instrument has been substantially improved compared to traditional TAS instruments. The new instrument provides a signal that is comparable to the best TAS instruments in the world, and a measurement flexibility that is unparalleled.

The Density Minimum in Deeply Supercooled Confined Water

D. Liu, Y. Zhang, S.-H. Chen[1]; C.-C. Chen, C.-Y. Mou[2]; P. H. Poole[3]

In this article we highlight a report of the first experimental evidence of the existence of the density minimum in supercooled water [1]. Using the NG-7 small angle neutron scattering (SANS) instrument at the NCNR, we measured the density of heavy water contained in 1-D cylindrical pores of mesoporous silica material MCM-41-S-15 having pores of diameter of (15 ± 1) Å. In these pores the homogenous nucleation process of bulk water at 235 K does not occur and the liquid can be supercooled down to at least 160 K. The analysis of SANS data allows us to determine the absolute value of the density of D_2O as a function of temperature. We observe a density minimum at (210 ± 5) K with a value of (1.041 ± 0.003) g/cm^3. We show that the results are consistent with the predictions of molecular dynamics simulations of supercooled bulk water.

The 17th century discovery of the density maximum in water at 4 °C demonstrates the long history of water science [2]. Incredibly, it took another 320 years to observe that water has a density *minimum* at an even lower temperature [1]. The reason may be that bulk

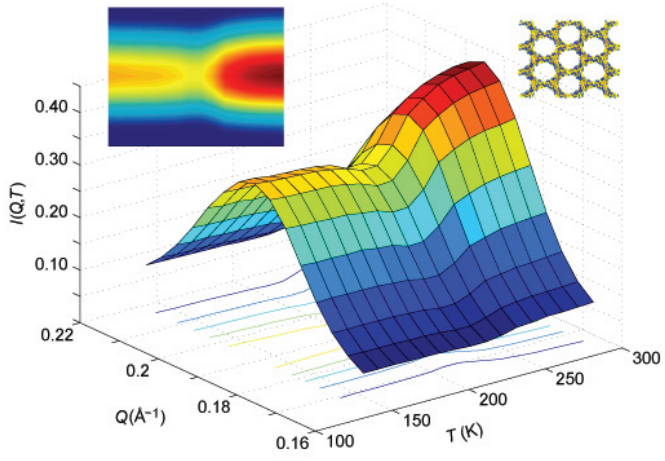

FIGURE 1: SANS intensity distribution as a function of *Q* and *T*. The peak in *I*-*Q* plane is due to Bragg diffraction of the 2-D hexagonal lattice in grains of the silica crystallites (right inset). The height of the diffraction peak is a quadratic function of the density of D_2O inside the cylindrical pore. The saddle point indicates the density minimum point of supercooled confined heavy water. The left inset shows a contour of the intensity surface.

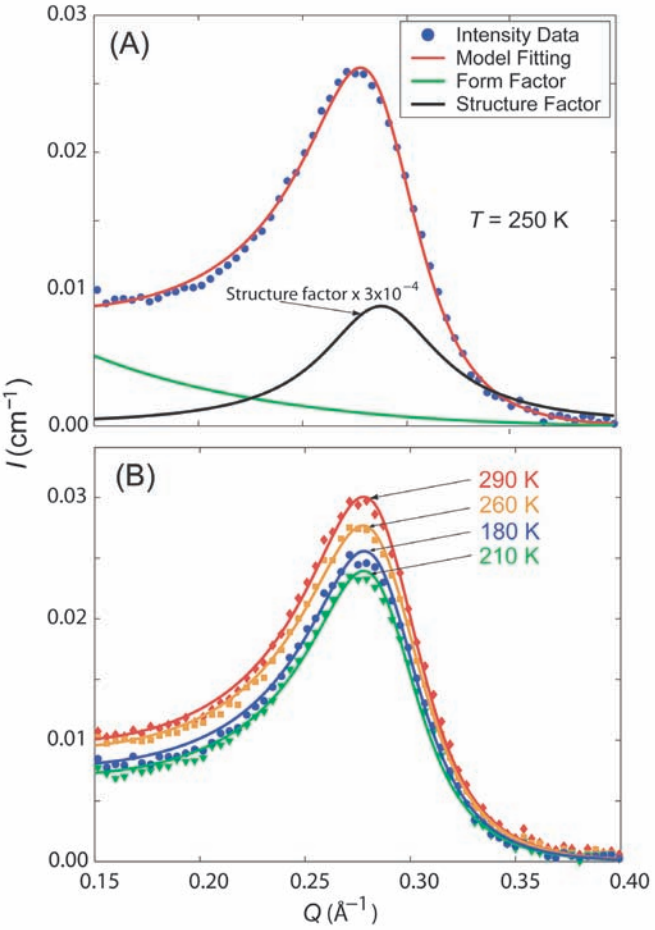

FIGURE 2: Model analysis of SANS intensity distribution. (A) The blue circles show the SANS data (at 250 K) with the contribution of the interfacial (surfaces of the grains) scattering subtracted. The red solid line represents the fitted curve using the model given in Ref. 1. The black line represents the structure factor *S*(*Q*) of the 2-D hexagonal lattice. The green line represents the form factor *P*(*Q*) of the cylindrical column tube of D_2O. (To make the figure clearer, the magnitude of *S*(*Q*) is multiplied by a factor 3x10^{-4}) . (B) SANS data and their fitted curves (solid lines) for different temperatures. Four curves are selected to show the good agreement between the model analyses and the experimental data.

[1]Massachusetts Institute of Technology, Cambridge, MA, 02139
[2]National Taiwan University, Taipei, Taiwan 106
[3]St. Francis Xavier University, Antigonish, Nova Scotia, B2G 2W5, Canada

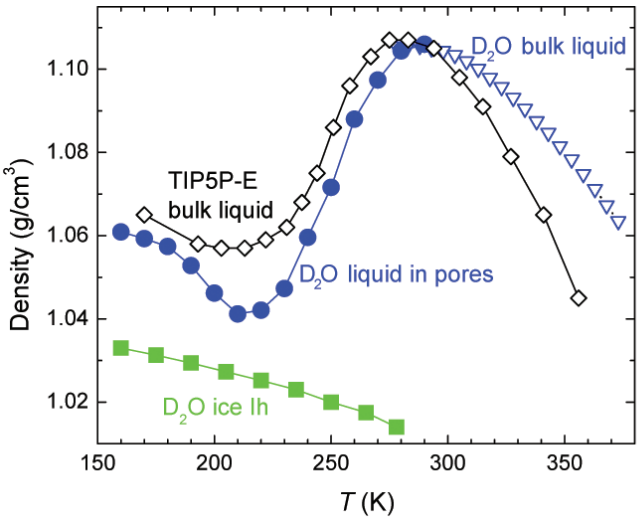

FIGURE 3: Comparison of density versus temperature curves at ambient pressure for bulk liquid D_2O (triangles) [CRC handbook], confined liquid D_2O (solid circles) from this work, D_2O ice Ih (solid squares), and MD simulations of liquid TIP5P-E water (open diamonds). The density values for the TIP5P-E model (which is parametrized as model of H_2O) have been multiplied by 1.1 to facilitate comparison with the behavior of D_2O.

water inevitably crystallizes into hexagonal ice below its melting point (at 0 °C) and so far it has not been possible to measure the density of bulk liquid water at the low temperature where the density minimum occurs. We have been able to bypass this difficulty by confining water and have demonstrated that if it is kept from freezing at this temperature there is a well-defined density minimum at 210 K in D_2O.

Our sample was a MCM-41-S-15 powder which is made of a micellar templated mesoporous silica matrix and has 1-D cylindrical pores arranged in a 2-D hexagonal lattice [3]. The sample was fully hydrated with D_2O for the measurement. In this experiment, we chose the material with a pore diameter of (15 ± 1) Å because differential scanning calorimetry data showed no freezing peak down to 160 K for the fully hydrated sample. Based on a detailed analysis of the SANS data, we find that the height of the Bragg peak of the hexagonal lattice is related to the scattering length density (SLD) of D_2O inside the silica pores. The SLD of D_2O is proportional to its mass density $\rho^m_{D_2O}$. Hence, we are able to determine the density of water (D_2O) by measuring the temperature-dependent neutron scattering intensity $I(Q)$ (see Fig. 1). Detailed analysis is illustrated in Fig. 2.

Consistent with these experimental results, a number of recent molecular dynamics (MD) computer simulation studies predict that a density minimum occurs in water (H_2O) (see Fig. 3) [4,5]. Compared to experiments on bulk water, these computer simulation studies achieve deep supercooling without crystal nucleation due to the small system size and short observation time explored.

The finding of a density minimum also has significant implications for the proposal that a liquid-liquid phase transition occurs in supercooled water [6]. These implications arise because a formal relationship exists between density anomalies and response functions, such as the isothermal compressibility K_T and the isobaric specific heat C_P. Our finding reinforces the plausibility that there is a Widom line emanating from the liquid-liquid critical point in supercooled water passing between T_{min} and T_{max}, as was indicated in our previous experiment [3] which detected the dynamic crossover phenomenon at 225 K at ambient pressure.

References

[1] D. Liu, Y. Zhang, C.-C. Chen, C.-Y. Mou, P. H. Poole, and S.-H. Chen, Proc. Natl. Acad. Sci., **104**, 9570 (2007).

[2] R. Waller, *Essays of Natural Experiments* (1684), (Johnson Reprint Corporation, New York, 1964)

[3] L. Liu, S.-H. Chen, A. Faraone *et al.*, Phys. Rev. Lett. **95**, 117802 (2005).

[4] D. Paschek, Phys. Rev. Lett. **94**, 217802 (2005).

[5] P. H. Poole, I. Saika-Voivoid and F. Sciortino, J. Phys: Condens. Matter **17**, L431 (2005).

[6] P. G. Debenedetti and H. E. Stanley, Physics Today **56**, No. 6, 40 (2003).

Hydrogen Absorption Properties of Metal-Ethylene Complexes

W. Zhou[1, 2]; T. Yildirim[1, 2]; E. Durgun[3], S. Ciraci[3]

The success of future hydrogen and fuel-cell technologies is critically dependent upon the discovery of new materials that can store a large amount of hydrogen at ambient conditions. The current obstacles in hydrogen storage are slow kinetics, poor reversibility and high dehydrogenation temperatures for the chemical hydrides, and very low desorption temperatures or energies for the physisorption materials. Recently, we have suggested a novel concept to overcome these obstacles [1-2]. We predicted that a single Ti atom affixed to carbon nanostructures (Fig. 1), such as C_{60} or nanotubes, strongly adsorbs up to four hydrogen molecules with a binding energy of 0.4 eV compatible with room temperature desorption/absorption. Unfortunately, synthesizing the predicted structures of Ti decorated nanotubes/C_{60} was proven to be very difficult. In searching for a more efficient and feasible high capacity hydrogen-storage medium, we found that the C=C double bond of an ethylene molecule C_2H_4, mimics double bonds of C_{60} that strongly binds the transition metal (TM) atom (see Fig. 1) and therefore it is expected to support TM atoms strongly to provide a basis for high-capacity hydrogen storage via the Dewar-Kubas mechanism. In this article, we highlight our exploration of this idea [3, 4].

Our results are obtained from first-principles plane wave calculations within density functional theory using Vanderbilt-type ultrasoft pseudopotentials with Perdew-Burke-Ernzerhof exchange correlation. Single molecules have been treated in a supercell of (20 × 20 × 20) Å^3 with Γ *k*-point and a cutoff energy of 408 eV.

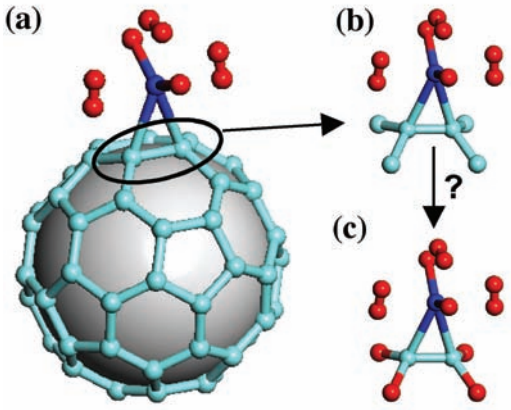

FIGURE 1: (a) One of the most stable structures of the Ti-C_{60} complex, where the Ti atom (dark blue) is bonded to a C-C double bond with four hydrogen molecules attached (red). (b) The local structure of the Ti-C_{60} double bond. (c) Replacing the end carbon atoms shown in (b) by H results in an ethylene molecule. This suggests that we may simply use the ethylene molecule to hold Ti atoms, which then binds multiple hydrogen molecules.

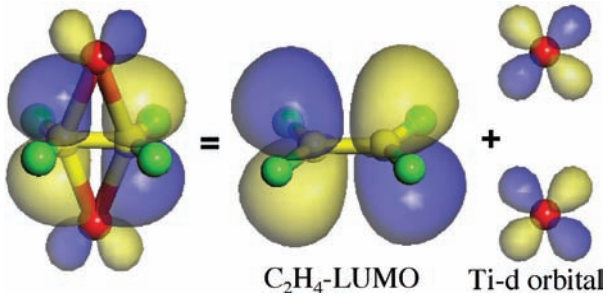

FIGURE 2: Optimized structure of an ethylene-Ti complex, $C_2H_4Ti_2$, showing that Ti-C_2H_4 bonding orbital results from the hybridization of the LUMO of the C_2H_4 and the Ti-*d* orbital, in accord with Dewar coordination.

We first studied the bonding of a single Ti-atom to an ethylene molecule to form C_2H_4Ti. We found no energy barrier for this reaction. The Ti atom forms a symmetric bridge bond with the C=C bond of ethylene with $E_B = 1.45$ eV. Interestingly, it is also possible to attach a second Ti atom to the C_2H_4Ti to form $C_2H_4Ti_2$ (Fig. 2) without any potential barrier and about the same binding energy as the first Ti atom. Figure 2 shows that the bonding orbital for the Ti atoms and C_2H_4 results from the hybridization of the lowest-unoccupied molecular orbital (LUMO) of the ethylene molecule and the Ti-*d* orbitals, in accord with Dewar coordination.

We next studied the H_2 storage capacity of the Ti ethylene complex by calculating the interaction between $C_2H_4Ti_2$ and a different number of H_2 molecules and configurations. The first H_2 molecule is absorbed dissociatively to form $C_2H_4(TiH_2)_2$ as shown in Fig. 3(a) with a binding energy of 1.18 eV/H_2. The additional hydrogen molecules do not dissociate and molecularly absorbed around the Ti atom. Two of these configurations are shown in Figs. 3(b) and 3(c). In the $C_2H_4(TiH_2\text{-}2H_2)_2$ configuration, two H_2 are molecularly bonded from the left and right side of the TiH_2 group with a binding energy of 0.38 eV/H_2 and significantly elongated H-H bond length of 0.81 Å. It is also energetically favorable to add a third H_2 molecule from the top of the TiH_2 group, with a binding energy of 0.4 eV and bond length of 0.82 Å. The resulting structure, $C_2H_4(TiH_2\text{-}3H_2)_2$, is shown in Fig. 3(c). We note that these binding energies have the right order of magnitude for room temperature storage. Since the hydrogens

[1]NIST Center for Neutron Research, National Institute of Standards and Technology, Gaithersburg, MD 20899
[2]University of Pennsylvania, Philadelphia, PA 19104
[3]Bilkent University, Ankara 06800, Turkey

	Li	Sc	Ti	V	Cr	Mn	Fe	Co	Ni	Cu	Zn	Zr	Pd	Pt
$E_B(M)$	0.70	1.39	1.45	0.94	0.18	0.51	0.92	1.39	0.91	0.80	–	1.91	1.95	2.52
E_B (per H_2)	0.28	0.28	0.46	0.53	0.21	0.18	0.34	0.28	0.42	0.33	–	0.54	0.27	0.25
max H_2/M	2	5	5	5	5	5	5	3	2	2	–	5	2	2

TABLE 1: The metal-C_2H_4 binding energies (E_B in eV/M atom) with respect to atomic energies of various metals, and the average H_2 binding energies (in eV/H_2) on C_2H_4M for maximum number of H_2 molecules bonded to each metal.

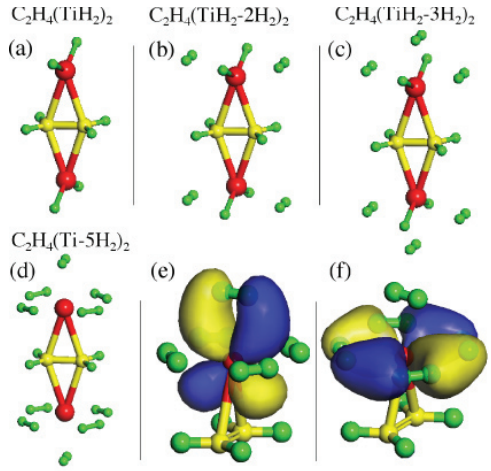

FIGURE 3: Atomic configurations of an ethylene molecule functionalized by two Ti atoms, holding (a) two H_2 molecules which are dissociated, (b) six H_2 molecules, and (c) eight H_2 molecules. Panel (d) shows a configuration where ten H_2 are bonded all molecularly. The panel (e) and (f) shows the bonding orbital for the top (e) and side hydrogen molecules, respectively. Note that the hydrogen σ^*-antibonding orbitals are hybridized with Ti-*d* orbitals, suggesting Kubas interaction for the H_2-Ti bonding.

are absorbed molecularly, we also expect fast absorption or desorption kinetics.

Finally, we also observed many other local stable configurations where all of the hydrogen molecules are bonded molecularly. One such configuration, denoted as $C_2H_4(Ti\text{-}5H_2)_2$, is shown in Fig. 3(d). Here the H_2 molecules stay intact and benefit equally from bonding with the Ti atom. The total of ten hydrogen molecules absorbed by a single Ti-ethylene complex, $C_2H_4(Ti\text{-}5H_2)_2$, corresponds to a mass fraction of ≈ 14 %.

The top hydrogen molecule in $C_2H_4(Ti\text{-}5H_2)_2$ has the weakest bonding in the system with E_B = 0.29 eV, whereas the side H_2 molecules have the strongest bonding with E_B = 0.49 eV/H_2 and significantly elongated H-H bond distance of 0.85 Å . This suggests the presence of two different H_2-$C_2H_4Ti_2$ bonding orbitals as shown in Figs. 3(e) and 3(f). The first one is a hybridization of the top-H_2 σ^*-antibonding with the Ti-*d* orbital. The second one is the simultaneous hybridization of the side H_2 σ^*-antibonding orbitals with the Ti-*d* orbital. Since the bonding orbitals are mainly between metal d- and hydrogen σ^*-antibonding orbitals, the mechanism of this interesting interaction can be explained by the Kubas interaction.

It is important to know if the above results for *M* = Ti hold for other metals. We studied [4] a large number of them, including the light metal Li. The results are summarized in Table I. Scandium is the ideal case, but for practical reasons Ti is the best choice. Cr binds very weakly while Zn does not bind at all to the C_2H_4 molecule. Heavier metals such as Pd and Pt can also form complexes with C_2H_4, but bind fewer hydrogen molecules with significantly stronger binding energy than Ti. For the alkali metal Li we also obtained interesting results. The ethylene molecule is able to complex with two Li atoms with a binding energy of 0.7 eV/Li. This complex then binds up to two H_2 molecules per Li with a binding energy of 0.24 eV/H_2 and an absorption capacity of 16 % mass fraction of hydrogen.

The stability of the proposed metal-ethylene complexes was tested by extensive calculations such as normal-mode analysis, finite temperature first-principles molecular dynamics simulations, and reaction path calculations [3, 4]. These calculations indicate that the proposed structures are stable up to 500 K. Among many vibrational modes, we note that the H_2 stretching mode is around 330 meV to 420 meV for the absorbed H_2 molecules, significantly lower than ≈ 540 meV for the free H_2 molecule. Such a shift in the mode frequency would be the key feature that can be probed by inelastic neutron scattering measurement to confirm a successful synthesis of the structures predicted here.

In conclusion, we showed that an individual ethylene molecule functionalized by metal atoms can bind up to several hydrogen molecules via the Dewar-Kubas interaction, reaching a mass fraction gravimetric density as high as 16 %. These results suggest that co-deposition of transition/lithium metals with small organic molecules into nanopores of low-density materials could be a very promising direction for discovering new materials with better storage properties.

References

[1] T. Yildirim and S. Ciraci, Phys. Rev. Lett. **94**, 175501 (2005).

[2] T. Yildirim, J. Iniguez, and S. Ciraci, Phys. Rev. **B 72**, 153403 (2005).

[3] E. Durgun, S. Ciraci, W. Zhou, and T. Yildirim, Phys. Rev. Lett. **97**, 226102 (2006).

[4] W. Zhou, T. Yildirim, E. Durgun, and S. Ciraci, Phys. Rev. B, in press (2007).

Exceptionally Stable Organic Glasses

S. F. Swallen[1]; K. L. Kearns[1]; M. K. Mapes[1]; Y. S. Kim[1]; R. J. McMahon[1]; M. D. Ediger[1]; T. Wu, L. Yu[1]; S. K. Satija[2]

Glasses made from small organic molecules (organic glasses) have potential applications in many areas as diverse as amorphous pharmaceuticals, optoelectronic, photochromic and photovoltaic devices. In all of these applications thermal and kinetic stability of the glass are important criteria. Stability can be a problem for amorphous pharmaceuticals in particular: if the internal structure changes during storage, properties such as solubility also will change, potentially undermining the effectiveness of the drug. Conventional organic glasses produced by cooling liquids at experimentally accessible rates often show poor stability. Herein we show that *vapor deposition of organic molecules* can create high density glassy materials with extraordinary thermodynamic and kinetic stability. We attribute this substantial improvement in thermodynamic and kinetic stability to enhanced molecular mobility within a few nanometers of the glass surface during deposition.

Glassy materials combine the disordered structure of a liquid with the mechanical properties of a solid. Glasses are usually prepared by cooling a liquid, but accessing low energy states by this route is impractically slow [1]. If a liquid avoids crystallization as it is cooled, molecular motion eventually becomes too slow to allow the molecules to find equilibrium configurations. This transition to a nonequilibrium state defines the glass transition temperature T_g. Glasses are "stuck" in local minima on the potential energy landscape [2,3]. Since glasses are thermodynamically unstable, lower energies in the landscape are eventually achieved through molecular rearrangements. However, this process is so slow that it is generally impossible to reach states deep in the landscape by this route.

We have discovered that vapor deposition can bypass these kinetic restrictions and produce glassy materials that have extraordinary energetic and kinetic stabilities, and unusually high densities. We demonstrate this for two molecular glass formers: 1,3-bis-(1-naphthyl)-5-(2-naphthyl)benzene (TNB, T_g = 347 K) and indomethacin (IMC, T_g = 315 K). For these systems, the most stable glasses are obtained when vapor deposition occurs onto a substrate controlled near T_g - 50 K, where T_g is the bulk value.

Differential scanning calorimetry (DSC) was used to examine the kinetics and thermodynamics of vapor-deposited samples created by heating crystalline TNB or IMC in a vacuum. Figure 1 shows DSC data for TNB vapor-deposited (blue) onto a substrate held at 296 K. This scan was continued to above the melting point, after which the sample was cooled into the glass and then scanned again to yield the black curve. This latter curve represents the behavior of an ordinary glass of TNB, with T_g = 347 K, as defined by the onset temperature; it is consistent with previously reported results for TNB [4]. Remarkably, the vapor deposited sample has a significantly higher onset temperature of 363 K. This indicates that the vapor-deposited material is kinetically much more stable, since higher temperatures are required to dislodge the molecules from their glassy configurations. For comparison, we isothermally annealed the ordinary glass for 6 months at 296 K and up to 15 days at 328 K (equilibrium was reached at 328 K). Vapor-deposited samples created in only a few hours have much greater kinetic stability than ordinary glasses aged for many days or months below T_g.

We have used neutron reflectivity to characterize diffusion in ordinary and stable glasses of TNB. As schematically shown in the inset of Fig. 2, 300 nm films were prepared by alternately vapor-depositing layers of protonated TNB (h-TNB) and deuterated TNB (d-TNB). The specular reflectivity, R, was measured as a function of beam angle relative to the sample surface, and is plotted as a function of the wavevector q. Reflectivity curves for TNB samples vapor-deposited at different temperatures are presented in the main part of Fig. 2. The peaks represent diffraction: only odd diffraction

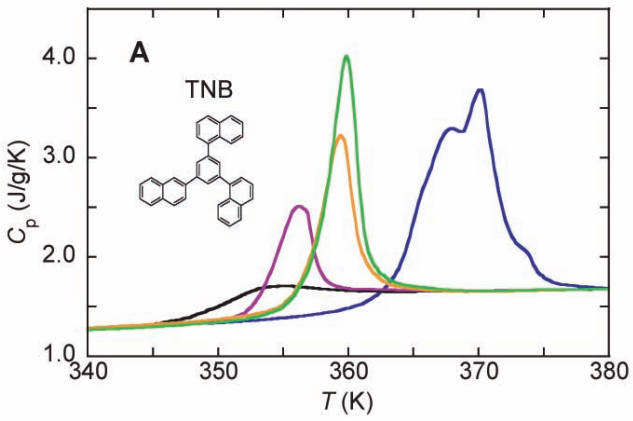

FIGURE 1: Heat capacity, C_p, of TNB samples; blue: vapor-deposited directly into a DSC pan at 296 K at a rate of ≈ 5 nm/s ; black: ordinary glass produced by cooling the liquid at 40 K/min; ordinary glass annealed at 296 K for 174 days (violet), 328 K for 9 days (gold), and 328 K for 15 days (green).

[1]University of Wisconsin, Madison, WI 53705
[2]NIST Center for Neutron Research, National Institute of Standards and Technology, Gaithersburg, MD 20899

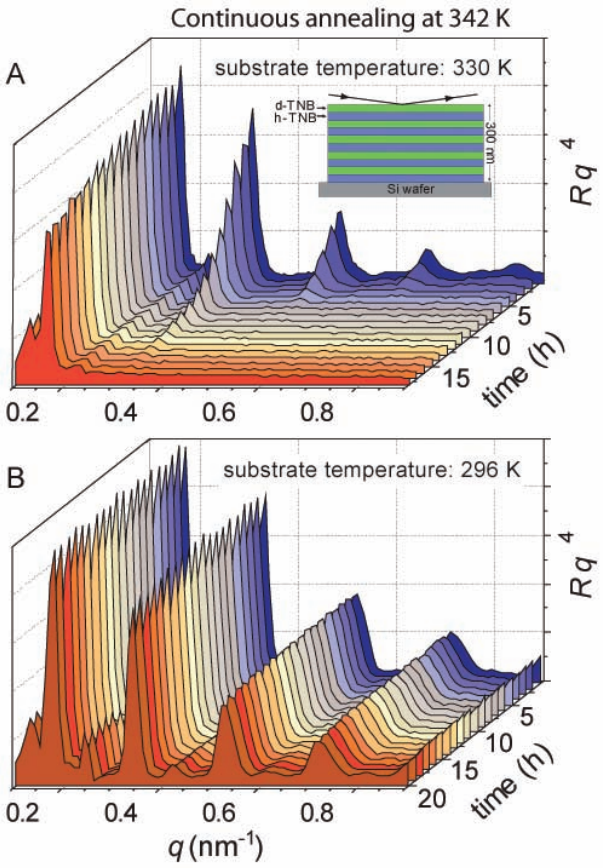

FIGURE 2: Neutron reflectivity data for TNB glass multilayer films (inset) taken periodically while continuously annealing at 342 K. The substrate temperature during vapor deposition in (A) was 330 K; the decay of the harmonic peaks in occurs over 8 h and is due to bulk molecular diffusion [5]. In (B), remarkably, by simply changing the substrate temperature to 296 K during deposition no detectible diffusion occurs over 16 h.

orders are present, as expected for our symmetric multilayer samples. For samples deposited at low temperature, diffraction can be observed up to 13th order, indicating very sharp h-TNB/d-TNB interfaces.

Figure 2 shows a time series of neutron reflectivity curves obtained for two vapor-deposited samples during annealing at 342 K. The sample in panel A was deposited at 330K. During 8 hours of annealing, all diffraction peaks (except the first order peak) decay to zero, indicating that substantial interfacial broadening has occurred due to interdiffusion of h-TNB/d-TNB. The sample in panel B was deposited at 296 K. During the 16 hours of annealing at 342 K, no detectable interdiffusion has occurred, even on the single nanometer length scale. We emphasize that the only difference between these two samples was the temperature at which the substrate was held during deposition. Figure 2A illustrates the behavior of an ordinary glass annealed near T_g, as published earlier [5]. Interdiffusion in this sample is characteristic of the equilibrium liquid. In contrast, the sample deposited near T_g - 50 K (Fig. 2B) is kinetically much more stable, in qualitative agreement with the high onset temperature shown for the vapor-deposited sample in Fig. 1. Consistent with this result, we have observed in preliminary experiments that crystal growth rates in stable TNB glasses are slower than in ordinary glasses, although vapor-deposited samples may contain crystal nuclei.

We attribute the enhanced stability and high density of vapor deposited glasses to enhanced mobility within a few nanometers of the surface of a TNB glass. Such mobility would explain both the broad interfaces observed in the as-deposited samples and the unusually stable glasses formed by vapor-deposition. The surface-mobility mechanism for the creation of unusually stable glasses is supported by an order-of-magnitude calculation. TNB samples vapor-deposited at 296 K have interface widths of 2.5 nm, somewhat in excess of the width associated with surface roughness. We attribute 1 nm of interface width to surface mobility, and given a deposition rate of 0.1 nm/sec, the molecules are within the mobile surface layer for 10 s. Combining this length and time yields an estimate for the surface diffusion coefficient of 5 x 10^{-16} cm^2/sec. For bulk TNB, this diffusion coefficient is found near T_g, where the structural relaxation time τ_α is a few seconds. Thus surface molecules plausibly remain mobile for several structural relaxation times before becoming buried, arguably long enough to find near-equilibrium configurations at 296 K. Recent experiments also show that the optimum temperature for making most stable glasses is near ≈ 0.85 T_g. Deposition below this temperature does not produce stable glasses because at low deposition temperatures the molecules do not have enough time to relax into low energy configurations, i.e., there is a deposition temperature window for achieving glass stability.

In summary we have shown that vapor deposited glasses of TNB can be made unusually stable by depositing the glass at lower temperatures of the order of 0.85 T_g. We speculate that unusually stable glasses can be prepared for many systems that can be vapor-deposited, if surface mobility is enhanced and the substrate temperature is appropriately controlled. Stable glasses could also impact technologies such as amorphous pharmaceuticals, where stability against crystallization is required in order to retain the enhanced bioavailability of amorphous preparation. For more detailed information on this system the reader is referred to our recent article [6].

References

[1] M. D. Ediger, C. A. Angell, S. R. Nagel, J. Phys. Chem. **100**, 13200 (1996).
[2] P. G. Debenedetti, F. H. Stillinger, Nature **410**, 259 (2001).
[3] F. H. Stillinger, Science **267**, 1935 (1995).
[4] C. M. Whitaker, R. J. McMahon, J. Phys. Chem. **100**, 1081 (1996).
[5] S. F. Swallen *et al.*, Journal of Chemical Physics **124**, 184501 (2006).
[6] S. F. Swallen *et al.*, Science **315**, 353 (2007).

Hydrogen Storage in a Prototypical Zeolitic Imidazolate Framework-8

H. Wu[1, 2]; W. Zhou[1, 3]; T. Yildirim[1, 3]

Crystalline porous compounds with well-defined nano-openings have long been used as chemical filters and gas-entrapment materials. Intense interest currently surrounds their potential to store hydrogen for next generation transportation applications. Zeolitic imidazolate frameworks (ZIFs) are a new class of nanoporous compounds which consist of tetrahedral clusters of MN_4 (M = Co, Cu, Zn, etc.) linked by simple imidazolate ligands [1,2]. As a subfamily of metal-organic frameworks (MOFs), ZIFs exhibit the tunable pore size and chemical functionality of classic MOFs. At the same time, they possess the exceptional chemical stability and rich structural diversity of zeolites [2]. Because of these combined features, ZIFs show great promise for hydrogen storage applications. However, in contrast to a large number of extensive studies of other MOFs, no experimental work concerning the nature of H_2-ZIF interactions and the manner in which hydrogen molecules are adsorbed has yet been reported. Such fundamental studies hold the key to optimizing this new class of ZIF materials for practical hydrogen storage applications.

ZIF8 is a prototypical ZIF compound ($Zn(MeIM)_2$, MeIM = 2-methylimidazolate) with a sodalite (SOD) zeolite-type structure, exhibiting an interesting nanopore topology formed by 4-ring and 6-ring ZnN_4 clusters, as shown in Fig. 1. Since the nanopores are only accessible through narrow 6-ring funnel-like channels (Fig. 1a), one wonders how H_2 molecules are adsorbed, where the major binding sites are and what the binding energies are. This article highlights our work using the Fourier difference analysis of neutron powder diffraction data along with first-principles calculations to provide answers to these questions for the first time [3].

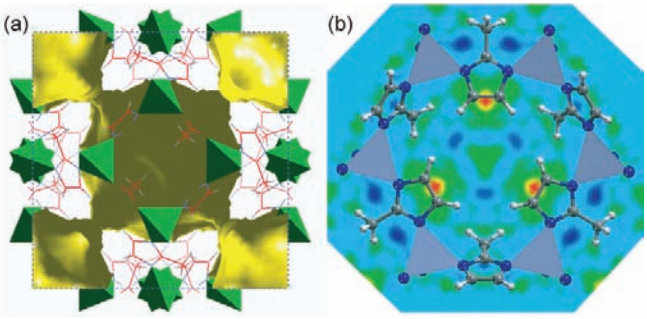

FIGURE 1: (a) (001) view of refined crystal structure of ZIF8 host lattice from neutron powder diffraction along with the available free space (pore structure) for H_2 occupation, based on van der Waals interactions. (b) A (111) view of the real-space Fourier-difference scattering-length density superimposed with 6-ring pore aperture of the ZIF8 structure, indicating the location of the first adsorption sites (red-yellow regions).

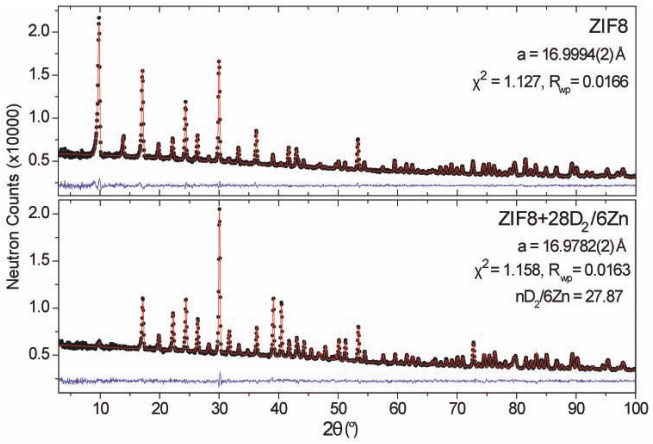

FIGURE 2: Observed (dots), refined (line), and difference (noisy line) neutron powder diffraction profiles (λ = 2.079 Å, 3.5 K) for ZIF8 host lattice (space group $I4\bar{3}m$) and ZIF8 with D_2 loading of $28D_2$/6Zn.

ZIF8 was synthesized using a solvothermal method as described in Ref. 2. Neutron powder diffraction data were collected on the BT-1 diffractometer. Because of the large incoherent cross section of H_2, adsorption was studied as a function of D_2 concentration per ZIF8 molecular formula ($Zn_6N_{24}C_{48}H_{60}$). Target amounts of D_2, i.e., $3D_2$, $16D_2$, and $28D_2$ per 6Zn, were loaded into the ZIF8 sample at 70 K. One H_2/6Zn corresponds to ≈ 0.15 % mass fraction hydrogen uptake. The sample was then cooled to 30 K at which point the D_2 was completely adsorbed. Once the system was equilibrated at 30 K, the sample was further cooled to 3.5 K before the diffraction measurement.

The top panel of Fig. 2 shows the neutron diffraction data from the ZIF8 bare material measured at 3.5 K. The refined lattice parameters and atomic positions of Zn, N and C agree well with previously reported room temperature x-ray diffraction result. The high resolution neutron diffraction data also enabled us to unambiguously determine the orientation (i.e., the hydrogen positions) of the methyl group, which was not possible in the x-ray measurement.

[1]NIST Center for Neutron Research, National Institute of Standards and Technology, Gaithersburg, MD 20899
[2]University of Maryland, College Park, MD 20742
[3]University of Pennsylvania, Philadelphia, PA 19104

For comparison, the neutron diffraction patterns from ZIF8 with the following D_2 concentrations: nD_2 = 3, 16, 28 per 6Zn are also shown in Fig. 2 (also see Ref. 3). Using the model of the refined ZIF8 host structure, we performed Rietveld structure refinements on the D_2 adsorbed samples. The Fourier difference method was used to find the scattering-length density distribution for D atoms based on the refinements ignoring the adsorbed D_2 molecules. Fig. 1b is an example of such a Fourier-difference plot, which clearly shows that the initial adsorption site (i.e., D1) is on top of the MeIM organic linker and close to the C=C bond, thus termed the "IM site".

Upon D_2 loading, the order of site filling in ZIF8 was determined to be sequential from D1 to D6, shown in Fig. 3. The already mentioned D1 site and the second site (D2) are both determined from the initial loading of $3D_2$/6Zn. The latter site is located at the center of the channel of the 6-ring opening (termed "channel site I"). For $16D_2$/6Zn loading, the D1 and D2 sites are nearly fully occupied, and the third adsorption site (D3) starts to populate. The third site is also at the center of 6-ring opening but located on the other side of the complex, so we termed it "D3: channel site II". This site is less favorable than the D2 channel site I due to the presence of the methyl group, mainly a geometry effect. Interestingly, the first three adsorption sites discussed above form a pseudo-cubic "nanocage" with the edges slightly bent toward the ZIF8 framework, as shown in Fig. 3c. We also observed a small amount (≈ 5 %) of D_2 adsorbed at a fourth site (D4) located at the face center of the H_2-nanocage.

With further D_2 loading, the first three adsorption sites were almost completely occupied. For the maximal loading of $28D_2$/Zn, the fourth site discussed above as well as two additional sites (D5 and D6) close to the center of the void in ZIF8 (inside the nanocage formed by the first three sites), are progressively occupied. The nearest neighbor distances between these adsorption sites are about 3.04 Å, significantly shorter than 3.6 Å found in solid H_2. Self-assembled 3D interlinked hydrogen nanostructures with short intermolecular distances were previously observed in MOF5 [4] and seem to be a common novel feature of these nanoporous metal-hybrid systems.

To understand the hydrogen host-lattice interactions further, we also performed total-energy calculations from density functional theory (DFT) using the plane-wave implementation of the local-density approximation to DFT. Consistent with experimental observation, our calculations suggested that the IM and channel site I are the most energetically stable adsorption centers. The calculated H_2 binding energies for these two sites are 170 meV and 147 meV, respectively, in agreement with the larger population of the IM site at low D_2 loading.

In conclusion, we obtained detailed structural information such as the orientation of the methyl groups, H_2 adsorption sites and binding energies in the ZIF8 structure for the first time. The imidazolate organic linker is primarily responsible for adsorption, in contrast to metal oxide-based MOFs.

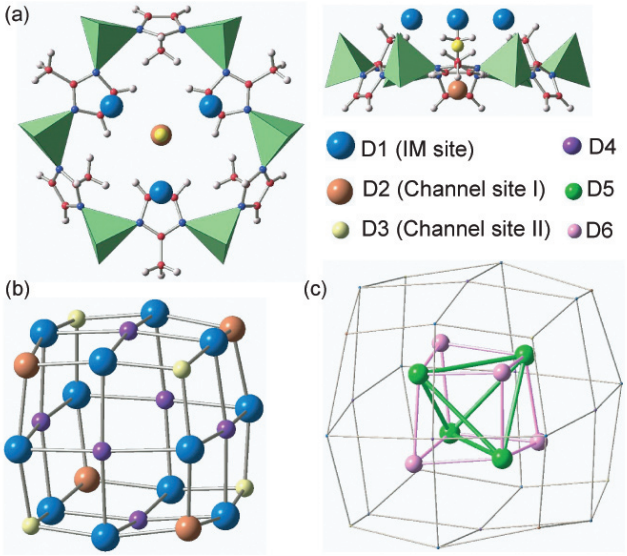

FIGURE 3: The hydrogen adsorption sites obtained from Fourier difference analysis. (a) Top and side views of first three adsorption sites near a Zn-hexagon opening. (b) Pseudo-cubic nanocage formed by D1, D2 and D3 sites. (c) Tetrahedron-like nanocage formed by D5 and D6 sites.

This suggests that modification of the linkers rather than metal types in ZIFs is more important to optimize these materials for higher storage capacity. At high concentration of hydrogen loading, ZIF8 is able to hold hydrogen molecules up to a mass fraction of 4.2 % as self-assembled nanostructures with relatively short intermolecular distances compared to solid hydrogen. This suggests that ZIFs can also be used as an ideal template host-material to generate molecular nanostructures with interesting properties.

References

[1] X. C. Huang, Y. Y. Lin, J. -P. Zhang, X. M. Chen, Angew. Chem. Int. Ed. **45**, 1557 (2006).

[2] K. S. Park, Z. Ni, A. P. Cote, J. Y. Choi, R. D. Huang, F.J. Uribe-Romo, H. K. Chae, M. O'Keeffe, O. M.Yaghi, Proc. Natl Acad. Sci. USA **103**, 10186 (2006).

[3] H. Wu, W. Zhou, T. Yildirim, J. Am. Chem. Soc. **129**, 5314 (2007).

[4] T. Yildirim and M. R. Hartman, Phys. Rev. Lett. **94**, 175501 (2005).

Bose-Einstein Condensate of Magnons in Coupled Spin Ladders

V. O. Garlea, A. Zheludev[1]; T. Masuda[2]; H. Manaka[3]; L.-P. Regnault, E. Ressouche, B. Grenier[4]; J.-H. Chung, Y. Qiu[5]; K. Habicht, K. Kiefer[6]; M. Boehm[7]

Field-induced transitions in quantum magnets can often be interpreted in terms of Bose-Einstein condensation (BEC) of magnons [1, 2]. Such transitions are fully equivalent to BEC of atoms in liquid ^{4}He, laser-cooled gases in magnetic traps. An interesting conundrum is presented by BEC of magnons in weakly interacting gapped quantum spin chains or ladders [2]. Here the disordered spin liquid normal state is a unique property of 1-dimensional (1D) topology. In contrast, the stability of the magnon condensate at high fields is necessarily a 3D effect, and relies on residual inter-chain interactions. The phenomenon is therefore one of the more striking examples of dimensional crossover in many-body quantum mechanics. Do the topology and one-dimensionality of the normal state influence the properties of the condensate? We addressed this question experimentally by a neutron scattering study of the field-induced BEC in a prototypical spin ladder material, $(CH_3)_2CHNH_3CuCl_3$ (IPA-$CuCl_3$) [3,4].

Both an isotropic spin Hamiltonian and some 3D magnetic interactions are prerequisites of true BEC in magnetic systems. At high fields the magnon condensate is then a commensurate, gapless, 3D-ordered phase [2]. To date, such transitions were detected experimentally in only a handful of model compounds and, for mostly technical reasons, the excitation spectrum at high fields could only be studied in sufficient detail in the 3D system $TlCuCl_3$ [5]. In this material the disorder and spin gap in zero field are due to local singlet ground states of structural spin dimers. Our prototype compound IPA-$CuCl_3$ is in fact a uniform $S = ½$ ladder system. It undergoes a magnetic BEC transition in accessible fields and has energy scales ideally suited for inelastic neutron scattering (INS) studies of the excitation spectrum. The spin ladders in IPA-$CuCl_3$ are built of $S = ½$ Cu^{2+} ions and run parallel to the *a* axis of the triclinic P1 crystal structure (Fig. 1).

Excitations from this quantum-disordered ground state are revealed in INS experiments that directly probe the pair spin correlation function $S(q,\omega)$. Fig. 2a shows a time-of-flight (TOF) spectrum collected on an IPA-$CuCl_3$ single crystal sample at $T = 100$ mK in zero magnetic field using the Disk Chopper Spectrometer (DCS) at the NCNR. The magnon, with a steep parabolic dispersion along the *a* axis and a gap at the 1D antiferromagnetic (AF) zone-center $h = 0.5$, is clearly visible. The energy gap ($\Delta = 1.2$ meV) is small

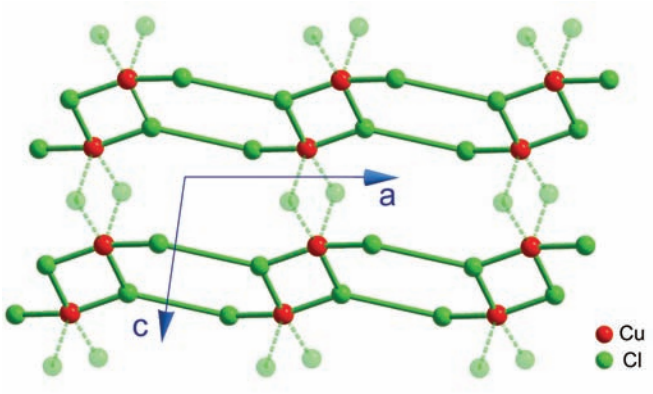

FIGURE 1: Layers of magnetic Cu^{2+} (red) and the bridging Cl^- (green) ions in IPA-$CuCl_3$, showing the spin ladders running along the *a* axis.

compared to the chain-axis magnon bandwidth, but is considerably larger than inter-chain interactions along the *c* and *b* axes. The corresponding bandwidths are 0.4 meV and < 0.1 meV, respectively, and thus not potent enough to disrupt the 1D spin liquid.

Figure 3 shows INS spectra collected at the 1D AF zone-center $h = 0.5$ in several fields using the SPINS 3-axis spectrometer at the NCNR with 3.7 meV fixed incident energy neutrons, horizontally focusing pyrolitic graphite analyzer, and a BeO filter after the sample. As the field is turned on, the single peak at $\mu_o H = 0$ becomes divided into three equidistant components. As the gap softens, commensurate long-range AF order sets in and gives rise to new magnetic Bragg reflections of type $(h+½, k, l)$, h, k and l-integer. The measured field dependence of the (0.5, -1, 0) peak is consistent with a mean field critical exponent $\beta = 0.5$, expected for a 3D BEC transition [3,4].

A key result of this work is a direct measurement of excitations of the magnetic Bose-Einstein condensate in IPA-$CuCl_3$. Data collected above the critical field are shown in Fig. 2b. Three distinct excitation branches, two gapped and one gapless, are clearly visible, though the overall inelastic intensity is reduced compared to lower fields. The gapless mode is fully analogous to the phonon in a conventional BEC, being the Goldstone mode associated with the spontaneous breaking of $O(2)$ symmetry. It is a *collective* excitation of the magnon condensate and has a linear dispersion relation. At $H > H_c$

[1]Oak Ridge National Laboratory, Oak Ridge, TN 37831
[2]Yokohama City University, Yokohama City, Kanagawa, 236-0027, Japan
[3]Kagoshima University, Korimoto, Kagoshima 890-0065, Japan
[4]CEA-Grenoble, DRFMC-SPSMS-MDN, 38054 Grenoble Cedex 9, France
[5]NIST Center for Neutron Research, National Institute of Standards and Technology, Gaithersburg, MD 20899 and University of Maryland, College Park, MD, 20742
[6]BENSC, Hahn-Meitner Institut, D-14109 Berlin, Germany
[7]Institut Laue Langevin, 38042 Grenoble Cedex 9, France

it takes the place of the massive quadratically dispersive *single-magnon* excitation seen below the critical field (Fig. 2a). Similarly, the phonon in a conventional Bose gas is a linearly dispersive collective mode that replaces quadratically dispersive individual particles in the normal state. The two massive (gapped) excitations seen in Fig. 2b are descendants of the $S_z = 0$ and $S_z = 1$ members of the Haldane triplet at $H < H_c$ and are thus specific to the magnetic case. Even though above the critical field one finds 3D AF long range order, the observed spectrum is distinct from that of spin waves in a classical magnet. The latter are transverse-polarized precession waves in the long range order parameter field. For a Heisenberg AF in an external magnetic field one expects one gapless and one gapped spin wave, in contrast with two gapped modes detected in IPA-$CuCl_3$. The high field ordered phase should therefore be described as a quantum spin solid, in contrast to the classical spin solid in conventional magnets.

While the critical behavior and long-wavelength spectral features in IPA-$CuCl_3$ are very similar to those in spin-dimer systems, the *short-wavelength* spin dynamics at the zone

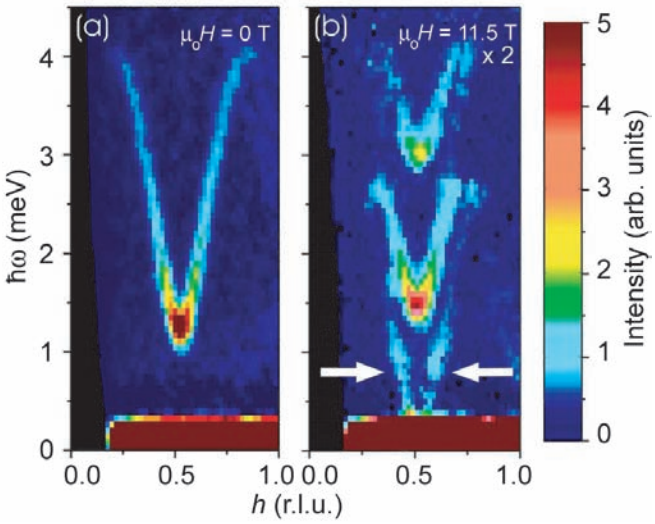

FIGURE 2: TOF neutron spectra measured in IPA-$CuCl_3$ in the 1D Haldane-gap spin liquid phase (a) and the 3D ordered BEC phase (b), at $\mu_o H = 0$ and $\mu_o H = 11.5$ T, respectively. Solid white arrows indicate the linearly dispersive gapless Goldstone mode. The abbreviation r.l.u. stands for reciprocal lattice units.

boundary is strikingly different. We find that the two massive excitations in IPA-$CuCl_3$ undergo a qualitative change upon the BEC transition. As seen in Fig. 2b, at $\mu_o H = 11.5$ T, only 20 % above H_c, their bandwidths are suppressed by over a factor of two. At $H > H_c$ the emergence of long-range AF order breaks an additional discrete symmetry operation, namely a translation by the structural period of the ladder. The spontaneous doubling of the period implies that at $H > H_c$ the wave vectors $h = 0$, $h = 0.5$ and $h = 1$ become equivalent magnetic zone centers. At the same time, $h = 0.25$ and $h = 0.75$ emerge as the new boundaries of the Brillouin zone. The result is a formation of anticrossing gaps for all magnons at these wave vectors, which translates into a

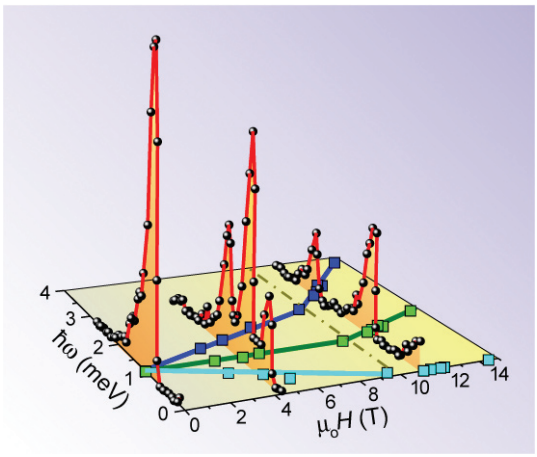

FIGURE 3: SPINS spectra and the measured gap energies at the 1D AF zone center $h = 0.5$ as a function of applied magnetic field, at $T = 100$ mK. The magnetic field drives the energy of low-lying magnons to zero by virtue of the Zeeman effect, prompting them to condense at a critical field $\mu_o H_c = 9.6$ T.

reduction of the zone-boundary energy of the two gapped magnons in IPA-$CuCl_3$.

Our experiments illustrate that any *long-wavelength* characteristics of the field-induced magnetic BEC transition and the magnon condensate, such as critical indexes, emergence of the Goldstone mode and behavior of gap energies, are universal. They are not affected by the 1D topological nature of the normal state in spin chains and ladders, and are very similar to those in local cluster spin systems. In contrast, the *short-wavelength* properties can be significantly different in these two classes of materials. In coupled AF spin chains or ladders, unlike in many couple dimer systems, and unlike in conventional BEC, the transition breaks an additional discrete symmetry. The result is a radical modification of the excitation spectrum.

References

[1] E. G. Batyev, L. S. Braginski, Sov. Phys. JETP **60**, 781 (1984).
[2] T. Giamarchi, A. M. Tsvelik., Phys. Rev. B **59**, 11398 (1999).
[3] V. O. Garlea, A. Zheludev, T. Masuda, H. Manaka, L.-P. Regnault, E. Ressouche, B. Grenier, J.-H. Chung, Y. Qiu, K. Habicht, K. Kiefer, and M. Boehm, Phys. Rev. Lett. **98**, 167202 (2007).
[4] A. Zheludev, V. O. Garlea, T. Masuda, H. Manaka, L.-P. Regnault, E. Ressouche, B. Grenier, J.-H. Chung, Y. Qiu, K. Habicht, K. Kiefer, and M. Boehm, Phys. Rev. B., submitted; arXiv:0705.1360 (2007).
[5] C. Ruegg, N. Cavadini, A. Furrer, H.-U. Gudel, K. Kramer, H. Mutka, A. Wildes, K. Habicht, and P. Vorderwisch, Nature **423**, 62 (2003).

Magnetic Resonance Mode and the Superconducting Condensate in a High-T_c Cuprate

S. D. Wilson, P. Dai, S. Li, J. Zhao[1]; J. W. Lynn[2]; G. Mu, H.-H. Wen[3]; P. G. Freeman, L.-P. Regnault[4]; K. Habicht[5]

Although the precise mechanism responsible for the formation of the superconducting condensate in the high-transition-temperature (high-T_c) copper oxides remains an area of ongoing research, vast experimental efforts over the past two decades have shown conclusively that magnetism plays an important role within the physics of high-T_c superconductivity. One key challenge remaining however is to experimentally identify the nature and extent through which magnetism in these high-T_c cuprates couples to the electronic charge carriers. Specifically, the fundamental mode of coupling between magnetic order (either static or fluctuating) and the quasiparticles responsible for Cooper pair formation remains a pivotal focus of research in the high-T_c community. In the work highlighted here, we have performed studies on the BT-9 triple axis spectrometer at the NCNR using high magnetic fields to explore the relationship between the well-studied magnetic resonance mode in high-T_c cuprates and the corresponding condensation energy of the superconducting phase in an electron-doped cuprate, $Pr_{.88}LaCe_{.12}CuO_{4-\delta}$ (PLCCO, $T_c = 24$ K) [1]. Additionally, by capitalizing on the relatively low field necessary to completely suppress superconductivity in the n-type cuprates, we have measured the detailed changes in the static and dynamic spin behavior in a high-T_c cuprate as it is driven into its field-suppressed, nonsuperconducting ground state.

In searching for magnetic properties that demonstrate a clear coupling to the superconducting phase in the high-T_c cuprates, one particular feature—the magnetic resonance mode—has been promising. The resonance mode itself is a collective spin excitation within the CuO_2 planes of the cuprates and is observed along the commensurate antiferromagnetic (AF) ordering wave vector at $\boldsymbol{Q} = (0.5, 0.5)$ in the *ab*-plane. Direct coupling between the superconducting phase and the resonance excitation has been observed through the mode's complete disappearance above T_c in optimally doped-cuprate systems and through the characteristic frequency of the resonance mode being directly proportionally to T_c. This intimate link between the energy scale of the superconducting phase and that of the resonance mode, $E_R = 5.8\ k_B T_c$, along with the resonance mode's universal presence in all classes of high-T_c cuprates, has led to speculation that the resonance is intimately related to electron pairing and superconductivity.

To demonstrate that the resonance mode is indeed related to the electron-electron pairing process in the high-T_c cuprates, an experimental signature must be established that shows a definitive coupling between the resonance mode and the quasiparticle behavior within the superconducting phase. At moderate field strengths, a *c*-axis aligned magnetic field introduces vortices into the CuO_2 planes of the cuprates and weakens the superconducting state. Once the field strength reaches above the upper critical field (H_{c2}) of the system, the nonsuperconducting vortex regions prevent the establishment of a coherent superconducting phase. Thus, through comparison of the magnetic field behavior of the quasiparticle excitations observed via heat capacity measurements with inelastic neutron measurements of the resonance mode, possible links between quasiparticle behavior and the resonance can be investigated. In fact, previous measurements on the hole-doped $YBa_2Cu_3O_{6.6}$ ($YBCO_{6.6}$) system have attempted such a study by demonstrating that the resonance mode is partially suppressed under the application of a *c*-axis aligned magnetic field in a fashion similar to the measured condensation energy [2]. While these results suggest a

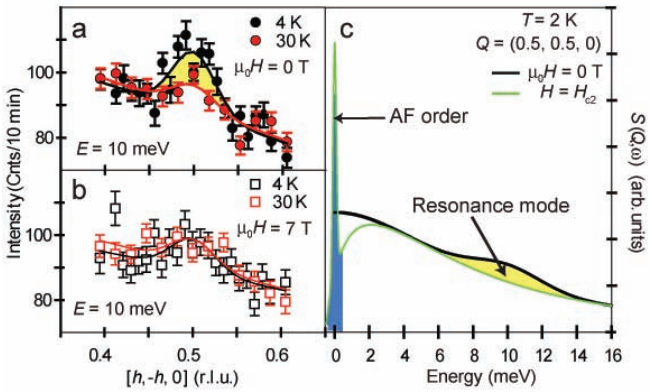

FIGURE 1: a) BT-9 momentum scans through the $Q = (0.5, 0.5)$ in-plane AF ordering wave vector at the resonance energy in PLCCO, $\Delta E = 10$ meV. The enhancement observed upon cooling into the superconducting phase (yellow shaded region) at (0.5, 0.5) is indicative of the resonance mode. b) 7 T ($\approx \mu_0 H_{C2}$) momentum scans through $Q = (0.5, 0.5)$ at the resonance energy. The resonance mode has completely vanished under this field strength. c) Schematic of $S(Q, \omega)$ versus energy at $T = 2$ K at the AF ordering wave vector for PLCCO under both 0 T and 7 T. Upon the application of a superconductivity-suppressing field, quasi-2D AF order is stabilized, and the resonance mode is completely suppressed.

[1]University of Tennessee, Knoxville, TN 37996
[2]NIST Center for Neutron Research, National Institute of Standards and Technology, Gaithersburg, MD 20899
[3]National Laboratory for Superconductivity, Chinese Institute of Physics, Beijing, China
[4]Institute Laue-Langevin, Grenoble, France
[5]Hahn-Meitner Institut, Berlin, Germany

link between the resonance mode and the quasiparticle excitations measured through specific heat, the experiments were unable to completely suppress T_c and the corresponding condensation energy due to the extremely high H_{c2}'s manifested by all of the hole-doped cuprates.

Fortunately, for the electron-doped cuprates the upper critical fields are substantially lower than their hole-doped counterparts, and the magnetic resonance mode has very recently been observed in these systems [3]. This discovery, along with the advantageous feature of an experimentally accessible H_{c2}, now enables a study of the detailed evolution of the resonance mode as superconductivity is driven into its field suppressed ground state. Specifically, we have chosen to study the c-axis aligned magnetic field dependence of the resonance in the optimally-doped $Pr_{.88}LaCe_{.12}CuO_{4-\delta}$ (PLCCO $T_c = 24$ K) cuprate system.

Our results are shown in Fig. 1 a-b, where for fields greater than H_{c2} we find that the resonance excitation completely vanishes. The upper critical field in this geometry was determined to be ≈ 7 T through heat capacity measurements of the superconducting phase transition.

These heat capacity measurements, conducted in parallel to our neutron efforts, were also able to extract the field dependence of the superconducting condensation energy, U_c (Fig. 2b). Overplotting the relative field dependence of U_c and the resonance mode in Fig. 2a reveals that the resonance mode's rapid suppression as a function of field closely follows the suppression of U_c in PLCCO. The relative spectral weight of the resonance is therefore directly related to the quasiparticles participating in the superconducting condensate.

Our magnetic field experiments have also revealed the emergence of a competing AF phase with the suppression of superconductivity. Previous experiments on underdoped PLCCO concentrations ($T_c < 23$ K) have already demonstrated that a quasi-two dimensional AF state coexists with superconductivity, whereas for optimally doped PLCCO ($T_c > 23$ K) concentrations no zero field static magnetic order exists [4]. A direct competition between this quasi-2D AF phase in underdoped samples and superconductivity was shown through an enhancement in the coexisting AF phase upon the application of a *c*-axis aligned magnetic field. This competition, however, was only observed in underdoped systems in which the AF phase already coexisted with SC under zero field. Indeed, previous studies on optimally doped PLCCO concentrations were unable to resolve the appearance of any field-induced competing AF phase in samples which initially possessed no AF order (perhaps due to small signal or insufficient sample mass). Our neutron studies of the present optimally doped system have now shown the clear appearance of a field-induced quasi-two dimensional AF phase. The induced AF magnetic signal exhibits an anisotropic response with respect the applied field direction with no observable order induced under the application of a magnetic field parallel to CuO_2 planes. This is a clear indication that the induced AF signal

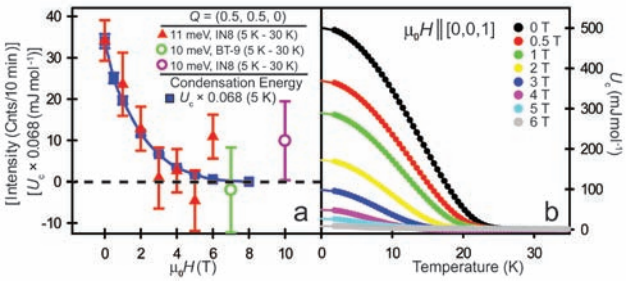

FIGURE 2: a) Field dependence of the condensation energy, U_c, (in blue symbols) overplotted with the field dependence of the resonance mode in PLCCO. The resonance mode completely disappears by 7 T coincident with the vanishing of the condensation energy. b) Temperature dependence of U_c under various fields. The magnetic field was applied along the perpendicular to the CuO_2 planes.

arises through a direct competition with the SC phase (which is strongly suppressed when the field is oriented parallel to c-axis while only slightly affected when the field is parallel to the *ab*-plane). This behavior is strikingly similar to the competition between the SC phase and the incommensurate spin density wave state in the $La_{2-x}Sr_xCuO_4$ (LSCO) hole-doped system, thereby suggesting that the presence of a competing magnetic phase coexisting with SC is a common feature of the cuprates.

Through our high-field neutron studies of the static order, low energy excitations, and resonance mode in the PLCCO, we have mapped out a comprehensive picture of the modification of the spin behavior in a cuprate superconductor as it is driven into its field suppressed, non-superconducting groundstate (Fig. 1c). Our results show that the spectral weight of the resonance in PLCCO is directly connected to the system's condensation energy, with the resonance mode vanishing entirely with the field-suppression of the superconducting phase. Even more intriguing is the apparent observation of the transfer of spectral weight from the suppressed resonance mode into a newly stabilized AF phase under field. However, future experiments are required to quantitatively test this. The picture through which the spin excitations and static magnetic order in the cuprates evolve as these systems are driven to be nonsuperconducting provides invaluable insight into the detailed nature of the ground state from which high-T_c manifests itself. The present work has taken a fundamental step toward forming this picture by providing a comprehensive study of the magnetism in the field suppressed ground state of PLCCO.

References

[1] S. Wilson *et al.*, Proceedings of the National Academy of Sciences **104**, 15259 (2007).

[2] P. Dai, H. A. Mook, G. Aeppli, S. M. Hayden, and F. Dogan, Nature **406**, 965 (2000).

[3] S. Wilson *et al.*, Nature **442**, 59 (2006).

[4] H. J. Kang *et al.*, Phys. **Rev. B. 71**, 214512 (2005).

Interfacial Domain Walls in Perpendicular Magnetic-Media Prototypes

S. M. Watson, J. A. Borchers[1]; T. Hauet[2]; S. Mangin, F. Montaigne[3]; E. E. Fullerton[4]

The advancement of computer technology and handheld digital devices has created a continuous demand for increased magnetic storage capacity. Traditional storage media has magnetic moments oriented in the film plane while in the newest "perpendicular" media information is stored in bits with magnetic moments oriented out of the plane. These multilayer films consist of a magnetically anisotropic ("hard") top layer over a more isotropic structured "soft" underlayer that returns the flux, but also plays several important roles in the design of the write head and read head. These innovations have led to a large increase in the density of stored bits to ≈ 40 Gbit/cm^2 (250 Gbit/in^2) with a limit projected eventually to reach 1000 Gbit/in^2. Perpendicular media, in which a single bit is comprised of a single domain, may allow for the lateral size constraints necessary to achieve this long term goal.

Studies of exchange-spring systems have shown that the exchange coupling between the hard and soft magnetic layers leads to the formation of a magnetic spiral during field reversal [1,2]. The system's transport properties depend upon the characteristics of these spiral domain walls, as demonstrated by magnetoresistance measurements (i.e., field-dependent resistance) that show pronounced features varying with the width of the spiral domain wall [3]. While depth-dependence of spirals can be directly probed using polarized neutron reflectivity in systems having in-plane moments, the out-of-plane moments can be probed only indirectly, since the scattering vector and the measurement direction are parallel in that case. Here we highlight our reflectivity studies that utilize a novel scattering geometry in order to extract the magnetic moment component in the film plane as a function of depth. This method obtains information on the field-dependent evolution of the in-plane domain wall.

To probe the field dependence of the magnetic moment reversal, we have used Polarized Neutron Reflectometry (PNR) with the incident neutron polarization perpendicular to the sample surface. This arrangement permits investigation of magnetic properties of an exchange-coupled bilayer system with out-of-plane magnetization. Using $Tb_{55}Fe_{142}Co_{37}$ (25 nm)/[Co (0.42 nm)/Pd (x)]$_{15}$ (x = 0.5, 0.7 nm) structures grown at room temperature on Si wafers by dc magnetron sputtering, we were able to study the evolution of the domain wall as a function of the Pd thickness. In this system, the moment configuration results from the competition among the applied magnetic field, short-range ferromagnetic (FM) exchange coupling between the Co layers, antiferromagnetic (AF) exchange coupling between the TbFeCo and neighboring Co layer, and long-range dipolar interactions. In addition, both the [Co/Pd] bilayers and TbFeCo exhibit strong out-of-plane anisotropy.

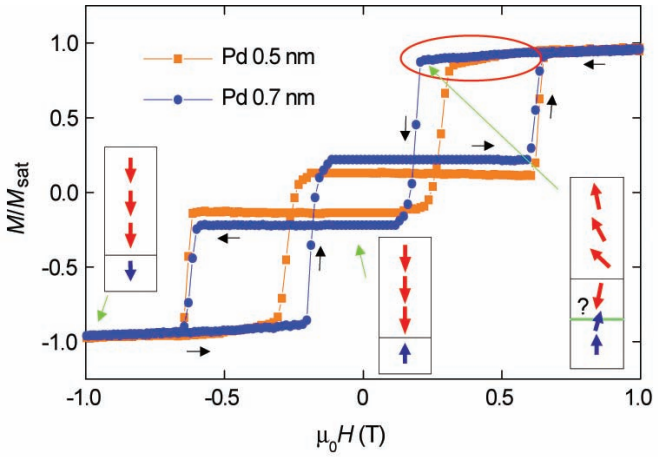

FIGURE 1: Comparison of magnetization vs applied field for films with Pd thicknesses of 0.5 nm and 0.7 nm taken at 300 K. The black arrows indicate the direction of the field sweep. The red oval highlights the gradual decrease in magnetization suggestive of the formation of a domain wall lying in the layer plane. The cartoons illustrate the behavior of selected Co moments (red) and the TbFeCo moment (blue) at various fields. The question mark in the cartoon indicates uncertain behavior in the layer neighboring TbFeCo, also shown in Fig. 3.

As a preliminary investigation, we measured the magnetic hysteresis curves of two films having different Pd thicknesses (Fig. 1). After saturation of all the layer moments in a high field, the first reversal occurs *before* reaching negative fields because of the strong AF coupling of the CoPd layers to the TbFeCo base. Note that the thinner Pd-separator sample (x = 0.5 nm) flips before the thicker one: as expected, the exchange coupling between Co layers is larger for a thinner Pd separator, and the AF coupling to the layer near the base dominates. Thus the magnitude of the exchange coupling between the Co layers may be tuned by changing the Pd thickness. Also note the gradual decrease in magnetization before the flip, which suggests that a gradual moment reversal, a domain wall, is developing through the layers.

[1]Center for Neutron Research, National Institute of Standards and Technology, Gaithersburg, MD 20899
[2]Hitachi Global Storage Technology, San Jose, CA 95135, USA
[3]LPM, Nancy University-CNRS, Vandoeuvre-les-Nancy Cedex, France
[4]University of California, San Diego La Jolla, CA 92093-0401

To reproduce the conditions for the magnetization measurements (Fig. 1), PNR data were obtained at a series of fields at room temperature. For the PNR experiments, both the neutron polarization and the external field were oriented perpendicular to the sample plane, parallel to the direction of the scattering vector ***Q***. There are four reflectivity cross-sections: R^{++} and R^{--} labeled non-spin flip (NSF) as the neutron retains its original polarization, and R^{+-} and R^{-+}, labeled spin flip (SF), where the neutron spin rotates 180°. In the new geometry, NSF reflectivity is sensitive to the chemical composition of the film, such as layer thicknesses and interfacial roughnesses. SF reflectivity is sensitive only to the component of the magnetization projected in the sample plane, i.e., perpendicular to the field direction. To obtain the chemical and magnetic profile as a function of depth, the PNR data were fitted using a least squares optimization. To reduce the number of free parameters, fits of the structural parameters from x-ray reflectivity data were applied to the neutron data and held constant while select neutron parameters were allowed to vary restrictively.

The field dependence of the spin-flip reflectivity data for films with Pd thicknesses of 0.5 nm and 0.7 nm is shown in Fig. 2. Qualitatively, an increase in spin-flip reflectivity magnitude is observed with decreasing field and shows a dependence overall on Pd thickness. As the field decreases from 0.7 T (near saturation), the observed increase in the scattering indicates that the in-plane component of the moment (and thus the in-plane projection of the domain wall) is growing. At 0.005 T, where we expect antiparallel alignment of the Co layers to the TbFeCo base, the SF reflectivity drops off as the in-plane moments are again reduced, with the Co and TbFeCo magnetic moments then aligned perpendicular to the film plane: i.e. the domain wall has collapsed.

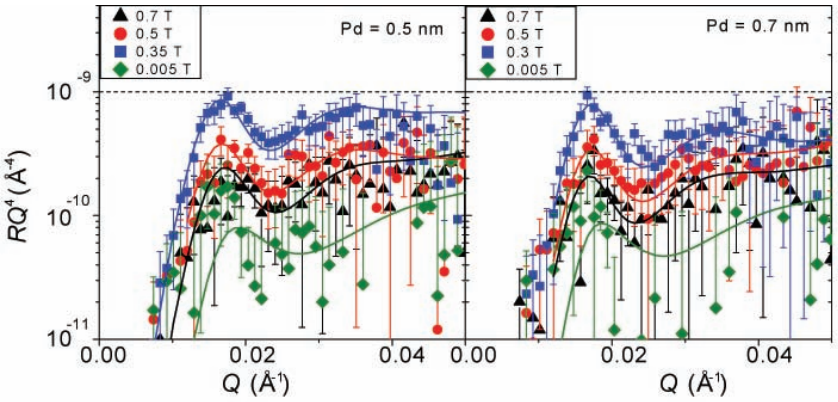

FIGURE 2: Comparison of the average spin-flip reflectivity data for films with Pd thicknesses of 0.5 nm (left) and 0.7 nm (right). The increase in SF reflectivity at intermediate fields corresponds to in-plane moments, consistent with domain wall formation.

Figure 3 summarizes the results. Left to right, the cartoon displays the domain wall originating at the top surface, with the Co layer moment parallel to the field, and extending to the layer near the TbFeCo interface, with moments

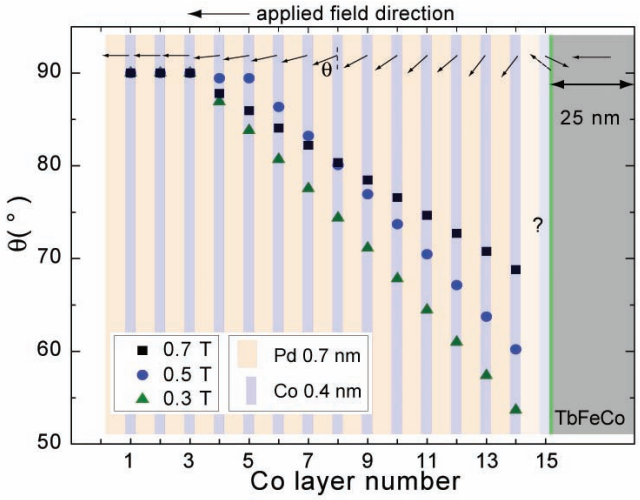

FIGURE 3: Moment angle vs CoPd layer number for various applied fields. At lower fields, the moment projects more into the plane. The magnetic behavior in layer 15 is uncertain, presumably due to inhomogeneity of the magnetization across the sample plane. The green line indicates a 1.4 nm layer at the TbFeCo/Co interface in which the moment reverses direction to line up with the net moment in the TbFeCo (grey) region which is aligned with the applied field.

gradually tipping away from the field. At this interface (i.e., Co layer number 15), the in-plane moment component changes abruptly, presumably due to the competition between the field and the strong, local AF coupling between the Co and TbFeCo base. The figure also illustrates that the in-plane projection of the moment increases in magnitude with decreasing field as expected because the AF coupling should gradually overcome the torque of the applied field.

In conclusion, PNR results confirm the formation of an in-plane domain wall as indicated by the magnetization and magnetoresistance measurements. The extent and depth of the domain wall vary with the exchange stiffness of the Co-Co interaction of the Co/Pd bilayers and with the applied field. Further, we were able to isolate the field-dependence of the domain wall spiral using a novel measurement geometry. Though neutron reflectivity measurements are not directly sensitive to moments perpendicular to the sample plane, this new configuration provides a means to indirectly gather information on the out-of-plane moment component. Our results thus open the door for future investigations of the depth-dependent magnetic structure in perpendicular recording media.

References

[1] D. C. Crew and R. L. Stamps, J. Appl. Phys. **93** (10), 6483 (2003).
[2] G. Asti *et al.*, Phys. Rev. B **73**, 094406 (2006).
[3] S. Mangin *et al.*, J. Appl. Phys. **89** (11), 7203 (2001).

Discovery of Zone Boundary Soft Modes in the Relaxor Ferroelectric PMN

I. P. Swainson[1]; C. K. D. Stock[2]; P. M. Gehring[3]; G. Xu[4]; H. Luo[5]

Piezoelectrics are solids that have the ability to convert mechanical energy into electrical energy and vice-versa. When a piezoelectric crystal is squeezed, a voltage is generated across the opposite faces of the crystal. When an external voltage is applied, the crystal dimensions distort. This effect is extremely important, finding use in sonar, ultrasound imaging, microphones, and computer hard drives. The lead oxide perovskites $Pb(Mg_{1/3}Nb_{2/3})O_3$ (PMN) and $Pb(Zn_{1/3}Nb_{2/3})O_3$ (PZN) belong to a novel class of materials known as "relaxors" that possess ultrahigh piezoelectric properties that far surpass those of $PbZr_xTi_{1-x}O_3$ (PZT) ceramics, which have long been the material of choice for use in commercial devices. When either PMN or PZN is combined with small amounts of $PbTiO_3$, which is a conventional ferroelectric, the piezoelectric properties are enhanced to record-setting levels, making these materials enormously attractive for industrial, medical, and military applications. But beyond a certain level of $PbTiO_3$ the piezoelectric properties drop precipitously [1]. While different ideas have been proposed to explain these anomalous relaxor properties, no consensus exists.

Pure PMN and $PbTiO_3$ share many static and dynamic features. Of particular note is the fact that both exhibit a low-frequency, transverse optic (TO) soft phonon at the zone center [2], which in the case of $PbTiO_3$ drives the cubic-to-tetragonal ferroelectric transition at 763 K. While the TO mode in $PbTiO_3$ never softens completely because the transition is first order, PMN exhibits no such transition, retaining an average cubic unit cell down to 4 K; instead, the TO phonon in PMN becomes extremely broad in energy on cooling from 900 K. A simultaneous broadening of the transverse acoustic (TA) phonon in PMN that tracks that of the TO phonon is also observed upon cooling. Intriguingly, the damping of both phonons vanishes near the nominal Vogel-Fulcher freezing temperature $T_f \approx 220$ K. Also intriguing is the fact that the TO phonon frequency in PMN increases with cooling below T_f in a manner consistent with that expected for a conventional ferroelectric.

To further our understanding of the complex lattice dynamics of relaxor materials, measurements were made on a large (8 cm^3) single crystal specimen of the prototypical relaxor PMN at 300 K and 600 K over a broad region of reciprocal space using the neutron time-of-flight scattering technique. The PMN crystal was oriented in the [*HHL*] zone and mounted inside a closed-cycle ^{4}He refrigerator with access to temperatures from 30 K to 650 K. The neutron scattering measurements were performed on the NCNR Disk Chopper Spectrometer to characterize the low-frequency lattice dynamics along the major symmetry directions Γ–Λ–R, Γ –Σ–M, and Γ –Δ–X (see the inset of Fig. 1).

Fig. 1 shows an intensity map of the neutron inelastic scattering measured at 300 K along the reciprocal lattice direction [1.5 1.5 *L*], corresponding to a scan along the transect M-T-R edge of the Brillouin zone. These data reveal a truly remarkable feature that is indicated by the strong "column" of inelastic scattering located at the M-point zone boundary at (1.5 1.5 -1), which extends all the way from -5 meV to the elastic line. Similar, but weaker, columns of inelastic scattering are visible at R-point zone boundary locations as well, such as (1.5 1.5 -0.5). The excitations at both the R and M-points are well defined in momentum, but also extremely broad in energy, indicating a highly periodic form of disorder. At 600 K the intensities of all columns weaken considerably; this behavior strongly implies the presence of soft zone boundary modes that are most likely the origin of the temperature-dependent superlattice peaks

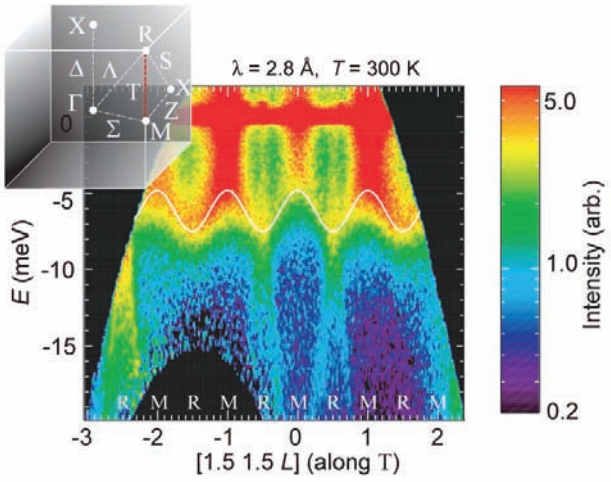

FIGURE 1: Neutron scattering intensity map measured on DCS at 300 K on a single crystal of PMN. The figure is a slice along [1.5 1.5 *L*] and shows a continuous dispersion between the M and R-points along T. Note the strong continua of inelastic scattering that extend to the elastic position from the M-point modes and the weaker continua located at the R-points. The curve is a guide to the eye. Inset: Brillouin zone (BZ) of the primitive cubic form of the perovskite PMN, along with some high-symmetry points and lines. The one symmetrically-distinct edge along M-T-R is shown in red.

[1]Chalk River Labs, Chalk River, Ontario K0J 1J0, Canada
[2]Johns Hopkins University, Baltimore, MD 21218
[3]NIST Center for Neutron Research, National Institute of Standards and Technology, Gaithersburg, MD 20899
[4]Brookhaven National Laboratory, Upton, NY 11973-5000
[5]Shanghai Institute of Ceramics, Chinese Academy of Sciences, Shanghai, China 201800

that have been observed in both x-ray [3] and neutron measurements, as shown in Fig. 2 [4]. Such zone boundary soft modes have never been reported in any relaxor material before.

The data in Fig. 1 demonstrate continuity along the line M-T-R thus implying that the scattering intensities visible at the M and R-point zone boundaries have a common origin. The fact that the modes at M and R appear to be zone boundary acoustical ones would seem to indicate that these are the well-known oxygen octahedral tilt modes. However, preliminary neutron structure factor calculations suggest that the corresponding ionic displacements instead involve the Mg/Nb and Pb atoms. This picture is consistent with prior x-ray studies according to which the superlattice peaks are created by anti-parallel Pb displacements correlated along <110> cubic directions [3]; moreover, neutron data show that in-phase oxygen octahedra rotations, to which x-rays are much less sensitive, do not contribute to the intensities of peaks of the form ½(h h 0). Further analysis is being done to identify the eigenvectors associated with these modes.

Based on the ionic displacements and the broad linewidths, the superlattice peaks are believed to represent *antiferro*distortive nanoregions roughly 3 nm in size. X-ray measurements have also demonstrated that the onset of the superlattice peak intensity occurs at the Vogel-Fulcher freezing temperature T_f [3]. This establishes a direct connection between the macroscopic dielectric properties and local crystal structure of PMN. The potential relationship between the columns of inelastic scattering and the superlattice peaks in PMN is therefore intriguing because the temperature dependence of the M-point superlattice peak shown in Fig. 2 nearly tracks that of the zone center soft optic mode [2], which is associated with the development of short-range *ferro*electric correlations at low temperatures. PMN is also well-known to develop local regions of ferroelectric order known as polar nanoregions at high temperature that give rise to strong diffuse scattering around various Bragg peaks. The presence of both ferroelectric and antiferrodistortive nanoregions, both of which exhibit correlations of roughly 3 nm to 5 nm, suggests a complex interplay between these competing orders that may explain the unusual relaxor properties of PMN.

The discovery of strong columns of inelastic scattering located at the M and R-point zone boundaries in PMN is significant because it implies a dynamical origin to the superlattice peaks, which exhibit a temperature dependence consistent with macroscopic dielectric properties. Of equal significance is the fact that these columns of inelastic scattering are *not* observed in either $PbTiO_3$ or in PMN doped with a mole fraction of 60 % $PbTiO_3$, both of which possess tetragonal, ferroelectric ground states with markedly smaller piezoelectric properties. While not well understood, the relaxor properties of PMN are believed to stem from random fields associated with the structural disorder of the perovskite B-site that is shared by the heterovalent ions Mg^{2+} and Nb^{5+}. Quenched random fields likely give rise to an unusually anharmonic free energy surface for which higher order expansion terms are significant, thereby admitting many different polar phases. If the free energy surface is sufficiently flat along directions that connect these phases, then the huge piezoelectric properties can be understood by the ease with which the system can be switched between states of different polar order. The neutron data support such a picture inasmuch as the coexistence of soft modes at multiple zone boundaries and the zone center, and the coexistence of short-range ordered regions of ferroelectric and antiferrodistortive character, imply that PMN lies energetically close to states with competing polar order such that the application of a small external voltage could produce the observed ultrahigh piezoelectric reponse.

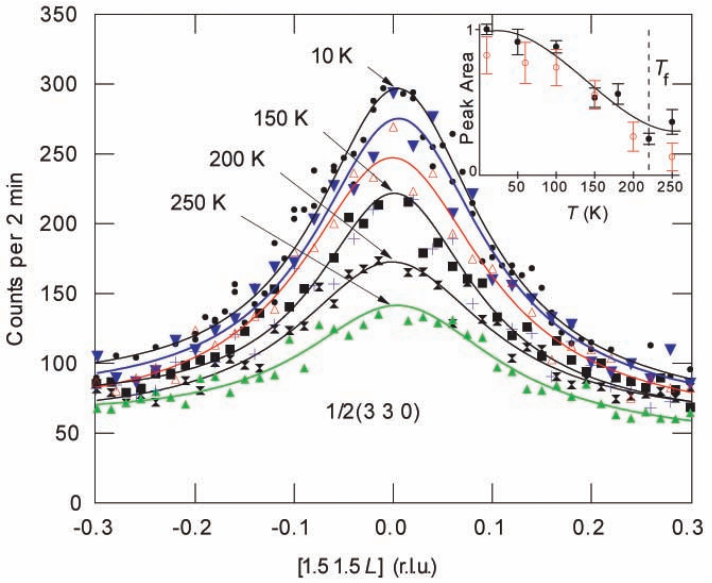

FIGURE 2: Elastic scattering intensity profiles measured at the M-point 1/2(3 3 0) with thermal neutrons along [001] from 10 K to 250 K. The abbreviation r.l.u. stands for reciprocal lattice units. The inset shows the temperature dependence of the *L*-integrated intensities at 1/2(3 3 0) (filled circles) on cooling and at the symmetry equivalent peak ½(-3 -3 0) (open circles) on heating. The Vogel-Fulcher freezing temperature T_f is indicated by the vertical dotted line.

References

[1] S.-E. Park and T. R. Shrout, J. Appl. Phys. **82**, 1804 (1997).

[2] G. Shirane, J. D. Axe, J. Harada, and J. P. Remeika, Phys. Rev. B **2**, 155 (1970); P. M. Gehring, S. Wakimoto, Z.-G. Ye, and G. Shirane, Phys. Rev. Lett. **87**, 277601 (2001).

[3] A. Tkachuk and H. Chen, AIP. American Institute of Physics Conference Proc., edited by Peter K. Davies and David J. Singh, Williamsburg, VA, **677**, p. 55 (2003).

[4] A. Tkachuk and P. M. Gehring, in preparation.

Hidden Order in URu_2Si_2

J. A. Janik, C. R. Wiebe[1]; G. J. MacDougall, G. M. Luke[2]; J. D. Garrett[3]; H. D. Zhou, Y.-J. Jo, L. Balicas[4]; Y. Qiu, J. R. D. Copley[5]; Z. Yamani, W. J. L. Buyers[6]

The unique properties of correlated electron materials, such as high-temperature superconductors, geometrically frustrated magnetic oxides and low dimensional magnets, arise from many-body effects which are poorly understood. Heavy-fermion metals – materials that have high effective electron masses due to these effects – display a variety of exotic properties ranging from unusual magnetism, unconventional superconductivity and 'hidden' order parameters. The heavy-fermion URu_2Si_2, which becomes superconducting at $T_c = 1.3$ K at ambient pressure and zero magnetic field, exhibits a 'hidden-order' (HO) phase starting well above this at an ordering temperature $T_0 = 17.5$ K, but well below the 'coherence temperature' (≈ 70 K) for the formation of heavy-fermion excitations. The central issue in URu_2Si_2 concerns the identification of the order parameter that explains the reduction in the specific heat coefficient, $\gamma = C/T$, and thus the drop in entropy through the transition at T_0. Earlier neutron scattering measurements indicated that the ordered moment is $0.03\mu_B$, much too small to account for this change. Here we highlight NCNR Disk Chopper Spectrometer measurements uncovering a new piece of this puzzle that accounts for a significant portion of the entropy change.

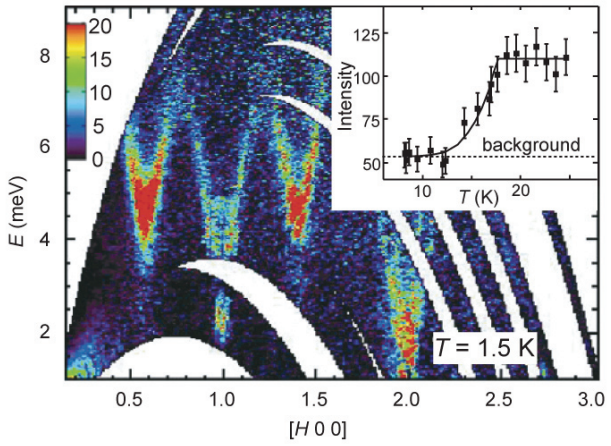

FIGURE 1: Inelastic neutron scattering of URu_2Si_2 showing the excitation spectrum in the [H 0 0] plane at $T = 1.5$ K (where H and L are integers multiplying reciprocal lattice vectors a^* and c^*; L is integrated from −0.12 to 0.12). Note the minimum at the AF zone center [1 0 0] and at the incommensurate positions [1±0.4 0 0]. The feature at [2 0 0] is due to phonons. The inset shows the intensity obtained by counting at the point [0.6 0 0] at 0.25 meV energy transfer on a triple-axis spectrometer and demonstrates the development of a gap in the incommensurate excitations through the transition. The error bars are determined by the square root of the intensity.

We carried out experiments above and below the ordering temperature to measure how the spin excitations evolve. Figure 1 shows the excitation spectrum in the [H 0 0] plane of URu_2Si_2 at 1.5 K, well below T_0. Note the characteristic gaps of 2 meV at the AF zone center [1 0 0] and 4 meV at the incommensurate wavevectors [0.6 0 0] and [1.4 0 0]. The incommensurate wavevector corresponds to a displacement of $0.4a^*$ from the AF zone centers (that is, where $(H + K + L)$ is an odd integer, and is thus forbidden in the body-centered cubic chemical structure.) It is clear from our data (shown in Fig. 2) that above T_0 the spectrum is dominated by fast, itinerant-like spin excitations emanating from these incommensurate wavevectors. From the group velocity and temperature dependence of these modes, we surmise that these are heavy-quasiparticle excitations that form below the coherence temperature and play a crucial role in the formation of the heavy-fermion and HO states.

These excitations have a structure in reciprocal space such that they occur at several symmetry-related wavevectors within the first Brillouin zone. The amount of phase space occupied by these excitations is greater than those at the [1 0 0] AF zone center. Figure 2 shows constant energy cuts of the excitations in the [H 0 L] plane to emphasize this. At $T = 20$ K note the weak AF fluctuations at [1 0 0] and [2 0 1] in comparison with the excitations at the incommensurate positions. Also, note how a cone of scattering develops at the incommensurate positions, whereas the AF zone center simply decreases in intensity as energy transfer is increased. The results at 20 K suggest a continuum of excitations within a cone of scattering (as expected for low-lying excitations at the Fermi surface), as opposed to the sharp excitations that are gapped below 17.5 K, shown for comparison in Fig. 2a at 1.5 K.

It is the opening of an energy gap in these incommensurate heavy-quasiparticle excitations as they fall into a condensate below T_0 which makes them less accessible to thermal fluctuations. This accounts for a significant portion of the reduction in entropy below the specific heat jump-like anomaly at 17.5 K, as described in Fig. 3.

[1]Florida State University, Tallahassee, FL 32306 and National High Magnetic Field Laboratory, Tallahassee, FL 32310
[2]McMaster University, Hamilton, Ontario L8S 4M1, Canada
[3]Brockhouse Institute for Materials Research, McMaster University, Hamilton, Ontario L8S 4M1, Canada
[4]National High Magnetic Field Laboratory, Florida State University, Tallahassee, FL 32310
[5]NIST Center for Neutron Research, National Institute of Standards and Technology, Gaithersburg, MD 20899
[6]Chalk River Labs, Chalk River, Ontario K0J 1J0, Canada

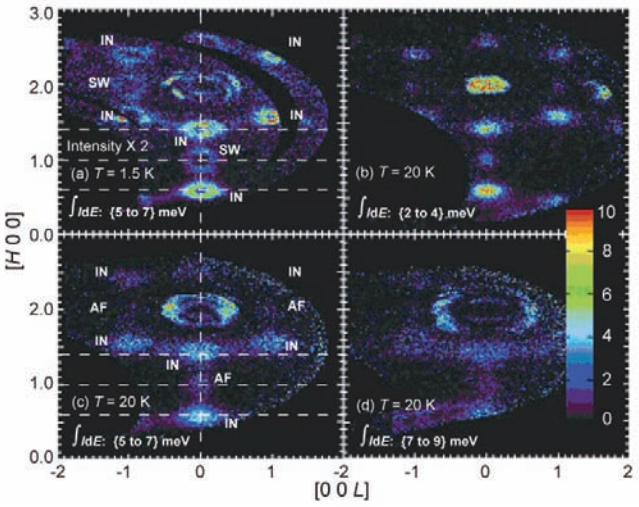

FIGURE 2: Energy cuts in the [*H* 0 *L*] plane showing the evolution of inelastic scattering in URu_2Si_2: below T_0 at 1.5 K in (a), and above T_0 at 20 K in (b) to (d). The rings at [2 0 0] correspond to phonons. The rings marked "SW" at 1.5 K centered on $(H + K + L)$ = odd integers (AF zone centers) are spin waves. Note the rings marked "IN" centered at incommensurate points separated by $0.4a^*$ from the AF zone centers in all panels. While there are weak overdamped AF fluctuations at the zone centers at 20 K, it is clear that at the incommensurate positions cones of highly correlated excitations develop as a function of energy. Comparing (c) with (a), the incommensurate excitations in the same energy cut display a ring, i.e., have a smaller group velocity, below T_0 than above where they display a cone.

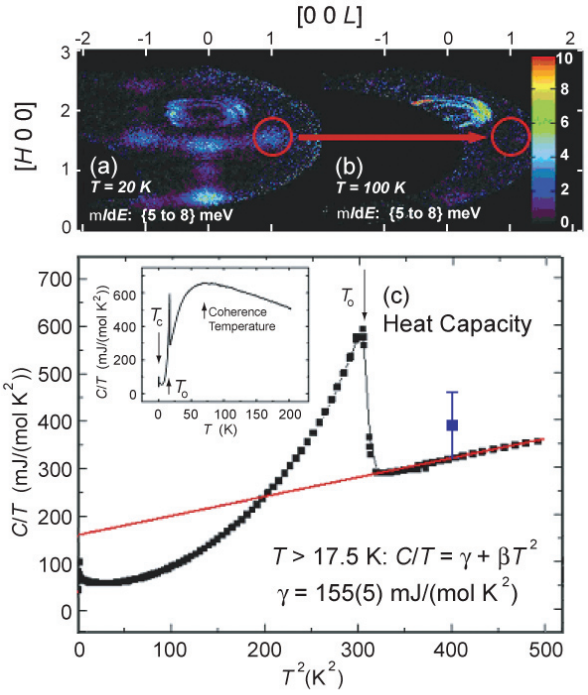

FIGURE 3: Correlations with features in the specific heat. (a) and (b), cuts in the [*H* 0 *L*] plane integrated from 5 meV to 8 meV at 20 K in (a), and at 100 K in (b). The incommensurate scattering at positions such as [1.6 0 1] disappears at 100 K (indicated by a circle). This is just above the 'coherence' temperature where a signature of heavy-quasiparticle formation is seen in the specific heat (inset in (c)). (c), the specific heat *C* divided by temperature as a function of *T*, showing the jump-like anomaly at 17.5 K. The linear portion of the specific heat, γ, is calculated with the solid line to be 155(5) $mJmol^{-1}\ K^{-2}$. The blue data point is our calculation of $\gamma = 220(70)\ mJ\ mol^{-1}\ K^2$ from the incommensurate spin fluctuations observed at 20 K.

The implications of our work are as follows: (1) the incommensurate excitations have a well-defined structure as a function of Q, and thus the electrons are highly correlated above 17.5 K. This is completely unexpected for a system of localized moments in a paramagnetic state, but is similar to dynamics above the Néel temperature, T_N, that have been observed with neutron scattering in other itinerant electron systems such as chromium and V_2O_3. (2) The dispersion is such that the maximum group velocity is at least a factor of two larger than the maximum group velocity of the excitations in the HO state. A significant restructuring of the Fermi surface must be responsible for the HO state. (3) The energy gap in these strong spin fluctuations opening up below 17.5 K must provide a considerable portion of the entropy removal at the transition.

Our findings place constraints on all new theories of HO in URu_2Si_2. A minimum theory must account for (1) incommensurate itinerant spin excitations and (2) the lack of crystalline electric fields up to 10 meV. The HO transition seems to be a rearrangement of electrons at the Fermi surface in an itinerant rather than localized electron picture. Excitations out of this state at these incommensurate wavevectors show a mode-softening that is reminiscent of another dynamic ground state that has no translational order but a prominent specific-heat anomaly—the superfluid liquid helium transition.

Correlations between the heavy quasiparticles in URu_2Si_2 build up below 100 K, and at 17.5 K, there is a transition to a new condensate that remains unidentified. The true order parameter for this system has yet to be determined.

References

[1] C. R. Wiebe, *et al.*, Nature Physics **3**, 1 (2007).
[2] Z. Fisk, *et al.*, Science **239**, 33 (1988).
[3] C. Broholm, *et al.* Phys. Rev. B **43**, 12809 (1991).
[4] C. R. Wiebe, *et al.*, Phys. Rev. B **69**, 132418 (2004).
[5] H. Chou, *et al.*, Phys. Rev. B **43**, 5554 (1991).

Quantum Coherence in a Spin Chain

G. Xu[1,2]; C. Broholm, Y. Chen, M. Kenzelmann[1,3]; Y.-A. Soh[4]; G. Aeppli[5]; J. F. DiTusa[6]; C. D. Frost[7]; T. Ito, K. Oka[8]; H. Takagi[8,9]

Superconductivity spectacularly displays quantum phase coherence on a macroscopic length scale. Quantum effects are more usually associated with physics on the atomic scale. Here we report quantum coherence among the magnetic dipoles of Ni^{2}+ in crystalline Y_2BaNiO_5 at a length scale (hundreds of atoms) being approached in integrated circuit devices. Using neutrons, we also demonstrate that the coherence length can be modified by static and thermally activated defects in a quantitatively predictable manner. The observation of quantum coherence beyond the atomic scale in a magnetic material exhibiting no classical long range order is a surprising first, and betters prospects for applications in quantum computing.

A perfectly coherent wave is one in which the wave fronts lie on planes and appear periodically in time. In more complex waves, coherence is measured over the finite distance (or time) over which correlations in phase are more or less well-defined. Quantum phase coherence describes the coherence properties of the wave-function. With quantum coherence comes all the beauty and mystery of quantum mechanics, including interference, uncertainty and especially entanglement, a property central to the development of quantum computation. Typically, interaction with the environment limits quantum coherence. The experimental conditions under which quantum coherence can transcend the atomic scale and acquire technological importance remain a major pursuit of applied physics.

Fig. 1A provides experimental evidence that this *does* occur in the one dimensional antiferromagnet Y_2BaNiO_5. The sharp intensity ridge is the experimental signature of coherence: a well defined relationship between the spatial periodicity (horizontal axis) and temporal periodicity (vertical axis) in the excited state wave function. To quantify the degree of coherence, we focus on the lowest energy excitation marked by an intense red peak in the data. It corresponds to the creation of a magnon with crystal momentum $q = \pi$ through interaction with a neutron. Fig. 2B shows an energy-cut through the peak obtained with high resolution on the SPINS spectrometer. The sharp initial onset sets a limit of 0.1 meV on the relaxation rate indicating that the wave function remains coherent through 100 periods of its temporal oscillation. The three peaks result from crystalline anisotropy and finite resolution yields

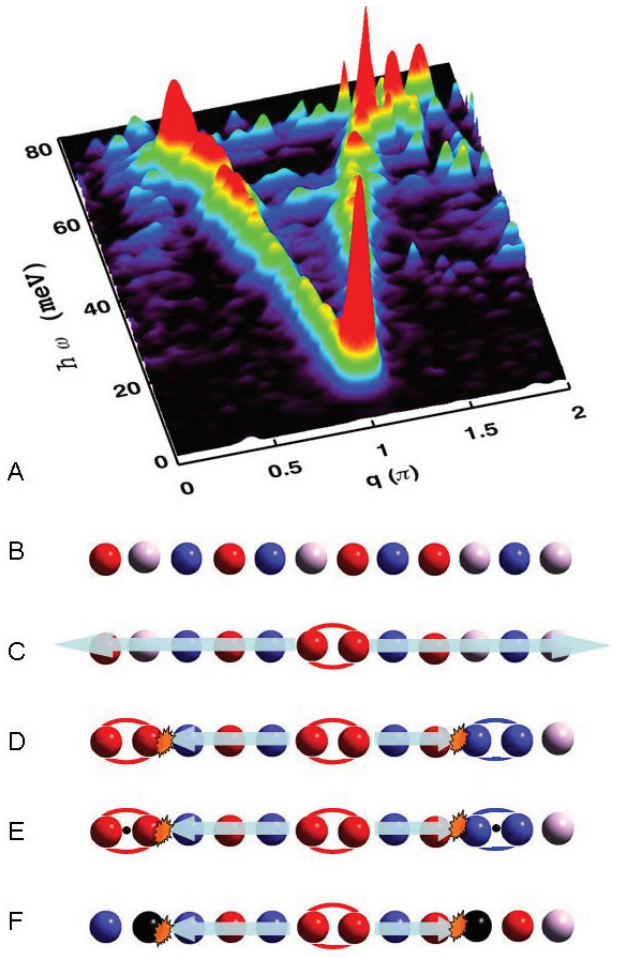

FIGURE 1: **A**: Map of neutron intensity multiplied by energy for Y_2BaNiO_5 at $T = 10$ K acquired on MAPS at the ISIS facility. **B-F**: Diagrams of quantum order in Y_2BaNiO_5. The red, white, and blue spheres represent sites with spin projection quantum numbers 1, 0 or -1. Impurities are represented by black spheres. **B**: Pure $S = 1$ chain at $T = 0$. **C**: Magnon excitation; **D**: at $T > 0$, thermally excited magnons confine each other into boxes. **E**: Confinement by Ca impurities, which introduce holes (small black spheres) into the chain and align neighboring spins. **F**: Confinement by non-magnetic Mg impurities.

the high energy tail. The solid symbols in Fig. 2D show the corresponding fixed energy cut versus q. After accounting for resolution, the intrinsic peak width is just 0.02 π and this indicates quantum coherence encompassing up to 100 nickel

[1]The Johns Hopkins University, Baltimore, MD 21218
[2]Brookhaven National Laboratory, Upton, NY 11973
[3]NIST Center for Neutron Research, National Institute of Standards and Technology, Gaithersburg, MD 20899
[4]Dartmouth College, Hanover, NH 03755
[5]University College London, London, WC1H 0AH, UK
[6]Louisiana State University, Baton Rouge, LA 70803
[7]ISIS Facility, Rutherford Appleton Laboratory, Chilton, Didcot OX11 0QX, UK
[8]National Institute of Advanced Industrial Science and Technology, Tsukuba, Ibaraki 305-8562, Japan
[9]University of Tokyo, Kashiwa, Chiba 277-8561, Japan

atoms. Also shown is the equal time correlation length: the classical distance over which probing one spin also reveals neighboring spin states.

To employ quantum coherence we must understand its practical limits, so we examined the effects of thermal and chemical defects. Fig. 2C shows that the coherence length decreases precipitously upon heating until it becomes indistinguishable from the classical correlation length when the thermal energy matches the gap energy. The solid line shows the calculated temperature (T) dependent distance from a random location along the chain to the nearest thermal or chemical defect, assuming a chemical defect density consistent with low temperature susceptibility data and a semi-classical description of magnons. Encouraged by the excellent agreement, Figs. 1 B-F illustrate the corresponding interpretation of coherence and its limitations in Y_2BaNiO_5. A measurement of the projection of the Ni^{2+} dipole moment along any chosen direction has three possible outcomes. Select a specific direction and indicate by red white and blue which of the three states is assumed by each spin. Theory indicates that the ground state of an antiferromagnetic spin-1 chain consists of alternating red and blue spheres with white spheres inter-dispersed at random. The classical correlation length can be considered a measure of the average spacing between white spheres. Though such a state appears disordered to the classical observer (Fig. 1 B), it is in fact a perfectly coherent quantum state as indicated by our observation of coherent excitations (Fig. 1A). Fig. 1C indicates the nucleus of an excitation in the form of a pair of red spheres that propagate coherently. The finite T and doping experiments indicate that coherence is limited by scattering from thermally (Fig. 1D) or chemically (Fig. 1E-F) induced defects.

The experiments described thus far show that heating and doping limit quantum coherence. Particular to one dimension is the confining effect of chemical impurities which according to Heisenberg uncertainty principle ($\Delta p \bullet \Delta x \geq \hbar/2$) should increase kinetic energy ($p^2/2m$). Might the analogy between thermal and chemical impurities extend to this fundamental quantum effect? Figure 2A shows the T dependence of the energy, Δ, associated with creating a $q = \pi$ magnon. It is indeed found to increase with T, which is qualitatively consistent with confinement by thermally generated defects (Fig. 1D). Moreover, the red points in Fig. 2A show the corresponding excitation energy in chemically impure samples at $T = 10$ K with defect density given by the upper axis. This axis was chosen in accordance with the solid line in Fig. 2C so the chemical defect density matches the thermal defect density corresponding to the lower axis. Data points from chemically and thermally doped samples fall on the same line which in turn was obtained from exact diagonalization of finite length spin chains. We have thus established that chemically and thermally induced defects lead to blue shift through confinement.

While quantum spin chains with a gap have a finite classical correlation length, our experiments show that

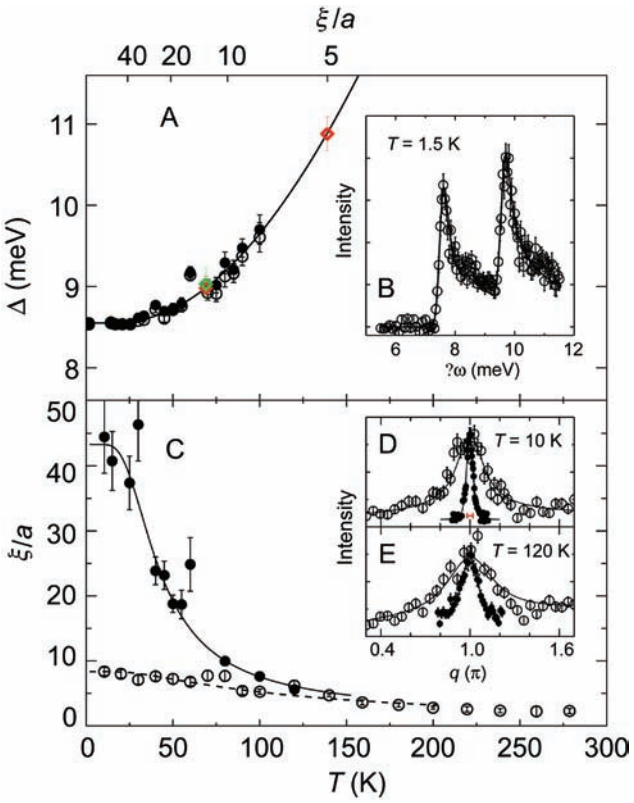

FIGURE 2: **A**: T dependence of the $q = \pi$ magnon energy in Y_2BaNiO_5. Diamonds indicate low T excitation energies in samples with chemical impurities at the average spacing indicated by the upper axis. That axis shows the calculated thermal defect spacing at the temperature given by the lower axis. **B**: $q = \pi$ energy scan from SPINS. The solid line is the resolution convolved intensity associated with a triplet of magnons split by crystalline anisotropy. The gap, Δ, reported in **A** is the average of these mode energies. **C**: T dependence of the classical correlation length (open symbols) and the quantum coherence length (closed symbols) extracted by fitting data such as those in **D** and **E**. Solid and dashed lines are theoretical results [1]. **D** and **E**: Solid symbols are cuts through neutron data for $\hbar\omega = 7.5$ meV probing quantum coherence. Red line is resolution width. Open symbols indicate energy integrated data ($\hbar\omega > 8$ meV) probing classical correlations. Data are from BT-2 and BT-4.

the coherence of excited states is limited only by thermal and chemical disorder. Both effects are accounted for by a semi-classical theory of magnons scattering from each other and from chemical defects. The experiments demonstrate that quantum phase coherence can be achieved in a solid state magnet at length scales that approach feature sizes in modern integrated circuits, thus removing one of many barriers towards applications in quantum computing.

References

[1] G. Xu, *et al.*, www.sciencexpress.org/10.1126/science.1146067.

The Nanoscale Building Blocks of Concrete

A. J. Allen[1]; J. J. Thomas, H. M. Jennings[2]

Concrete, the most widely used manufactured material, has moved one step closer to joining the nano revolution that is reshaping the use of many materials. The most important binding phase in cement paste, calcium silicate hydrate (C-S-H), has a structure at the nanometer scale that is directly related to concrete properties, but the structure of this phase, and in particular the composition and density, have proven remarkably difficult to determine. By combining small angle neutron and x-ray scattering data, and by exploiting the hydrogen/deuterium neutron isotope effect with both water and methanol, we have established the mean formula and mass density of the nanoscale C-S-H gel particles [1].

The disordered and complex structure of C-S-H, which includes a nanometer-scale pore system that normally is filled with water, changes significantly on drying, rendering the results of most modern techniques the subject of extensive interpretation. During the last decade the results from a variety of neutron scattering experiments have shed light on several characteristics of C-S-H in its normal, water-saturated state. In particular, small-angle neutron scattering (SANS) measurements on cement paste indicate that the nanometer-scale structure consists of solid particles or "globules" of

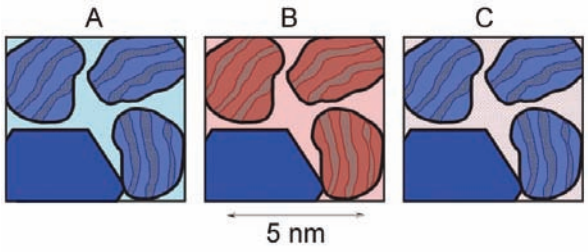

FIGURE 1: Schematic diagram of nanoscale hydration product in cement paste, consisting of layered C-S-H particles (striped images) and $Ca(OH)_2$ crystals surrounded by pore fluid. Three fluid exchange scenarios are shown. Phases containing only hydrogen are blue, while phases containing deuterium are red. The black lines indicate the scattering interface between the solid phases and the pore fluid. A) Normal saturated paste with H_2O in the pores. Due to its small volume fraction, scattering from nanoscale $Ca(OH)_2$ is almost negligible compared to that from C-S-H. B) A D_2O-exchanged paste. The C-S-H exchanges with OD^- groups to become C-S-D, while the $Ca(OH)_2$ is unchanged. Compared to case A, the scattering between $Ca(OH)_2$ and the pore fluid is much stronger, while scattering between C-S-D and the pore fluid is much weaker. Experiments with D_2O exchange allow the volume fraction of nanoscale $Ca(OH)_2$ to be determined. C) A paste exchanged with d3-methanol (CD_3OH). Since the fluid does not contain OD^- groups, only the pore phase changes. Both C-S-H and $Ca(OH)_2$ scatter strongly with CD_3OH and the scattering length density of the overall C-S-H/ $Ca(OH)_2$ nanoscale solid phase can be determined. By combining this result with the $Ca(OH)_2$ volume fraction obtained from D_2O exchange (Case B), and with SAXS data, the neutron and X-ray scattering length densities, composition, and mass density of the C-S-H phase can be determined.

C-S-H that are packed randomly to form a continuous phase through the paste, binding the cement particles together. The globules and associated water are shown schematically in Fig. 1a (striped images). Much has been learned [2-4], including the characteristic size of the globules (4 nm to 5 nm), their fractal arrangement and packing density, and the specific surface area of the paste. In addition, quasi-elastic neutron scattering (QENS) measurements have determined the relative amounts of chemically bound, adsorbed, and liquid water within hydrated cement paste [5]. What was not known until quite recently [1] is the water content and mass density of the solid C-S-H globules, the basic building blocks of the hydrated microstructure.

SANS is ideal for investigating the nanostructure of disordered wet materials such as cement paste. The intensity of the scattering at a given scattering vector, Q, depends on the amount of structure in the associated size range, but is also directly proportional to the square of the difference in the neutron scattering length densities (SLD) of the scattering phases, a factor called the scattering contrast. If the chemical composition and mass density of both phases are known, the contrast can be calculated precisely. This is not the case for the C-S-H phase in cement, however: the unknown water content and density of solid C-S-H is a longstanding issue of importance in cement science that also hinders a full interpretation of scattering data. The problem of an unknown solid phase can often be solved by varying the SLD of the liquid phase by replacing it with a deuterated fluid, in this case by exchanging the pore H_2O with varying amounts of D_2O (heavy water), which has a much higher SLD. By noting the matchpoint where the contrast drops to zero, the solid SLD and solid-H_2O contrast can in principle be calculated directly.

Two problems with this approach arise for cement-based materials. The presence of a small amount of nanoscale $Ca(OH)_2$ intermixed with C-S-H means that a zero-intensity contrast matchpoint does not exist, since $Ca(OH)_2$ has a matchpoint quite different from that of C-S-H. More important, solid C-S-H undergoes full H/D exchange to become C-S-D (see Fig. 1b), adding an additional level of complexity. The volume fraction of $Ca(OH)_2$ in various types of cement paste can be determined by analyzing the contrast variation parabolas (plotted as curves of scattered intensity versus D_2O fraction). The scattering contribution from $Ca(OH)_2$ can then be subtracted, leaving a self-consistent C-S-H contrast curve for H_2O/D_2O contrast experiments. The problem now is that this curve is actually for C-S-H/D as D exchanges for H, where both the solid and liquid SLD are changing, and

[1]Ceramics Division, National Institute of Standards and Technology, Gaithersburg, MD 20899
[2]Northwestern University, Evanston, IL 60208

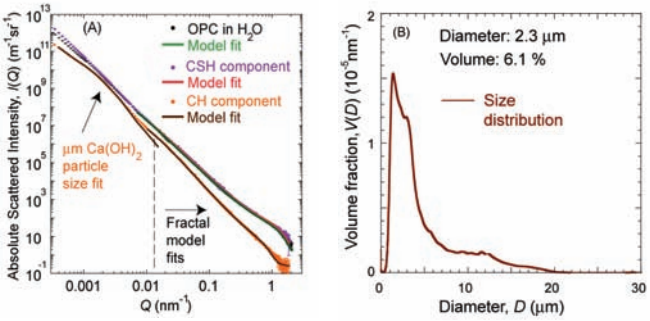

FIGURE 2: A) Combined SANS and USANS data for hydrated ordinary Portland cement (OPC), the decomposition of the scattering into its C-S-H and calcium hydroxide (CH) components, and both fractal and particle size fits to the high-*Q* and low-*Q* parts of the data as shown. B) Micrometer-scale calcium hydroxide crystallite size distribution (volume fraction per diameter interval) derived from maximum-entropy analysis of the low-*Q* $Ca(OH)_2$ data component.

no unique solution is possible if both the composition and density of C-S-H are unknown.

Providing constraints that define and refine the scattering length density of C-S-H solves this problem. Important information is obtained from SANS contrast data using CH_3OH/CD_3OH exchange: since CD_3OH does not contain OD groups, the OH groups in solid C-S-H remain OH, and only the fluid phase exchanges (see Fig. 1c). Thus, the SLD for the combined C-S-H/$Ca(OH)_2$ nanostructure can be calculated from the ratio of the SANS intensities in CH_3OH and in CD_3OH [1]. Another constraint comes from comparing SANS and small-angle x-ray scattering (SAXS) data from identical pastes on an absolute-calibrated intensity scale. Careful experiments of this nature have provided new and precise information about the important C-S-H phase in cement. While the calcium/silicon (C/S) molar ratio can vary over a wide range, it is well established at about C/S = 1.7 for C-S-H formed in normal cement paste. With this ratio held fixed, the combined SANS contrast and SAXS data provide an over-determination of the two remaining unknowns to give a water-to-silicon molar ratio, H/S = 1.80 ± 0.03, and a physical density of (2.604 ± 0.022) x 10^3 kg m^{-3} [1]. The H/S ratio of 1.80 represents the water content of the C-S-H particles themselves, and does not include any adsorbed water outside the particles. This interpretation provides a framework for reconciling C-S-H water contents obtained by a variety of different measurements, some of which are quite different from the value reported here.

In a system with a liquid phase and two solid phases, adjusting the liquid SLD to match that of one solid phase, a process known as contrast matching, causes the scattering from the matched phase to disappear, such that the measured scattering arises only from the other solid phase. Such experiments, which also incorporate data from ultrasmall-angle neutron scattering (USANS), have enabled the $Ca(OH)_2$ component in cement paste to be distinguished from the rest of the microstructure, both in its nanoscale form and in its better-known form as micrometer-scale crystallites. Applying all of the constraints allows the SANS (or SAXS) scattering curves for cement to be decomposed into the constituent components associated with the C-S-H and $Ca(OH)_2$ microstructures over the nanometer-to-micrometer scale range, as shown in Fig. 2A, and then reassembled to predict the overall scattering curves obtained for different H_2O/D_2O mixes.

While the SANS and USAXS data have been quantitatively interpreted using multi-component fractal models previously, the new information provides a much firmer basis for the absolute calibration of the microstructural information obtained. However, the USANS data extends such calibration up into the tens of micrometer length-scale. This has been sufficient to apply more conventional particle size measurement to the $Ca(OH)_2$ component, and determine, for the first time, the micrometer scale $Ca(OH)_2$ size distribution, within set cement, on the same absolute scale as the fractal information obtained at finer length-scales, as indicated in Fig. 2B.

The nanometer-scale globules of C-S-H are the basic building blocks of all cementitious materials. Having established the their composition and density in normal cement paste, the door is now open to modeling changes that occur under a host of environmental and mechanical influences. This is particularly important because new demands are being placed on this ancient yet irreplaceable material at an accelerating rate. For examples, one can look to well-publicized difficulties with the recent massive tunnel project in Boston, the unique engineering demands associated with new high-rise buildings with powerful architectural statements in New York and Chicago, and the rapidly increasing demand for concrete in Asia caused by rapid economic growth in those countries. One dark cloud on the otherwise sunny horizon for concrete is the problem of CO_2 generation during the manufacture of cement. The carbon footprint of concrete can be lowered significantly by incorporating industrial byproduct materials such and slag and fly ash into concrete. Under some conditions this can be beneficial but it also can cause durability problems. These materials are known to change the structure, and therefore the properties, of C-S-H. Here again, building on these recent results, SANS and other neutron methods can be used to measure the structure and provide a basis for a new generation of models.

References

[1] A. J. Allen, J. J. Thomas, and H. M. Jennings, Nature Materials **6**, 311 (2007).

[2] A. J. Allen, J. Appl. Cryst. **24**, 624 (1991).

[3] J. J. Thomas, H. M. Jennings, A. J. Allen, Cem. Concr. Res. **28**, 897 (1998).

[4] H. M. Jennings, J. J. Thomas, J. S. Gevrenov, G. Constantinides, F.-J. Ulm, Cem. Concr. Res. **37**, 329 (2007).

[5] J. J. Thomas, D. A. Neumann, S. A. FitzGerald, R. A. Livingston, J. Am. Ceram. Soc. **84**, 1811 (2001).

Biaxial Fatigue Failure in Gas Pipelines

T. Gnäupel-Herold[1,2]; D. Liu[1], H. Prask[1,2]

Fatigue has not traditionally been a primary concern in the design of oil or gas pipelines. However, investigations of recent oil pipeline ruptures [1, 2] have shown that fatigue was either the primary or a contributing cause, resulting in spills > 10^3 m^3 of crude oil. The huge costs associated with loss and cleanup warrant a more detailed investigation of material properties and behavior contributing to this type of failure.

For oil pipelines, vibrations and pressure changes are among the sources of stress cycling which lead to the high-cycle type of fatigue at moderate stress amplitudes. Other external influences that induce fatigue include bending/unbending during transportation of the pipe sections—identified as the primary cause for the fatigue rupture of the Enfield Pipeline [1], wave-action on offshore pipelines, and daily or seasonally changing soil conditions affecting ground-laid pipelines. The results are high axial stress amplitudes at relatively few accumulated cycles.

In pressurized gas pipelines the stresses are always biaxial with a ratio of hoop to axial stress of 2:1. External forces on floating structures or from shifting soil will primarily affect the axial stresses while hoop stresses remain static at a level determined by the gas pressure. Typical operating pressures result in hoop stresses of ≈ 70 % of the minimum specified yield strength (YS), which implies axial stresses of 0.35 × YS. Thus, infrequent but potentially high amplitude external stresses add to the already high operating stresses. Such external stresses are most damaging on pre-existing flaws or heterogeneities having detrimental properties, such as residual stress fields at or above the yield strength level.

Residual stress fields of this magnitude occur around girth welds [3] which are laid in the field during pipeline installation. This complex "stress environment" exists in the pipe steel microstructure which is anisotropic (in the axial, hoop and radial directions) and inhomogeneous (weld vs. base metal, base metal through thickness), due to the various stages of rolling, sizing and bending during pipe manufacture. Neutron diffraction appears uniquely suited to elucidate this complexity at all points in the pipeline life-cycle, i.e., after welding, to applied biaxial stress, to fatigue, and to failure, as well as being able to differentiate inside/outside and weld/base materials.

The specimens used, provided by Dr. Michael Law of the Australian Nuclear Science and Technology Organization,

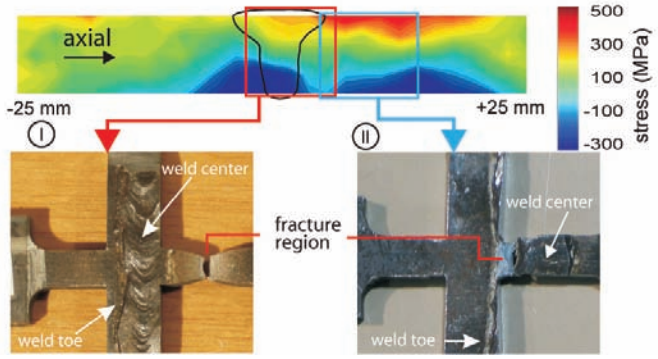

FIGURE 1: Residual stress field around the girth weld in an intact pipe section. The red and blue boxes indicate the gage sections of the cruciform specimens (I) and (II).

were cut from X70 grade steel pipe with a specified minimum yield strength of 483 MPa and an actual yield strength of between 543 MPa and 575 MPa. The pipe section used for electro-discharge-machine cutting cruciform and tensile specimens was 274 mm in diameter and 120 mm long. The cruciform gage sections were located such that they contained two parts: a portion of the weld containing the root and the heat-affected zone, and a region of high magnitude residual stress that was located approximately 8 mm to 12 mm away from the weld center line towards the axial direction. The cruciform specimens were both loaded statically with 340 MPa in the hoop direction, which loading was kept constant throughout the experiment. The axial load was increased until yielding was found using the d-spacings as a measure, then dropped to 240 MPa and then increased again which completed one cycle.

Specimen (I) failed in the first cycle at a load of 550 MPa, well outside the biaxial gage section. The circumstances of the failure (plastic collapse) and its location at the high magnitude stress field approximately 10 mm from the weld (see Fig. 1) prompted a second test with the gage section to include the location of the fracture of the first specimen. Specimen (II) had a reduced gage cross section to ensure the concentration of applied stresses within the gage section. It accumulated fewer than 50 cycles before failing by brittle fracture near the edge of the gage section in the heat-affected zone. Figure 2 shows the lattice-spacings in the center of the gage section near the outer and the inner pipe surfaces vs. applied axial stress for specimen (II). At the beginning of the loading the *d*-spacings are well distinguished and they

[1]NIST Center for Neutron Research, National Institute of Standards and Technology, Gaithersburg, MD 20899
[2]University of Maryland, College Park, MD 20742

maintain that difference up to the minimum specified yield strength. Higher stresses cause the *d*-spacings near the outside to saturate while the *d*-spacings near the inner surface continue to rise in proportion to the applied stress. This is a clear indication of an earlier onset of yielding near the outer surface, which was also the region of high tensile residual stress in the intact pipe (Fig. 1). The yield stress near the outside of the pipe is estimated to be approximately 50 MPa smaller than near the inside.

The comparison of measurements on this biaxially loaded sample with a uniaxially loaded (in the axial direction) tensile specimen reveals the difference between the strength of the weld and the base materials. The uniaxial specimen measurement is shown in Fig. 3. Due to the proximity to the fracture site with its stress concentration in the necking

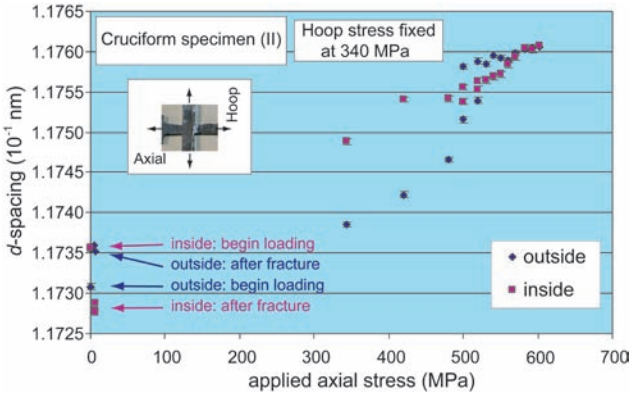

FIGURE 2: Lattice spacings from the gage section of the cruciform specimen (II). The inset cartoon shows biaxial tensile stressing of a cruciform sample.

region, the lattice spacings in the weld continue to climb because the local stress (> 600 MPa at peak) field is higher than in the base material. Note that the largest *d*-spacings actually occur below the yield region, which is caused by the experimental regimen of increasing strain rather than stress. Thus, after the onset of necking, strain is still accumulated while the applied stress drops. Similar to the cruciform specimen but at noticeably lower stress levels, the lattice spacings in the base material saturate (i.e., no longer increase with stress) first near the outside, while the *d*-spacings near the inside continue to climb. This confirms different yield stresses of the inside/outside locations.

The results presented here reveal that X70 pipe steel performs well up to the actual yield strength but, as expected, accumulates a very limited number of cycles at this stress level. More investigations are needed for cycling at lower stress amplitudes and especially for axial tension/compression cycles. The yield stress under biaxial loading appears to be higher than under uniaxial loading. However,

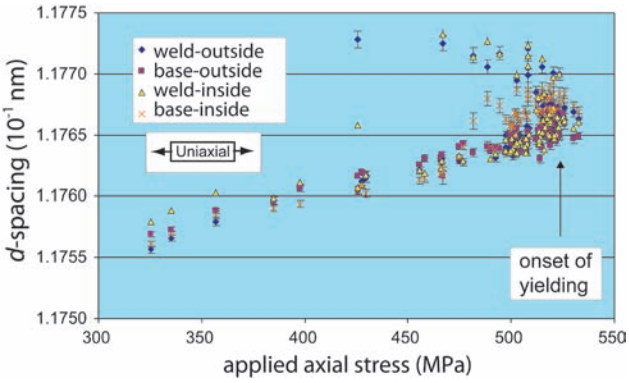

FIGURE 3: Lattice spacing for an axially loaded tensile specimen, measured at four locations near the inside/outside of the weld and the base. Base inside/outside positions correspond to inside/outside mentioned in Fig. 2. The inset cartoon shows uniaxial stressing of a tensile specimen.

a more detailed investigation of the transfer of applied biaxial load into the gage section needs to be conducted. Different yielding behavior is indicated in the base material near the inner and outer pipe surface, which is at least a contributing cause for the failure of cruciform specimen (I). This finding provides evidence that through-thickness anisotropy may have to be included in material models for pipeline simulation. The current practice of using through-thickness average YS results in a slightly overestimated YS for the region near the outside of the pipe. While these variations in strength occur well above the minimum specified YS they may affect the definition of the pipe safety margins.

References

[1] National Transportation Safety Board, *Rupture of Enbridge Pipeline and Release of Crude Oil near Cohasset, Minnesota July 4, 2002,* Pipeline Accident Report NTSB/PAR-04/01, PB2004-916501, Adopted June 23, 2004, Washington, D.C.

[2] Alberta Energy and Utilities Board, *Investigation Report: Rainbow Pipe Line Company Ltd. Crude Oil Pipeline Failure, October 10, 2006,* www.eub.ca , May 9th 2007.

[3] M. Law, H. J. Prask, V. Luzin, T. Gnaeupel-Herold, Materials Science and Engineering A **437**, 60 (2006).

Lateral Roughness Measurements of Buried Interfaces in Extreme Ultraviolet Lithography Photoresists

K. A. Lavery; V. M. Prabhu; E. K. Lin; W.-L. Wu[1]; K. W. Choi[2]; M. Wormington[3]; S. K. Satija[4]

Continual advances in the semiconductor industry have been driven by the consistent decrease in the lithographic feature size. As the critical size scale decreases to the sub-32 nm regime, the presence of roughness along the feature edge will be a major detriment to quality, reliability, and the potential for high device performance.

The origins of line edge roughness are not fully understood, but are rooted in the interdependent exposure, reaction, and development steps of the photolithographic process. In particular, the reaction step, in which activated photoacid molecules catalyze reactions in the exposed regions of the photoresist, has been linked to roughness formation through diffusion of acid molecules into unexposed areas. Here we present the first direct measurement of the complete photoacid reaction-diffusion front profile in a photoresist film, combining diffusion length measurements with examination of the lateral inhomogeneity of the diffusion front. This measurement was accomplished using specular and off-specular neutron reflectometry on the Advanced Neutron Diffractometer/Reflectometer (AND/R) beam line at the NCNR.

In this work, we used a representative extreme ultraviolet lithography (EUVL) photoresist copolymer, polyhydroxystyrene-*co*-poly(d_9-*tert*-butyl acrylate) (PHOST-*co*-d_9-TBA) where the hydrogens of the t-butyl protecting group are replaced with deuterium [1]. This substitution enhances the neutron contrast between the protected and deprotected regions of the resist, as the protecting group is volatile and leaves the film completely upon deprotection. The experimental geometry was a polymer-polymer bilayer [2] supported on a float glass substrate (Fig. 1A), where the bottom layer was a polymer containing 6 % by mass of the photoacid generator triphenylsulfonium perfluorobutane sulfonate (TPS-PFBS) and the top layer was the PHOST-*co*-d_9-TBA resist copolymer. This configuration mimics an ideal, perfectly sharp exposure line edge, with the bottom layer representing the exposed regions.

The reaction front was measured using specular neutron reflectometry (C). Specular neutron reflectometry was used to determine the extent of reaction and the diffusion front shape, allowing insight into the line broadening occurring during the lithographic process (Fig. 1B). The reflectometry data were converted into the extent of deprotection as a function of depth, as shown in Fig. 1C. While these measurements give the reaction-diffusion front depth profile with nanometer resolution, specular reflectometry gives no information on the lateral structure of the reaction front. For instance, one cannot differentiate a smooth, gradual decay in the deprotection profile from an undulating, inhomogeneous reaction front. The ability to discern between these two scenarios is of critical importance to determining whether the reaction process is responsible for roughness formation in lithographic features.

Off-specular neutron reflectometry was used to measure the buried in-plane structure of the reaction front [3]. Measurements were performed at multiple angles, thus giving sensitivity to lateral length scales ranging from 90 nm up to several microns. Off-specular reflectometry offers the additional advantage of being able to discriminate between interfacial roughness and material gradients [4]; something

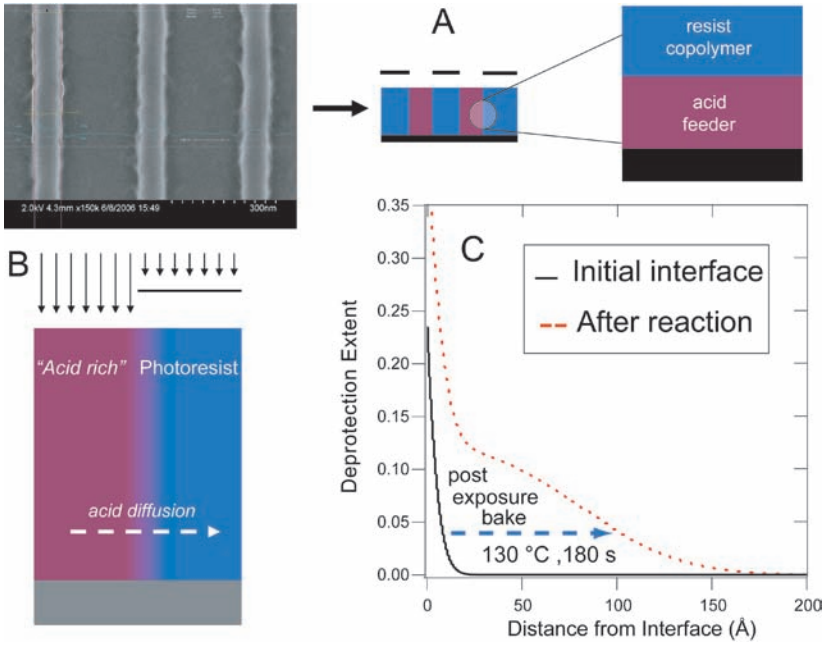

FIGURE 1: A polymer-polymer bilayer is used to model the line edge between the exposed and unexposed regions of a photoresist film (A). This geometry is used to follow the acid reaction-diffusion front in a model resist system, mimicking the diffusion at an exposure line edge (B).

[1]Polymers Division, National Institute of Standards and Technology, Gaithersburg, MD 20899
[2]Intel Corporation, Santa Clara, CA 95054
[3]Bede Scientific Inc., Englewood, CO 80112
[4]NIST Center for Neutron Research, National Institute of Standards and Technology, Gaithersburg, MD 20899

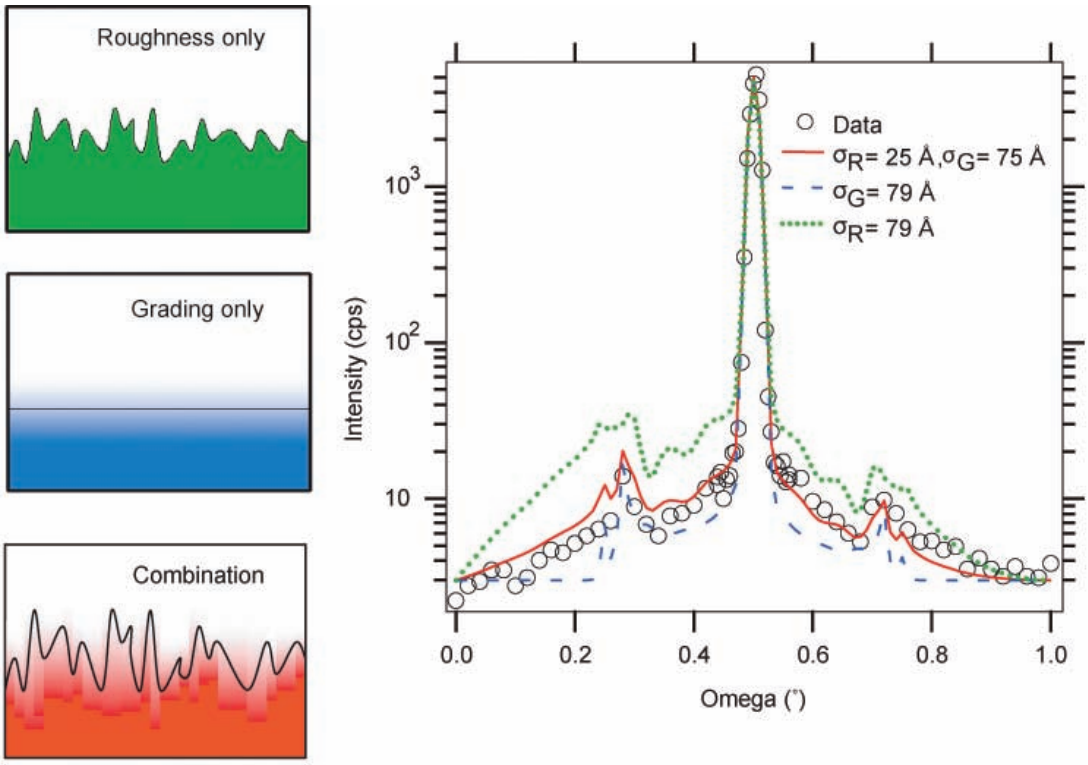

FIGURE 2: Off-specular reflectivity allows the differentiation between different types of "rough" interfaces. Using a highly rough interface to describe the reaction front over-estimates the off-specular intensity (green), while a chemical gradient (blue) under-estimates the intensity. A chemical gradient with undulations at the wave front provides the best description of the data (red).

that specular measurements are unable to provide. Figure 2 shows an off-specular curve taken at a Q_z value of 0.022 Å^{-1} which illustrates the sensitivity of the scattering intensity to the lateral form of the reaction front. From specular measurements, the width of the reaction front is 79 Å. If we assume that this width is completely due to undulations with amplitude 79 Å, the calculations overestimate the diffuse scattering intensity (green curve). On the other hand, if we assume the reaction front is perfectly smooth and the reaction front width is due solely to a gradient in the extent of deprotection, the calculations underestimate the diffuse scattering (blue curve).

The best fit to the data was obtained when combining these effects. Assuming the gradient (σ_G) and roughness (σ_R) terms are not coupled, we can constrain the fit using the interfacial width obtained from specular measurements (σ_{spec}) such that $\sigma_{spec}^2 = \sigma_G^2 + \sigma_R^2$. Using this constraint, we find the first 75 Å of the reaction front shows a smooth decrease in the deprotection extent. Over the last 25 Å there are lateral inhomogeneities at the wave front, modeled as roughness at the interface. This structure is illustrated in the red curve in Fig. 2, which provides the best description of the off-specular data. In addition to separating the contributions of gradient and roughness, the characteristic lateral length scale of roughness was found to be on the order of 800 Å. The amplitude and lateral length scale of the roughness of the reaction front is very smooth with a very low frequency, characteristics that are acceptable for next-generation lithography. Any significant roughness formation is likely to arise from subsequent processing steps such as the swelling and deswelling that may occur during the development process. Extending neutron reflectivity to probe the solid / liquid interface during development represents the next major step in understanding the materials limits of chemically amplified photolithography.

References

[1] K. A. Lavery, B. D. Vogt, V. M. Prabhu, E. K. Lin, W. L. Wu, S. K. Satija, and K. W. Choi, Journal of Vacuum Science and Technology B **24**, 3044 (2006).

[2] E. K. Lin, C. L. Soles, D. L. Goldfarb, B. C. Trinque, S. D. Burns, R. L. Jones, J. L. Lenhart, M. Angelopoulos, C. G. Willson, S. K. Satija, and W. L. Wu, Science **297**, 372 (2002).

[3] S. K. Sinha, E. B. Sirota, S. Garoff, and H. B. Stanley, Physical Review B **38**, 2297 (1988).

[4] M. Wormington, I. Pape, T. P. A. Hase, B. K. Tanner, and D. K. Bowen, Philosophical Magazine Letters **74**, 211 (1996).

Nanostructured Liquids From Disordered Surfactant Melts Blended With Functional Homopolymers

V. R. Tirumala[1,2]; E. K. Lin[2]; J. J. Watkins[1]

Block copolymers are immiscible macromolecules joined together by covalent bonding which form microscopically segregated phases. These phases readily form periodic morphologies that can be controlled by tailoring the molecular parameters [1]. Recent advances have shown that amphiphilic (i.e., having water-soluble and water-insoluble ends) block copolymers can be used in the templated fabrication of nanostructured inorganic materials that find a variety of applications in electronic, magnetic, and photonic devices. However, microphase segregated amphiphilic block copolymers are currently unavailable in bulk quantity, limiting their utility in the fabrication of nanostructured inorganic materials at a commercial scale. On the other hand, low molar mass amphiphilic surfactants based on poly (oxyethylene-oxypropylene-oxyethylene) (PEO-PPO-PEO; Pluronics or Poloxamers) are widely available, inexpensive and are used in many detergent, cosmetic, pharmaceutical, and biomedical applications. While the systems may be well suited for the fabrication of nanostructured materials, their melts are highly disordered and do not form periodic morphologies due to their low segregation strength.

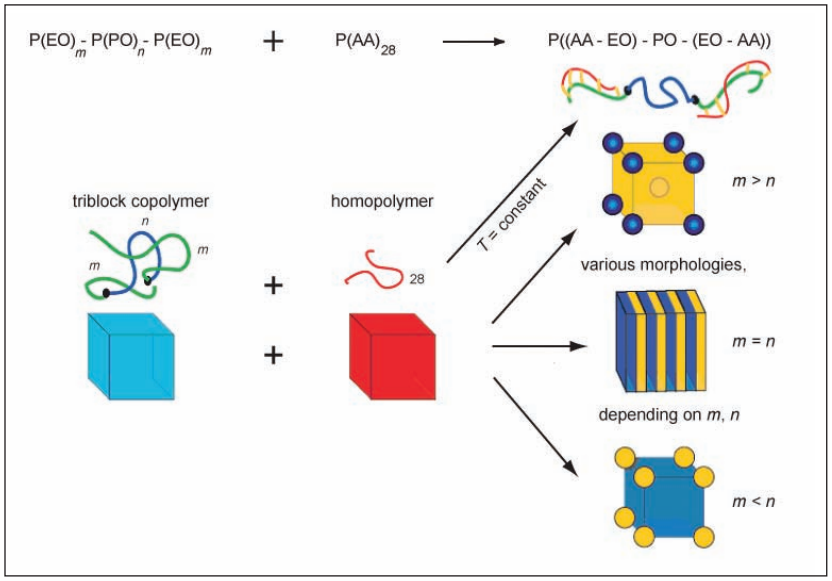

FIGURE 1: Schematic representing the generation of ordered microphases with the addition of a homopolymer to phase-mixed triblock copolymer melts. The phase-mixed copolymer is represented by the mixture of colors, *blue and green*, and the chemically homopolymer is represented by the color *red*. The phase-separated structures in the blend are thus represented by blue and yellow (i.e., mixture of red and green). In the figure *m* and *n* represent the number of EO and PO blocks, respectively.

The strength of phase segregation is determined by the product of the Flory-Huggins interaction parameter (χ) between the two constituents and the total molecular weight or chain length (N) of the block copolymer. Therefore, microphase segregated block copolymers typically have either large χ, which is a measure of repulsion between the segments, or a large molar mass. Commercially available Pluronic copolymers have a low molecular weight and a low interaction parameter, the product of which dictates them to be phase-mixed and highly disordered. Here, we show from small-angle neutron scattering measurements that the disordered Pluronic copolymer melts form ordered morphologies when blended with a widely available homopolymer such as poly (acrylic acid) (PAA) or poly (4-vinyl phenol). In other words, Pluronic copolymer melts undergo a disorder-to-order transition with the addition of a homopolymer that can selectively associate with the polyoxyethylene segments through hydrogen bonding. The results suggest a low cost, high volume approach to the generation of ordered polymeric liquids for commercial use [2]. The measurements were performed using the SANS diffractometers at NG-3 and NG-7 at the NCNR.

We first focus on Pluronic copolymers blended with PAA. Although PAA is known to associate with homopolymer PEO through hydrogen bonding, its selectivity between PEO and PPO is unknown. Differential scanning calorimetry and infrared spectroscopy measurements on mixtures of low molar mass homopolymers have shown that PAA interacts with the ether oxygen in both PEO and PPO. Therefore, we determined the selective miscibility of PAA from neutron scattering measurements by employing a deuterium labeled Pluronic-like copolymer (dF68; PEO-d_6PPO-PEO). Figure 2 shows the change in absolute neutron scattering intensity, full-width at half-maximum, and the position of the primary neutron scattering peak from deuterated Pluronic-like copolymer blended with hydrogenous PAA, collected as a function of homopolymer concentration at 80 °C. The neat copolymer comprises PEO at 80 % mass fraction which pertains to body-centered cubic morphology when microphase segregated. Above the melting point of PEO,

[1]University of Massachusetts, Amherst, MA 01003
[2]Polymers Division, National Institute of Standards and Technology, Gaithersburg, MD 20899

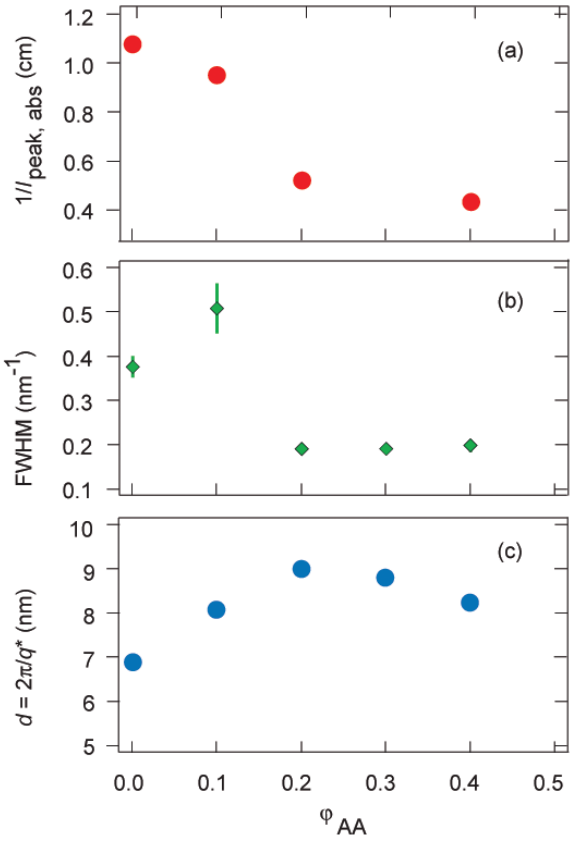

FIGURE 2: Change in (a) absolute intensity, (b) full-width at half-maximum, and (c) interdomain spacing calculated from the primary neutron scattering peak in deuterated Pluronic-like copolymer (*d*F68) thin film as a function of PAA concentration, φ_{AA}, at 80 °C. Concentration fluctuations in the disordered *d*F68 melt at 80 °C become strongly correlated with the addition of PAA between 10 % and 20 % mass fractions. The *d*F68 copolymer corresponds to the case, $m > n$, described in Fig. 1.

however, the broad scattering peak from the neat *d*F68 copolymer represents weakly correlated concentration fluctuations from a disordered liquid. The correlation between deuterated PPO domains improves significantly with the addition of PAA resulting finally in a relatively sharp peak at 40 % homopolymer mass fraction. The increase in scattering intensity from PAA/*d*F68 blends also suggests that the homopolymer is selectively miscible with PEO segments.

The selective PAA/PEO- association may increase the *effective* PEO-PPO segregation strength in Pluronic copolymers. An increase in segregation strength should directly correspond to an increase in the order-disorder transition temperature. Figure 3 shows the change in SANS spectra from PAA/*d*F68 blends at 0 % and 40 % homopolymer mass fractions, measured over the temperature range 80 °C to 175 °C. While the neat copolymer clearly gets more disordered with an increase in temperature, its blend with PAA remains highly ordered without a change in morphology until 175 °C.

The effective χN in PAA/*d*F68 copolymer blends is much higher than that in the neat copolymer due probably to the selective hydrogen bonding between PAA and EO segments. The selective AA/EO hydrogen bonding could increase the repulsion between EO-PO thus improving the effective segregation strength of the copolymer. This approach can be further generalized to any homopolymer with strong intermolecular association such as poly (4-vinylphenol), poly (styrenesulfonic acid), etc. The difference in selectivity affinity (for EO) and the strength of hydrogen bonding of the homopolymer can be used as additional variables to tune the melt phase morphology of Pluronic and Pluronic-like unsegregated and weakly segregated amphiphilic block copolymers. When applied to commercially available amphiphilic surfactants of low molecular weight and low segregation strength such as Pluronic copolymers, this simple and inexpensive approach can generate well-ordered polymeric liquids of cubic, cylindrical, and lamellar morphologies in commercially relevant quantities. Such systems find many applications in the industrial fabrication of nanostructured inorganic materials with improved functionalities. For example, mesoporous silica films synthesized from PAA/Pluronic F127 blends exhibit exceptional order compared to those prepared from the neat Pluronic F127 template [3].

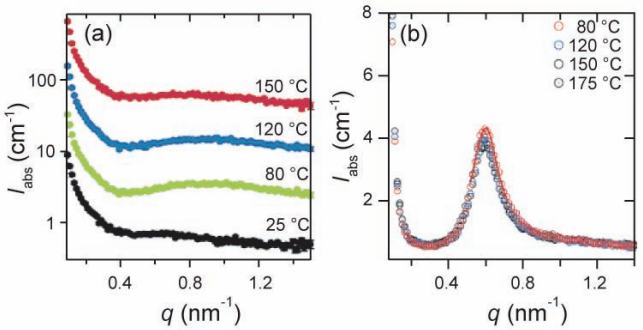

FIGURE 3: SANS profiles from (a) neat *d*F68 copolymer and (b) its PAA blend thin film at 40 % mass fraction as a function of temperature. The neat copolymer is highly disordered in the range 25 °C to 150 °C, whereas the temperature stability peak near $q = 0.6$ nm^{-1} shows that the blend remains highly ordered even up to 175 °C. Data in (a) are in absolute units at 25 °C but are offset in intensity by factors (100, 200, and 300) cm^{-1} at higher temperatures.

References

[1] F. S. Bates and G. H. Fredrickson, Physics Today, **52**, 32 (1999).
[2] V. R. Tirumala, A. H. Romang, S. Agarwal, E. K. Lin, and J. J. Watkins, Adv. Mater., submitted.
[3] V. R. Tirumala, R. A. Pai, S. Agarwal, J. J. Testa, G. Bhatnagar, A. H. Romang, C. Chandler, B. P. Gorman, R. L. Jones, E. K. Lin, and J. J. Watkins, Chem. Mater., in press.

A Class of Micellar Solutions with Viscosity Tunable by Light

Aimee M. Ketner and Srinivasa R. Raghavan[1]

Imagine a fluid that can be switched from a thick gel to a flowing liquid upon application of an external field. Such tunable fluids do exist: indeed, switching viscosity by application of an electric or a magnetic field has been known for more than 50 years [1]. A third class of switchable fluids using light as the external field has also been envisioned [1-4]; however, such light-tunable or "photorheological" (PR) fluids have remained of academic interest only—the limiting factor has been the need for complex photosensitive molecules that require tedious synthesis [3,4]. Here, we highlight our recent work [1] on developing a simple class of PR fluids based on inexpensive chemicals that are readily available from commercial manufacturers. These PR fluids can thus be easily replicated in any industrial or academic laboratory, and we hope this will spur on eventual applications for such fluids, possibly to construct microvalves, dampers or sensors.

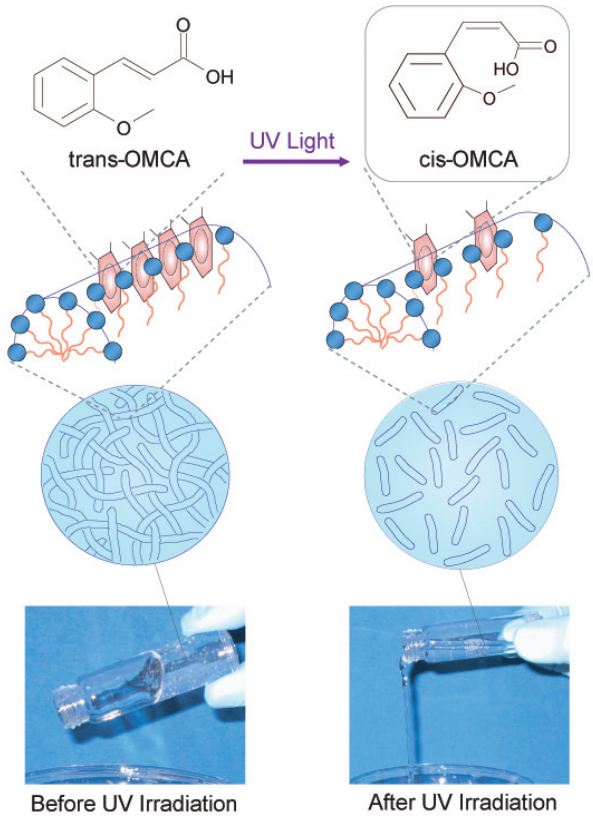

FIGURE 1: UV-induced changes in CTAB/OMCA fluids at the molecular, microstructural and macroscopic levels.

The scientific basis behind our PR fluids is depicted in Fig. 1, with the essential principle being the propensity of amphiphilic molecules (containing both hydrophilic and hydrophobic ends) to self-assemble in water to form nanoscale assemblies. Importantly, the size and shape of these assemblies depends on the geometry of the amphiphiles. The assemblies that we are primarily concerned with are called "wormlike micelles": these are long, flexible cylindrical chains with diameters around 5 nm and lengths that can extend up to a few microns. It is known that wormlike micelles can be formed in water by combining the well-known cationic surfactant, cetyl trimethyl-ammonium bromide (CTAB) with a range of organic additives. To make our system light-sensitive, we use a cinnamic acid derivative as our additive. This molecule, ortho-methoxy cinnamic acid (OMCA), is typically found with its C-C double bond in a *trans* configuration, as shown in the top portion of Fig. 1.

However, when OMCA is irradiated with UV light, the molecule photoisomerizes from *trans* to a *cis* configuration: as shown in Fig. 1, the *cis* isomer has a bend or kink at the double bond, giving the molecule a different geometry. The effect of this photoisomerization on the sample viscosity is illustrated visually in the bottom panel. Note that the original CTAB + *trans*-OMCA sample is highly viscous and almost gel-like in its appearance and it does not pour out of the tilted vial. On the other hand, upon UV irradiation, the sample (which is now composed of CTAB + *cis*-OMCA) has a low viscosity, akin to water, allowing the sample to be poured easily out of its vial. This visual difference in flow properties can be quantified by rheological measurements: it corresponds to a decrease in the zero-shear viscosity (η_0) of the sample by a factor of about 10 000 [1].

Why does the photoisomerization of OMCA induce such a dramatic drop in viscosity? The likely mechanism for this effect is shown in Fig. 1, and it has two distinct aspects: one at the molecular, and the other at the microstructural level [1]. At the molecular level, we believe that the geometry of *trans*-OMCA allows the molecule to adsorb onto the cationic micelles. Such adsorption occurs due to a combination of hydrophobic and electrostatic interactions, with the aromatic ring partially submerged into the hydrophobic core of the micelle. As a result of this adsorption, the *trans*-OMCA counterions reduce the effective charge on the cationic headgroups of CTAB and the lower headgroup charge, in turn, allows the self-assembly of very

[1]University of Maryland, College Park, MD 20742

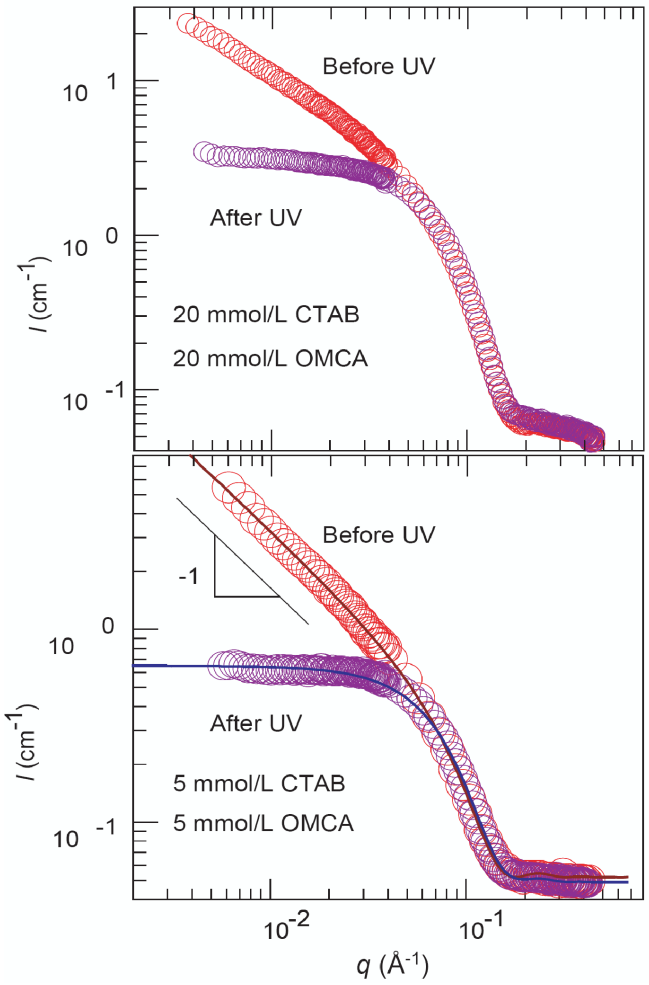

FIGURE 2: SANS spectra for two CTAB/OMCA samples before and after UV irradiation.

long wormlike micelles that entangle to produce a viscous fluid. However, when OMCA is isomerized, the *cis*-OMCA isomer has a much weaker tendency to adsorb onto the micelles because its hydrophobic and hydrophilic regions are not well separated. Thus *cis*-OMCA will tend to desorb from the micelles, increasing the effective charge on the surfactant headgroups. The increase in charge translates into an increase in headgroup area, and the resulting change in amphiphile geometry is reflected as a transition to much shorter micelles (short cylinders or ellipsoids or spheres). The shorter structures, in turn, impart a much lower viscosity to the sample.

The microstructural basis for our PR fluids is thus a light-induced transformation of long, wormlike micelles to much shorter micelles (Fig. 1). To verify such a change, we turned to small-angle neutron scattering (SANS) [1]. Samples for SANS were made in D_2O and measurements were conducted on the NG-7 beamline at the NCNR. SANS spectra for intensity I vs wave-vector q are shown in Fig. 2 for two samples with CTAB/OMCA concentrations of 20/20, and 5/5 mmol/L, respectively. (We studied samples at low concentrations to minimize intermicellar interactions). For both samples, UV irradiation causes a significant drop in the intensity at low q, which is a direct, qualitative indication of a decrease in micelle size. To be more quantitative, we modeled the SANS data from the 5/5 sample. Here, the intensity asymptotes at low q to a slope of about –1 prior to irradiation, which is indicative of long, cylindrical structures. We therefore modeled the micelles as rigid cylinders, and the fit yielded a micellar radius of 22 Å and a length of ca. 3000 Å. The same sample after irradiation shows a plateau in SANS intensity at low q, which suggests the presence of smaller and more globular structures. Accordingly, we modeled the micelles in this case as ellipsoids of revolution, and the best fit was obtained for prolate ellipsoids with radii of 22 Å and 40 Å, respectively, for their major and minor axes. Thus, SANS confirmed that there is indeed a dramatic reduction in the largest dimension of the micelles (a factor of about 100) due to UV irradiation.

Finally, it is worth clarifying several aspects and limitations of the PR fluids highlighted here. As indicated by the arrow in Fig. 1, the light-induced transition in the CTAB/OMCA system is a one-way effect, i.e., it is *not* reversible. The reason for the irreversibility lies in the nature of the absorption spectra of the *trans* and *cis* isomers of OMCA. Nevertheless, we emphasize that the concept illustrated by Fig. 1 is general and should apply to other organic derivatives where photoisomerizations are actually reversible. Indeed, work is ongoing in our own laboratory to find such derivatives.
A second issue that arises with any type of PR fluid is one of *timescale*. In our experiments, we used a 200 W mercury arc lamp and our sample size was 5 mL. Under these conditions, samples typically required about 30 min of irradiation to achieve their full reduction in viscosity. The limitation is one of path length and sample volume, i.e., faster effects can be obtained with smaller samples.

In conclusion, we have demonstrated a UV-induced drop in viscosity by more than four orders of magnitude in CTAB/OMCA mixtures. Although this effect is not reversible, the notable point is that it has been achieved in a simple system that can be replicated in any laboratory by mixing two common chemicals. The microstructural basis for this effect, which has been verified by SANS, is that UV light induces a transition from long, wormlike micelles to much shorter micelles. In turn, the microstructural changes are predicated upon a *trans* to *cis* photoisomerization at the molecular level.

References

[1] A. M. Ketner, R. Kumar, T. S. Davies, P. W. Elder, S. R. Raghavan, J. Am. **Chem. Soc. 129**, 1553 (2007).
[2] T. Wolff, G. von Bunau *et al.*, J. Phys. **Chem. 93**, 4894 (1989).
[3] H. Sakai *et al.*, J. Am. **Chem. Soc. 127**, 13454 (2005).
[4] G. Pouliquen, C. Tribet, Macromolecules **39**, 373 (2006).

Glass Transition Behavior of Thin Film Miscible Binary Polymer-Polymer Blends

P. F. Green[1]; B. M. Besancon[2]; C. L. Soles[3]

Nanotechnology is the discovery and application of novel, inherently size-dependent properties of materials confined to the nanometer scale. It is generally difficult to predict property deviations at this scale because they manifest the influence of two factors: confinement and interfacial interactions between the material (chemical) constituents and the external interfaces [1]. The length-scales over which the size-dependence is observed depend not only on the class of material, e.g., atomic or long-chain polymer, but also on the property observed.

One physical property of thin polymer films that is of practical interest is the glass transition temperature, T_g, below which a polymer becomes brittle. It is known that the average T_g of homopolymer films thinner than $h \approx 40$ nm may increase or decrease with decreasing h. This h-dependence appears to be associated with the relative monomer-substrate, monomer-monomer and monomer-free surface interactions. Most applications of polymers, however, involve mixtures of polymers. What, then, influences the T_g of a thin film homopolymer/homopolymer mixture?

Spectroscopic ellipsometery (SE) measurements of the average T_g of mixtures not only reveal thickness-dependent changes in T_g with decreasing film thickness but further indicate that the magnitudes of the changes are similar to those in pure polymers. A combination of SE and incoherent elastic neutron scattering (IENS) measurement [2] reveal the influence of locally heterogeneous dynamics on the average T_g of mixtures, leading to a completely new mechanism by which the glass transition can be understood in thin films.

We performed IENS studies on a completely miscible binary polymer-polymer blend of deuterated polystyrene (dPS) and tetramethyl bisphenol-A polycarbonate (TMPC), supported by SiO_x/Si substrates (oxidized silicon wafers). The thermodynamics of this system are well understood. The properties of particular interest with regard to understanding the T_g of thin films are: (1) the T_g of PS is 100 °C lower than that of TMPC; (2) the segmental dynamics of PS are fast compared to TMPC at any given temperature; (3) PS enriches the free surface (lower surface energy) whereas TMPC preferentially enriches the oxide layer of the substrate; (4) T_g decreases with decreasing h in the PS/SiO_x/Si system, whereas the opposite is true in the TMPC/SiO_x/Si system. It could be argued, therefore, that since the dynamics at the interfaces of these thin film samples are significantly different, the T_g-h dependencies should differ significantly from the pure homopolymer. However, SE measurements show remarkably similar h-dependent behavior. At high TMPC concentrations, greater than a mass fraction of 90 %, T_g increases with decreasing film thickness, whereas for smaller TMPC mass fractions T_g decreases with decreasing h [2].

Our INS measurements reveal evidence of a separate glass transition of the TMPC component, distinct from the average T_g of the film measured by spectroscopic ellipsometry. The incoherent scattering intensity is heavily dominated by the hydrogenous moieties in the TMPC whereas deuterium labeling greatly reduces the incoherent scattering cross section of the PS. The elastic scattered intensity, $I(Q)$, is plotted in Fig. 1 as a function of temperature for three samples containing 50 % mass fraction of TMPC. At temperatures $T < 200$ K, the intensity of the elastic peak is well approximated by the expression $I_{elastic}(Q) \propto \exp(-Q^2\langle u^2\rangle/3)$. In this expression, Q is the scattering vector, and $\langle u^2\rangle$ is the mean square atomic displacement. The deviation from linearity of the data near $T \approx 200$ K for each curve in Fig. 1 is interpreted as a sub-T_g

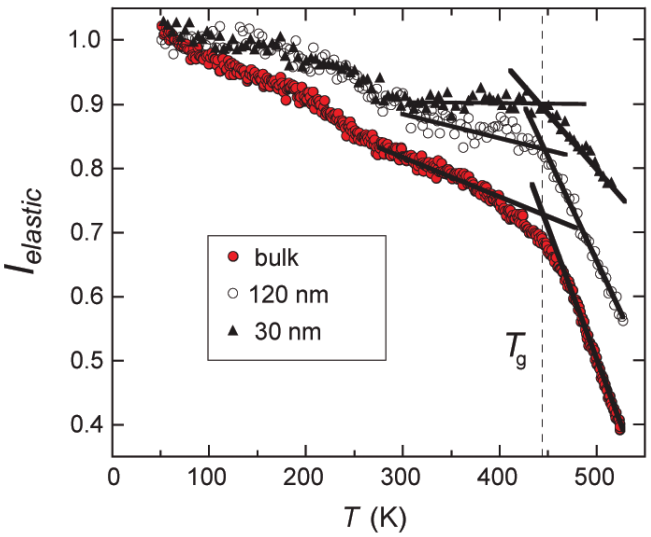

FIGURE 1: The neutron elastic scattering intensity vs temperature for the 50 % mass fraction TMPC/dPS samples is dominated by the (hydrogen-bearing) TMPC component. The TMPC effective glass transition temperature, identified with the crossing of the fitting lines, is $T_g \approx 445$ K (172 °C).

[1]University of Michigan at Ann Arbor, Ann Arbor, MI
[2]University of Texas at Austin, Austin, Texas 78712
[3]Polymers Division, National Institute of Standards and Technology, Gaithersburg, MD 20889

relaxation, primarily reflecting methyl group rotations. The glass transition temperature of the mixture, located where the fit lines cross, as shown in Fig. 1, occurs at $T_g \approx 445$ K (172 °C) for both bulk and thin film samples. The values of T_g determined using INS and ellipsometry (or differential scanning calorimetry (DSC) for the bulk samples [3]) are plotted as a function of composition for the 30 nm films in Fig. 2a and for the bulk samples in Fig. 2b. The values of T_g determined using these techniques are different: SE and DSC measure essentially the same average values of T_g, whereas the T_g of the TMPC component is found to be systematically higher in the INS measurements.

The different T_g values measured by the INS and SE techniques in these miscible blends might be rationalized as follows. Studies of binary miscible polymer-polymer blends that show a single average T_g can nonetheless show, at a local level, evidence of the distinctly different T_gs and relaxation times associated with each component in the blend; i.e., locally the dynamics can still be heterogeneous. The underlying reason for this dynamic heterogeneity is discussed in terms of the chain connectivity, which necessitates that a monomer on the A-chain (B-chain) will have an intrinsically higher than average concentration of A-monomers (B-monomers), locally as its nearest neighbors. This is often referred to as a self-concentration, φ_s. The effective local concentration, φ_{eff}, based on the Lodge-McLeish model [4], is determined by φ_s such that $\varphi_{eff} = \varphi_s + (1- \varphi_s)\varphi$, where φ is the bulk concentration. The model assumes that the length scale of the local region of enriched concentration around a given monomer is of order nanometers and is independent of temperature. In light of this, the component A of the mixture can sense a different effective T_g determined by φ_{eff}, than the average. It is probable that this notion is relevant here given that the INS measurements are predominantly sensitive to the methyl rotors on the TMPC, i.e., to the dynamics on the time scale of a single monomer. This is in contrast to SE (film) and DSC (bulk) measurements, which are sensitive to the average T_g. The T_g concentration dependencies of the different samples shown in Fig. 2 were fitted by a virial equation from which the self concentrations φ_s were determined [2]. The values of φ_s extracted from the fits to data using all three techniques are comparable.

The implication here is that in thin films the self-concentration concept appears to account for the systematically higher values of T_g determined by INS compared with those from SE. The fact that the TMPC concentration is enriched at the wafer interface, which would also lead to a local increase in the T_g near the interface, does not seem to be dominant, since this kind of interfacial segregation cannot occur in the bulk samples where INS values are also found to be systematically higher. Nevertheless, the T_g in these thin film polymer blends will depend in a complicated manner on the relative monomer-substrate, monomer-monomer and monomer-free surface

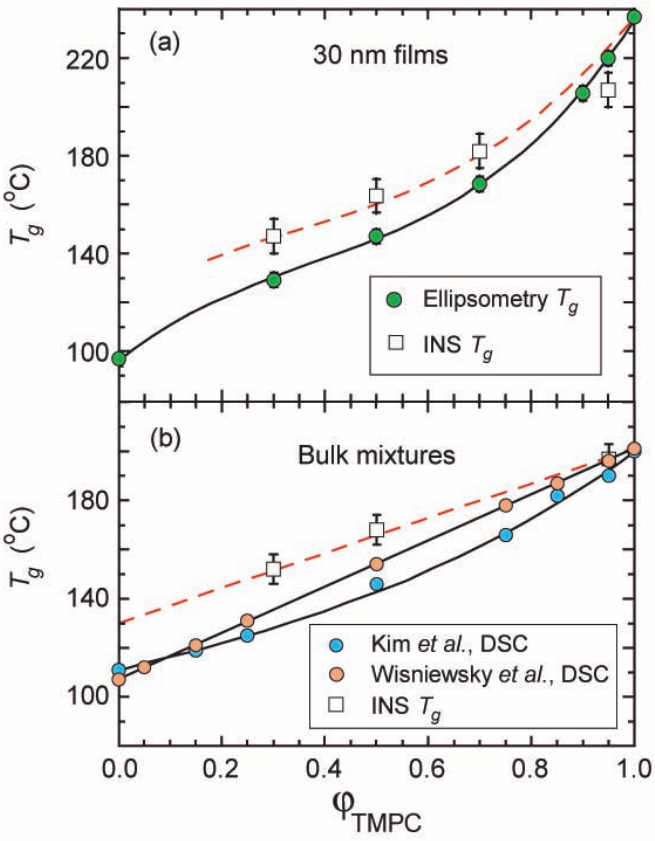

FIGURE 2: TMPC effective component T_g values measured using INS (white symbols) vs TMPC concentration. For 30 nm films the average glass transition temperatures from ellipsometry (solid line and colored symbols) are plotted in (a) and for bulk samples by DSC (solid line and colored symbols) in (b). The fit from the Lodge-McLeish model is shown as red dashed lines in (a) and (b) whereas the solid lines guide the eye.

interactions that determine the average T_g of homopolymer films. The thickness-dependent average values of T_g of polymer thin films reflect deeper underlying physics than was originally thought to be important. We are continuing these measurements using dielectric spectroscopy to examine further details of the component dynamics.

References

[1] K. Binder *et al.*, Prog. Polym. Sci. **28**, 115 (2002); M. Alcoutlabi, and G. B. McKenna, J. Phys. Condens. Matter **17**, R461 (2005); D. Long, and F. Lequeux, Eur. Phys. J. E 4, **371** (2001).

[2] B. M. Besancon, C. S. Soles, P. F. Green, Phys. Rev. Lett. **97**, 057809 (2006).

[3] E. Kim *et al.*, Macromolecules **28**, 1979 (1995); C. Wisniewsky *et al.*, Eur. Polym. J. **20**, 691 (1984).

[4] T. P. Lodge, and T. C. B. McLeish, Macromolecules **33**, 5278 (2000).

Alzheimer's Disease: Effects of β-Amyloid Oligomers on Cell Membranes

F. Heinrich, M. Lösche[1]; G. Valincius, I. Ignatjev[2]; Y. Sokolov, J. E. Hall[3]

Alzheimer's disease (AD) is a debilitating neurodegeneration that affects millions of elderly patients, particularly in the aging populations of developing countries around the globe. The *amyloid*-β (Aβ) peptide, a cleavage product of the membrane protein *amyloid precursor protein* (APP), has long been implicated in causing AD. Enzymatic cleavage of APP liberates Aβ monomers into the intercellular space of the central nervous system (CNS) where the peptide may adopt a misfolded conformation that is amenable to aggregation. Eventually, large insoluble amyloid fibrils are formed which constitute the hallmark feature found between destroyed nerve cells in affected brains of diseased patients. Indirect evidence has recently accrued that toxicity in the pathogenesis of AD may primarily reside with a specific soluble oligomeric form of Aβ rather than monomers or mature fibrils [1, 2]. These findings are starting to impact the search for promising novel therapeutic approaches [3, 4]. It is therefore timely to concentrate on molecular biophysical studies of the properties of Aβ oligomer particles [5]. We initiated such studies aiming to reveal structure-function relations that govern the association of prefibrillar Aβ oligomers with membranes, thus beginning a new direction in the century-old research on the origin of Alzheimer's disease.

Cell membranes are a complex blend of a large number of distinct lipids that form a two-dimensional matrix into which membrane proteins are incorporated or with which they are peripherally associated. One critically important function of cell membranes in the CNS is to maintain a cation gradient, and thereby a resting potential, between a cell's interior and external space.

The Hall lab at the University of California at Irvine has monitored the conductivity of free-standing model membranes, so-called black lipid membranes composed of just a single lipid or binary lipid mixtures, in response to incubation with soluble prefibrillar Aβ oligomers. They found a reduction of the insulating properties of the membrane that depends on its composition [6, 7]. In contrast to the currently prevailing hypothesis which suggests that Aβ oligomers form distinct membrane channels that interfere with ionic dynamic balance, it was suggested that the oligomers locally reduce the barrier to ion flow but do not open water-filled channel structures. Subsequently, in studies which invoked surface-stabilized, "sparsely tethered" bilayer lipid membranes (stBLMs) [8], we determined the structural impact of Aβ oligomers on membranes using neutron reflectometry (NR) and correlated changes in function, as observed with electrochemical impedance spectroscopy (EIS), with these structural effects. This work sets the scene for a broader research program on the molecular-scale aspects of AD.

NR measurements were performed on NCNR's AND/R spectrometer [9]. stBLMs composed of fully hydrogenated phospholipids showed reversible changes of the membrane upon incubation with soluble Aβ oligomers. Results were interpreted as a thinning of the hydrophobic bilayer core

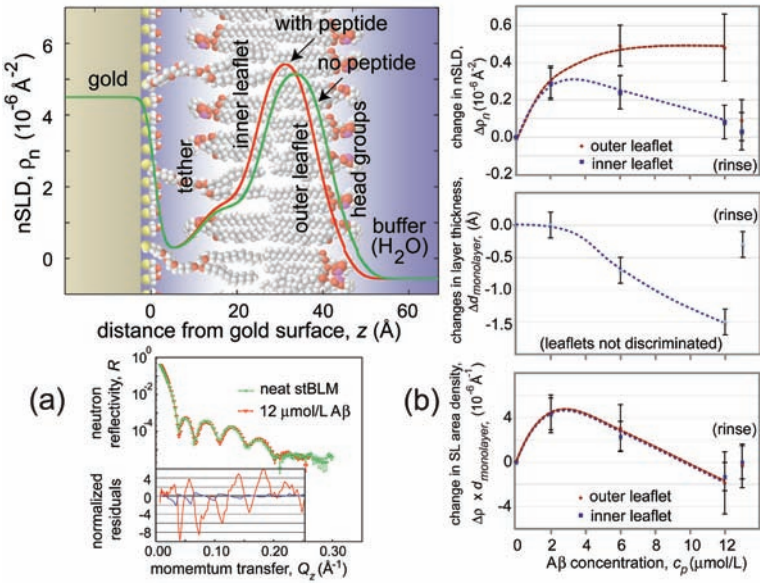

FIGURE 1: (a) NR and model reflectivities (lines) of an as-prepared stBLM and the same bilayer under the influence of Aβ oligomers. The lower inset shows residuals of the same data normalized to the NR of the neat bilayer, as well as the normalized residuals of a data set (not shown) of the bilayer after rinsing with protein-free buffer. The upper panel shows the nSLD models corresponding to the NR in the lower panel. (b) Changes of selected parameters that describe the stBLM models in (a). Upper panel: Development of the nSLD in the two distinct bilayer leaflets. Middle panel: development of the thickness of the two leaflets (assumed to be equal). Lower panel: Development of the neutron scattering length per unit area in the two distinct leaflets. The models rely on measurements of multiple solvent contrasts that are not all shown in panel (a). Similarly a number of results at various peptide concentrations are included in panel (b) for which the original data are omitted from panel (a) for clarity.

[1]NIST Center for Neutron Research, National Institute of Standards and Technology, Gaithersburg, MD 20899 and
Carnegie Mellon University, Pittsburgh, PA 15213

[2]Institute of Biochemistry, Vilnius, LT-08662, Lithuania
[3]University of California at Irvine, Irvine, CA 92717

which depends in its extent on the nature of the lipid and the peptide concentration. However, these NR results on the interaction of (hydrogenated) Aβ oligomers with fully hydrogenated stBLMs were limited in their predictive power since it was impossible to locate the peptide particles with respect to the membrane structure. NR experiments that employed chain-perdeuterated DMPC—a saturated phospholipid that is often used in model studies—were much more revealing in that respect.

Figure 1a shows NR results in H_2O-based buffer, as well as the respective model fits, for an as-prepared stBLM formed from chain-perdeuterated DMPC-d_{54}, and the same stBLM incubated with soluble Aβ oligomers at a peptide concentration, c_p = 12 μmol/L. Because the inner hydrophobic sheath of the bilayer contains a fully hydrogenated surface anchor [8] together with the deuterated lipid, both leaflets show different neutron scattering length densities (nSLD), ρ_n, and are distinguishable in the nSLD profile shown in the top left panel in Fig. 1. These profiles indicate that oligomer incubation increases the nSLD in the hydrophobic slab and shifts the peak closer toward the substrate surface. As shown in Fig. 1b, this experiment determines the structural impact of the Aβ oligomers on the membrane: The peptide interpenetrates the core of the membrane and affects both leaflets of the stBLM equally, as observed in the changes of the scattering length *area* density, $\Delta\rho_n \times d$, broken down into the values observed for the two bilayer leaflets (lower panel in Fig. 1b). The bilayer thickness, d, decreases upon increasing c_p while $\Delta\rho_n \times d$ goes through a maximum. This suggests that peptide may incorporate massively into the membrane, where it induces a compaction of the lipid chains, followed by a lateral relaxation of the membrane structure at high c_p, presumably through the reorganization of membrane material locally into the three-dimensional defects. It is estimated that at c_p > 10 μmol/L as much as 10 % volume fraction of the membrane may be composed of the peptide.

Complementing EIS investigations (see the Bode plot, inset in Fig. 2) confirm a dramatic decrease in membrane resistance to ion conduction at low frequencies of the driving voltage. While NR results which indicate that Aβ oligomers penetrate the entire membrane might be consistent with the assumption of channel formation, temperature-dependent EIS shows that the activation energy, E_a, for ion transport of across the membrane is much larger than expected for water-filled channels (lower panel of Fig. 2). This provides clear evidence that the Aβ-mediated conduction mechanism is distinct from membrane poration.

While providing the closest view to date on the molecular-scale aspects of the interaction of Aβ with membranes, these results are still preliminary in character. A more rigorous analysis and deeper understanding of the molecular-scale aspects of membrane-toxicity of Aβ oligomers will require more neutron scattering experiments with deuterated peptide, which has not yet been available to us. Furthermore, we aim at an in-depth comparison of the membrane effects

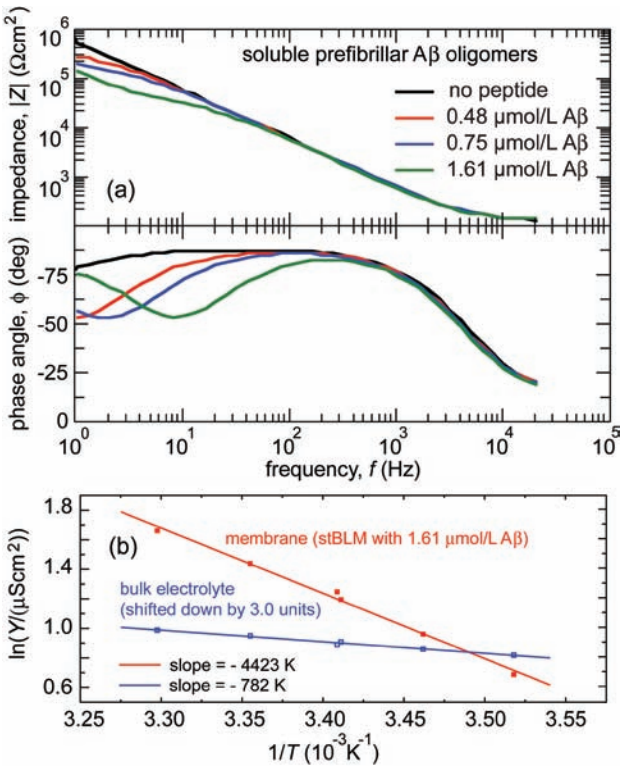

FIGURE 2: a) EIS Bode plots of a DOPC stBLM in 0.1 M NaCl, pH 7.3, as a function of Aβ concentration. b) Arrhenius plots of the conductivities of a membrane with Aβ (c_p = 1.61 μmol/L) and of the electrolyte, measured in the same experiment. Electrolyte conductivity has been divided by 1000. Activation energies derived from the slopes are E_a = 36.7 kJ/mol and 6.5 kJ/mol.

of other peptides (Aβ occurs in different lengths *in vivo*) and different aggregation states (peptide monomers, larger oligomeric association products, and fibrils). Deeper insight into the molecular aspects is also expected from coupling the results of scattering experiments with molecular dynamic computer simulations. These efforts, required to make serious progress toward an unraveling of the century-old puzzles posed by Alzheimer's disease, are currently underway.

References

[1] R. Kayed, E. Head, J. L. Thompson, T. M. McIntire, S. C. Milton, C. W. Cotman, C. G. Glabe, Science **300**, 486 (2003).
[2] D. M. Walsh, *et al.*, Nature **416**, 535 (2002).
[3] D. M. Walsh, *et al.*, Biochem. Soc. Trans. **33**, 1087 (2005).
[4] C. Glabe, Science **314**, 602 (2006).
[5] D. Eliezer, J. Gen. Physiol. **128**, 631 (2006).
[6] R. Kayed, Y. Sokolov, B. Edmonds, T. M. McIntire, S. C. Milton, J. E. Hall, C. G. Glabe, J. Biol. Chem. **279**, 46363 (2004).
[7] Y. Sokolov, J. A. Kozak, R. Kayed, A. Chanturija, C. Glabe, J. E. Hall, J. Gen. Physiol. **126**, 637 (2006).
[8] D. J. McGillivray, *et al.*, Biointerphases **2**, 21 (2007).
[9] J. A. Dura, *et al.*, Rev. Sci. Instrum. **77**, 074301 (2006).
[10] D. J. McGillivray, *et al.*, Proc. Natl. Acad. Sci. USA submitted (2007).

Protein Structure and Hydration Probed by SANS

C. B. Stanley, S. Krueger[1]; V. A. Parsegian, D. C. Rau[2]

Proper protein function relies on interactions that create correctly folded and assembled structures still maintaining the flexibility required for specific activity. Since these interactions are mediated by hydration, the energetics of protein function are necessarily coupled to water activity. Modulating biomolecular systems through the addition of solutes that vary in chemistry and size can provide a better understanding of the interactions including the role of water. Nature utilizes a variety of small solutes, called osmolytes, to protect proteins against thermal and chemical denaturation. Often osmolytes act indirectly through an exclusion from water hydrating biomolecular surfaces or from water sequestered in cavities. For similar reasons, stabilizing agents are added to protein solutions used in biotechnology and pharmaceutical applications. Here, we use small-angle neutron scattering (SANS) coupled with osmotic stress to investigate the hydration of guanylate kinase in the presence of solutes [1]. By taking advantage of the neutron contrast variation that occurs upon solute addition, the number of protein-associated (solute-excluded) water molecules can be estimated. These results provide a framework for studying similar biomolecular systems using neutron scattering.

An instructive way to view solute effects on biological systems is through the osmotic stress method [2]. This approach considers the various interactions from an added solute while also affording the measurement of forces between biopolymers and hydration changes accompanying biomolecular reactions. The solute size and chemical nature determines its exclusion from biomolecular surfaces, thereby acting osmotically on these regions and favoring more dehydrated states. Importantly, since osmotic stress mimics the influence of macromolecular crowding characteristic of the cell, its perturbing effects can teach us about molecular function in vivo.

Guanylate kinase (GK) is a 20.5 ku (20.5 kDa) protein that performs phosphoryl transfer from adenosine triphosphate (ATP) to guanosine monophosphate (GMP). We chose to study this protein because its structure contains a deep cavity for ligand binding, and it also undergoes large-scale conformational changes upon binding ligands. Conformational changes can be followed using SANS (Fig. 1) where Guinier fits indicate the protein radius of gyration, R_g, decreases from (17.2 ± 0.1) Å to (16.4 ± 0.1) Å upon binding GMP. The ATP-binding site also can be closed by addition of magnesium adenosine triphosphate (MgADP) resulting in R_g = (16.2 ± 0.1) Å. Calculated SANS profiles (Fig. 1, solid lines) made from the corresponding crystal structures using the Xtal2sas program [3] and references therein, demonstrate good agreement with the experimental data.

When solutes are introduced, any exclusion of solute away from the protein results in a preferential hydration. In the context of osmotic stress, these protein-associated water molecules that are thermodynamically important based on their exclusion from the bulk solute are what we term protein hydration. By considering the protein and protein-associated water as a composite particle, and accounting for the change in bulk solution scattering length density with solute volume fraction, Fig. 2 shows that solutes in the series: glycerol, triethylene glycol (TEG), and poly(ethylene glycol) (PEG) of molecular weight (MW) 400 and 1000 induce an additional scattering contribution above what is obtained from protein in H_2O/D_2O solvent alone. This excess contribution is attributed to protein-associated water [4]. Protein hydration can be expressed in terms of the number of water molecules associated with the protein, N_w (values given in Fig. 2). Glycerol is the least excluded solute, likely due to both its size

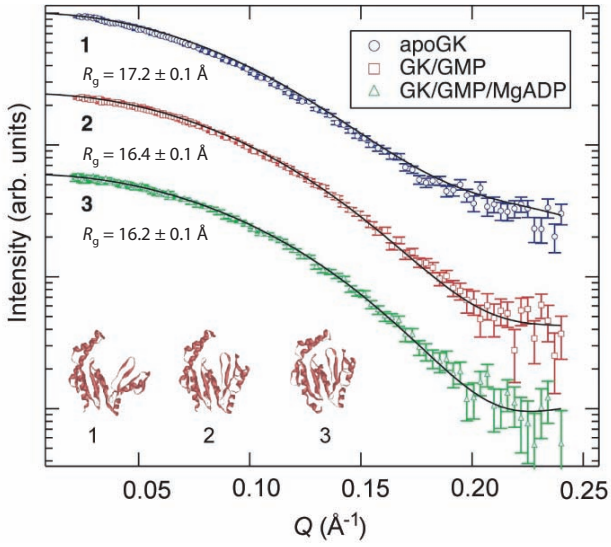

FIGURE 1: SANS of guanylate kinase (GK) conformations at 5 mg/mL in D_2O (data points) and SANS profiles calculated from the corresponding crystal structures using Xtal2sas (solid lines). Curves are shifted for clarity. Inset: Corresponding GK structures from x-ray crystallography: 1, GK (1EX6); 2, GK/GMP (1EX7); and 3, GK/GMP/MgADP (1LVG).

[1]NIST Center for Neutron Research, National Institute of Standards and Technology, Gaithersburg, MD 20899
[2]Laboratory of Physical and Structural Biology, National Institute of Child Health and Human Development, National Institutes of Health, Bethesda, MD 20892

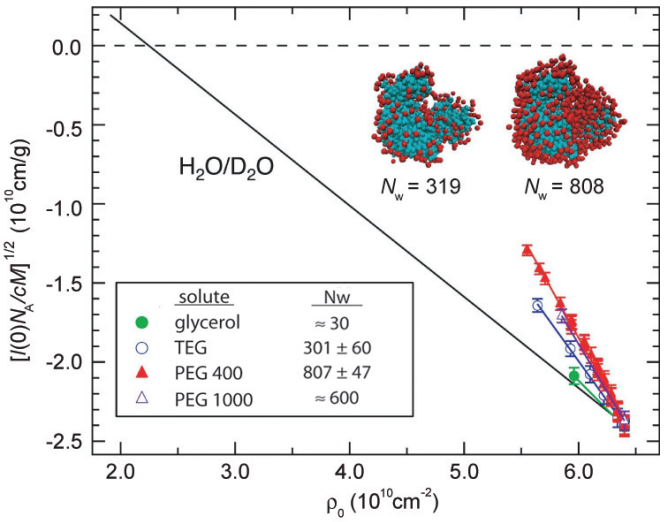

FIGURE 2: GK contrast variation by H_2O/D_2O (black line) and solute/D_2O. Plotted is the square root of the zero-angle neutron scattering intensity, $[I(0)N_A/cM]^{1/2}$, vs bulk solution scattering length density, ρ_0, where the observed excess contribution to the H_2O/D_2O contrast variation from added solute is related to the hydration of the protein, N_w, in the presence of that particular solute. Inset: Models of GK (cyan) with protein-associated water molecules (red) that closely correspond to N_w for the solutes TEG and PEG 400. Note that TEG is equivalent to PEG of MW 150.

and chemical nature. GK hydration then almost triples when going from TEG to PEG 400.

The corresponding changes in GK R_g are given in Fig. 3. No change in protein R_g is observed with added glycerol, consistent with the negligible N_w determined from $I(0)$. The solute size dependence observed with N_w in Fig. 2 is qualitatively mirrored in the effects on R_g. Isothermal titration calorimetry measurements of hydration changes accompanying ligand binding to GK display the same trend with solute size for these solutes and also indicate no protein conformational change occurs from solute alone over the range of solutes and concentrations applied in the SANS experiments. Based on the size-dependence of solute exclusion, the volume of protein-associated water, and similar SANS measurements we have made with lysozyme, it is determined that the majority of water associated with GK for these solutes likely resides in the cavity (see models in Fig. 2, inset). These results illustrate the potential use of SANS and osmotic stress for resolving structural details based on solute exclusion.

We have demonstrated methods of using SANS combined with osmotic stress to determine protein hydration in the presence of a series of solutes. The roles of solute size and chemistry, along with protein structure, in determining the extent of solute exclusion, and consequent protein hydration, have been investigated. Another opportunity for this research is to use deuterated solutes to unambiguously measure protein structure with solute addition. This can provide assurance that there are no structural changes for an added solute or be purposely used at high concentration to induce structural changes and measure the osmotic work. We hope this study forms the basis for such promising future research so that structural information about biological systems can be directly connected with their corresponding thermodynamics. SANS experiments were performed on the NG3 and NG7 30 m SANS instruments at the NIST Center for Neutron Research.

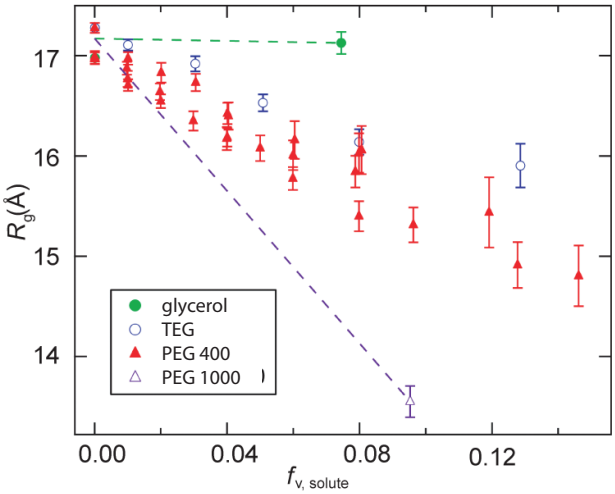

FIGURE 3: Measured change in GK R_g vs solute volume fraction, $f_{v,solute}$, determined by SANS. Dashed lines are given for glycerol and PEG 1000 to guide the eye.

References

[1] C. B. Stanley, S. Krueger, V. A. Parsegian, and D. C. Rau, Biophys. J. (submitted).

[2] V. A. Parsegian, R. P. Rand, and D. C. Rau, Proc. Natl. Acad. Sci. USA **97**, 3987 (2000).

[3] S. Krueger, I. Gorshkova, J. Brown, J. Hoskins, K. H. McKenney, and F. P. Schwarz, J. Biol. Chem. **273**, 20001 (1998).

[4] H. B. Stuhrmann, J. Haas, K. Ibel, M. H. Koch, and R. R. Crichton, J. Mol. Biol. **100**, 399 (1976).

Melting in Dehydrated Lipid Bilayers

M. Doxastakis[1], S. Ohtake[1]; V. García Sakai[2]; J. K. Maranas[3]; J. J. de Pablo[4]

Lipid bilayers are ordered structures that assemble in water as a result of the connection of hydrophilic head groups to hydrophobic tail regions. They form the biological membrane enclosing cells, as well as simplified enclosures, termed liposomes, used for drug delivery, gene therapy and immunization. Bilayers in biological functions and other applications are normally hydrated, and as a result the properties of hydrated bilayers are well studied and understood. This includes one of the most important physical properties of membranes: the melting transition that differentiates a solid-like state (gel phase) from the liquid state (liquid crystalline phase) [1]. The importance of this transition derives from the fact that cells and other enclosures leak their contents as it is crossed, which causes cell death or failure of liposomes as carriers. Although they have received less attention, dehydrated lipid bilayers are important both biologically, where certain organisms modify their cell membranes to survive desiccation [2], and in application as liposomes, where preparation of liposomal carriers requires drying and rehydration. In the former case, protection against dehydration is linked to changes in melting transition temperatures of hydrated and dehydrated membranes when additives are present. The work described in this highlight targets the melting transition in dehydrated lipid bilayers, filling the gap in our understanding of these systems.

Our approach uses a combination of quasi-elastic neutron scattering (QENS) experiments and molecular simulations to characterize mobility above and below the transition. We perform investigations on freeze-dried model liposomes, comprised of a single type of lipid molecule: dipalmitoyl-phosphatidylcholine (DPPC). These liposomes are a realistic representative of those used in applications, and they approximate biological cell membranes. We exploit the ability of neutrons to preferentially probe the motion of specific protons in the sample: by considering DPPC with deuterated head-groups (dhDPPC), we probe tail mobility; and by deuterating the tails (hdDPPC), we probe head-group mobility. In all of these dehydrated samples, the melting transition occurs near 370 K. As with any melting transition, the gel to liquid crystalline transition in a lipid bilayer involves a rapid rise in molecular mobility with temperature, easily observed using calorimetry. The analog to calorimetry in QENS is the fixed window scan, in which the elastic intensity, representing motion slower than the instrumental resolution, is monitored as a function of temperature. Fixed window scans on dhDPPC show that when dehydration is achieved via freeze-drying, the melting feature arises from the lipid tails. By comparison, scans on hdDPPC show a more gradual change [3].

We may regard mobility as rattling within a local cage superimposed with translation of the cage center of mass. Below the melting temperature, translation is minimal and it is possible to derive the local cage size from fixed window scans. The behavior of the local cage size with temperature is illustrated in Fig. 1. Below 220 K, only vibration occurs, as evidenced by the linear relation of mean squared displacement and temperature. Differences between head and tail proton motions are also small. Above this temperature, localized motion distinct from vibration appears with obvious differences in head and tail mobility. Above the highest temperature on the plot, 340 K, motion is no longer localized and thus its spatial extent may not be extracted. The appearance of non-localized motion, particularly in the lipid tails, is a hallmark of the liquid crystalline state. The mean squared displacements in Fig. 1 are averages over all tail or head group protons. Because these regions of the lipid molecules are connected, the difference in local cage sizes implies that cage size varies with the location of tail protons: those immediately near the head group region must explore smaller cage regions than those at the tail ends. This suggestion is validated with the simulation image provided in the figure inset. The image represents

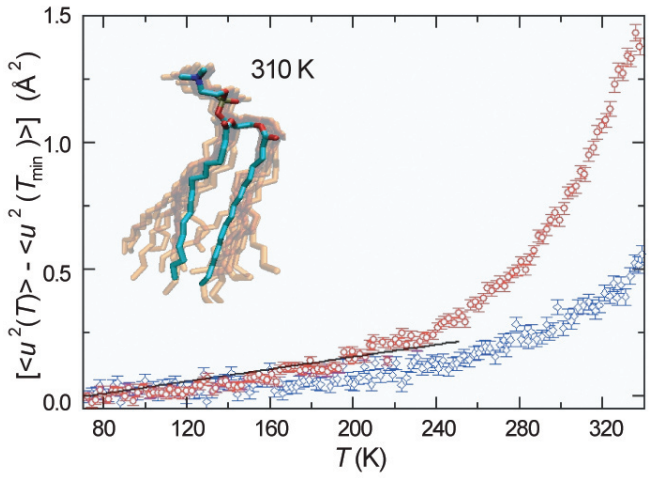

FIGURE 1: The local cage size in tail labeled (dhDPPC, red circles) and head labeled (hdDPPC, blue diamonds) samples referenced to 70 K, the lowest measured temperature. The inset image presents simulation coordinates of a single lipid molecule at 310 K, plotted every 400 ps over a time period of 4 ns.

[1]The University of Wisconsin, Madison, WI 53706
[2]National Institute of Standards and Technology
NIST Center for Neutron Research, Gaithersburg, MD 20899 and
The University of Maryland, College Park, MD 20742
[3]The Pennsylvania State University, University Park, PA 16802
[4]The University of Wisconsin, Madison, WI 53706

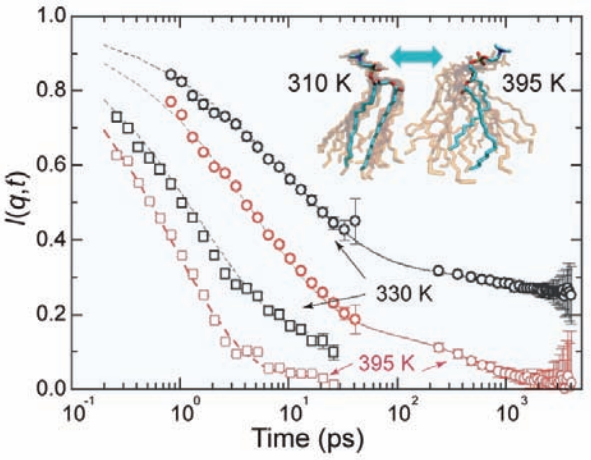

FIGURE 2: Mobility of dhDPPC above (395 K, red symbols) and below (330 K, black symbols) the melting transition. Dynamic data from two instruments (plotted here as the intermediate scattering function) are combined to form a single curve. Squares correspond to motion over a spherical region with diameter of 4 Å, and circles to motion over 7.5 Å. The inset images present simulation coordinates of a single lipid molecule plotted every 400 ps over a time period of 4 ns.

a time progression of a single lipid molecule over an interval approximately equivalent to the instrumental resolution, and demonstrates a variation in spatial exploration with tail position.

The localized motion characterized in Fig. 1 describes states below the melting transition. Since the rapid change in mobility at this transition appears in the tail protons, we focus on the dhDPPC sample, and investigate the associated change in dynamics. This requires characterization of neutron energy changes during scattering, rather than merely the elastic fraction. Because these measurements are more time consuming, only two temperatures, bracketing the transition, are presented in Fig. 2. These spectra consist of two parts which roughly correspond to localized motion observed for times less than 50 ps, and larger scale motion for times greater than 200 ps. Localized motion, the spatial extent of which was characterized above, exists both above and below the melting transition. Larger scale motion only occurs above the melting transition, as indicated by the absence of decay from 200 ps to 4 ns at 330 K. Although the experimental data do not decay enough to clearly identify the nature of this motion, the simulation snapshots suggest that larger scale motion of lipid tails originates from the onset of conformational changes in the head-group regions, and may be rotational in nature.

We focus on localized motion occurring both above and below the melting transition described by data at times less than 50 ps to extract information about the nature and timescale of the motion. Based on analysis of the fixed window scans and simulation snapshots, we expect that motion occurs by exploration of local regions, the size of which varies with location along the lipid tail. Our fitting procedure yields the elastic incoherent structure factor (EISF) of the localized process as a fit parameter, and examination of this variable in comparison to model functions can both confirm localized motion and provide information on its geometry. We choose a model describing motion as diffusion within impenetrable spheres [4]. As confirmed by the comparison in Fig. 2, a single sphere size is insufficient to describe the experimental data. If the sphere radius is allowed to vary with tail position, the same model provides an excellent description of the data. Rather than impose a linear variation of sphere size with tail position, we obtain the variation from our molecular dynamics simulations, where mobility at individual locations may be easily isolated.

Our investigation identifies several important characteristics on a molecular level. Below the melting transition, significant localized mobility is present in the lipid tails, with the spatial extent of this motion growing with temperature well before the transition occurs. The size of the region within which localized motion takes place is not homogeneous, but rather varies with location along the lipid tail. The rapid gain in mobility over the transition from the gel to liquid crystalline phase is observed in the lipid tails, and involves the onset of non-localized motion. This tail motion appears to be enabled by conformational transitions of the head groups at higher temperatures. This molecular picture of melting in dehydrated lipid bilayers provides a baseline against which the behavior of additive modified systems may be compared to determine the mechanism

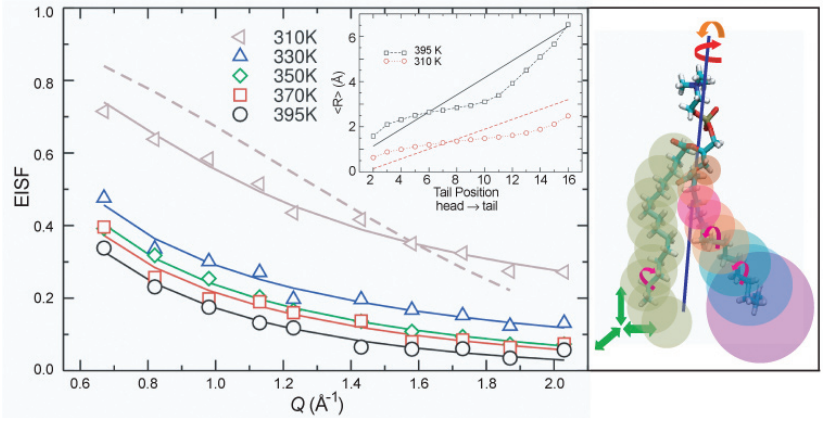

FIGURE 3: Comparison of the EISF extracted from fits to the short-time decay and a model of diffusion within impenetrable spheres. Two versions of model predictions are provided at 310 K. The dashed line uses spheres with a radius independent of tail position, as illustrated in the left lipid tail in the image. The solid line allows the sphere radius to vary with position, as illustrated in the right lipid tail in the image. The radius variation taken from molecular dynamics simulation is provided in the figure inset.

References

[1] J. F. Nagle, Ann. Rev. Phys. Chem. **31**, 157 (1980).
[2] J. H. Crowe, L. M. Crowe, Nature Biotechnol. **18**, 145 (2000).
[3] M. Doxastakis, S. Ohtake, V. García Sakai, J. K. Maranas, J. J. de Pablo, Biophys. J. **92** (1), 147(2007).
[4] L. Carpentier, M. Beé, A. M. Giroud-Godquin, P. Maldivi, J. C. Marchon, Mol. Phys. **68**, 1367 (1989).

Revealing Light-Enhanced Protein Activity with Neutrons

C. T. Lee, Jr., A. C. Hamill, S. C. Wang[1]; A. Faraone[2]

Of all the molecules found in living organisms, proteins are the most important. Enzymes act as catalysts; rhodopsin aids vision and G-protein-coupled-receptors mediate smell and taste. To a large extent, protein function is determined by protein conformation, particularly in the case of enzymes where folding results in an active site that allows for selective binding of substrates. However, the static "lock and key" mechanism has been replaced in modern enzymology with the form-dynamics-function relationship and the view that enzyme dynamics can have an equally important role in catalysis. To directly examine this relationship, the interaction of a photoresponsive surfactant with lysozyme has been investigated as a means to control the enzyme *structure, flexibility,* and *activity* with light illumination. Conformational changes as a function of photoresponsive surfactant concentration and light illumination were measured through shape-reconstruction analysis of small-angle neutron scattering (SANS) data. The SANS-based *in vitro* structures indicate that lysozyme adopts a partially-unfolded conformation in the presence of the photosurfactant under visible illumination, while UV illumination causes the protein to refold to a near-native structure. Protein swelling occurs principally away from the active site near the hinge region connecting the α and β domains, leading to enhanced domain motions that we directly measured with neutron spin echo (NSE). This enhanced enzyme flexibility is accompanied by an 8-fold increase in enzymatic activity relative to the native state, leading to complete photoreversible control of the structure, dynamics, and function of lysozyme.

Azobenzene-based photoresponsive surfactants ("azoTAB", see Fig. 1) have recently been utilized to induce reversible changes in protein conformation with light illumination, with relatively high resolution *in vitro* protein structures determined with small-angle neutron scattering (SANS) [1-4]. A photoisomerization between the visible-light *trans* (relatively hydrophobic) and UV-light *cis* (relatively hydrophilic) forms of the azobenzene moiety allows photocontrol of surfactant interactions with various proteins. With bovine serum albumin, the initial unfolding was localized to the hydrophobic α-helical segments in the C-terminal portion of the protein [1, 3]. In contrast, for α-chymotrypsin consisting primarily of β structures, only small changes in the overall size of the protein were observed (≈ 7 % increase in the radius of gyration), however, this subtle structural rearrangement was sufficient to convert

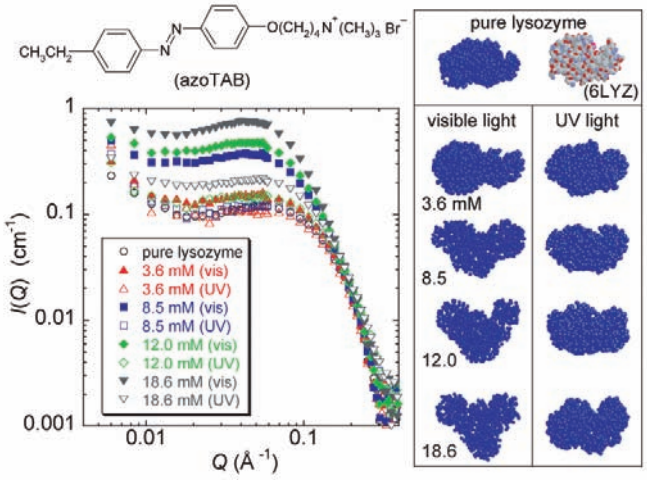

FIGURE 1: SANS data of lysozyme-azoTAB solutions as a function of photosurfactant concentration, along with *in vitro* lysozyme conformations determined from shape-reconstruction analysis of the SANS data. The crystal structure of lysozyme (PDB code 6LYZ) is shown for comparison.

*intra*molecular β structures into *inter*molecular β sheets and lead to eventual amyloid fibril formation [4].

For lysozyme containing both α and β domains, the SANS data in Fig. 1 indicate that the photosurfactant swells lysozyme under visible light (photosurfactant switched "on"), while the protein refolds to a native-like conformation under UV illumination (photosurfactant switched "off"). As previously described [2], shape reconstruction of the SANS data involves approximating the protein as a collection of scattering centers whose positions are adjusted to fit the experimental scattering curve. The resulting conformations of lysozyme are shown in Fig. 1 along with the x-ray crystallographic structure (PDB code 6LYZ). While at low azoTAB concentrations the SANS-based structures are similar to the crystal structure of pure lysozyme, the true utility of SANS is seen at elevated azoTAB concentrations where the degree and location, of protein swelling can be determined. Lysozyme is observed to swell primarily in the lower portion of the molecule away from the active site in the so-called hinge region, which gives rise to a progressively more open active-site cleft.

From these SANS-based *in vitro* conformations, lysozyme activity against glycolchitin was determined as a function of

[1]University of Southern California, Los Angeles, CA 90089
[2]NIST Center for Neutron Research, National Institute of Standards and Technology, Gaithersburg, MD 20899

azoTAB concentration and light conditions, revealing an 8-fold increase in activity (i.e., "superactivity") with lysozyme in the swollen form. In order to form the enzyme-substrate complex, it has been reported that the active-site cleft of lysozyme has to first open (to allow the substrate to enter the active site) and then close (to return the enzyme to a state similar to the native conformation) through hinge-bending motions of the α and β domains. Thus, it may be expected that domain motions play an important role in the catalytic process.

The rates of enzymatic reactions are controlled by the height of the activation energy barrier. Thus, to induce superactivity requires that enzyme flexibility be increased in such a way that transition-state structures are preferentially sampled. With this in mind, the superactivity observed in the presence of azoTAB under visible light could be a result of the higher degree of swelling of the hinge region, which would be expected to lead to enhanced hinge-bending motions. At the ensemble level as in Fig. 1, this is manifested by an overall broadening of the active-site cleft, analogous to regions with high temperature factors (B factors) in x-ray crystallographic structures that are often associated with regions undergoing large thermal motions.

To directly measure protein domain motions, neutron spin echo (NSE) experiments were performed at NIST on lysozyme-photosurfactant systems. While SANS is

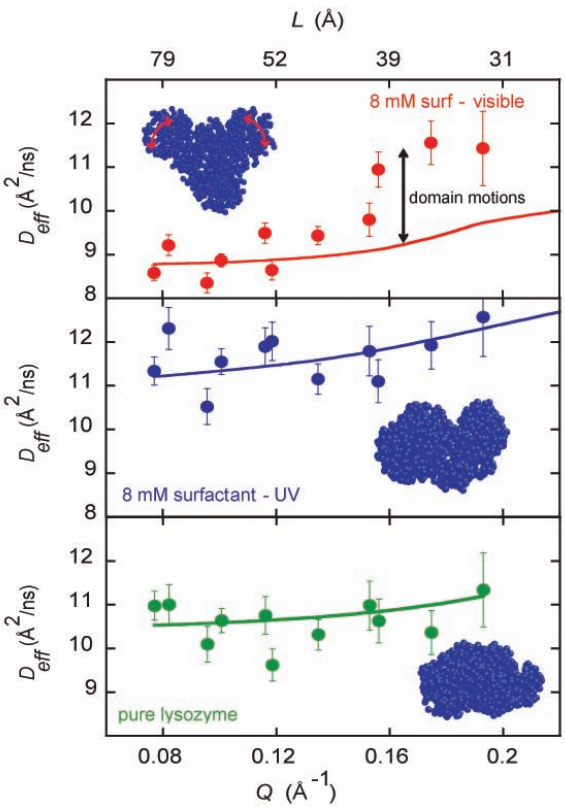

FIGURE 2: NSE measurements of the effective diffusion coefficient of 10 mg/mL lysozyme solutions in the presence of the azoTAB photosurfactant that is active under visible illumination and passive under UV illumination. Solid lines account for rigid-body motions (translation/rotation).

the neutron analogue of static light scattering with both measuring scattering intensity, NSE is analogous to dynamic light scattering, since both measure a diffusion coefficient. In contrast to translational diffusion determined from DLS, however, NSE can further access motions over time scales from 0.01 ns to 100 ns and length scales from 10 Å to 150 Å. As seen in Fig. 2, NSE reveals a deviation in the effective diffusion coefficient from that expected for purely rigid-body motions (i.e., translation plus rotation [5]) in the presence of surfactant activated under visible light, while converting the surfactant to the passive form with UV light results in a "dormant" protein in the nanosecond/nanometer regime, similar to native lysozyme. This deviation is observed as the length scale L (= $2\pi/Q$) decreases to values approaching the protein diameter. Thus, NSE is detecting nanosecond domain motions within the protein. Interestingly, these internal motions occur with the aforementioned 8-fold enhanced "superactivity" of the enzyme versus the native state. Thus, Fig. 2 provides a direct measure of photo-induced protein internal motions leading to enhancements in enzyme activity.

Through combined SANS and NSE measurements, unique insight is obtained into the mechanisms by which photoreversible control of protein structure/flexibility lead to enhanced enzyme activity. The *in vitro* enzyme conformations from SANS reveal that lysozyme swells primarily in the hinge region connecting the α and β domains. This in turn leads to nanosecond/nanometer domain motions within the protein, directly measured with NSE experiments, as well as to an 8-fold increases in enzymatic activity relative to the native state. By examining the complete *form-dynamics-function* triad of lysozyme, these results suggest a general procedure by which enzymatic activity could be increased through enhancements in enzyme flexibility.

ACKNOWLEDGMENTS

This material is based upon work supported by the National Science Foundation under Grant No. 0554115.

References

[1] C. T. Lee, Jr., K. A. Smith, T. A. Hatton, Biochemistry **44** (2), 524 (2005).

[2] A. C. Hamill, S-C. Wang, C. T. Lee, Jr., Biochemistry **44** (46), 15139 (2005).

[3] S-C. Wang, C. T. Lee, Jr., J. Phys. Chem. B **110** (32), 16117 (2006).

[4] A. C. Hamill, C. T. Lee, Jr., Biochemistry **46** (26), 7694 (2007).

[5] Z. Bu, R. Biehl, M. Monkenbusch, D. Richter, D. J. E. Callaway, PNAS (USA) **102** (49), 17646 (2005).

Extending Neutron Activation Analysis Capabilities

B. E. Tomlin, R. Zeisler, R. M. Lindstrom[1]

Trace elements play an important role in everyday life. Many of the high-tech devices that modern society relies upon require high-purity raw materials for their manufacture, and the content of trace elements in these materials can have a significant effect on their properties. In biological systems, trace elements play two roles—as essential nutrients for an organism's survival and as toxic substances that can cause disease and death at extremely low concentrations. Given the critical role of trace elements, the characterization of trace element compositions in a wide variety of materials is crucial for advancements in science, industry and medicine.

Neutron activation analysis (NAA) is a powerful method for the determination of a wide variety of trace elements, independent of the chemical environment of those elements. NAA is based on the measurement of nuclear gamma radiations. The technique of gamma-gamma ($\gamma\gamma$) coincidence spectrometry is a means of counting γ rays with a much higher level of discrimination by distinguishing radioactive decay events with unique signatures from the much larger number of all other decay events. Nuclear spectroscopists commonly employ $\gamma\gamma$ coincidence techniques, but this technique is not widely used within the nuclear analytical community. Early work on the use of $\gamma\gamma$ coincidence measurements as a means of improving the sensitivity of NAA for rare earth elements was reported in the literature almost forty years ago [1]; however, little development of the technique has occurred since then. New trends in instrumentation, however, promise greater improvements than have been achieved in the past.

In order to fully explore the use of $\gamma\gamma$ coincidence NAA in characterizing standard reference materials (SRM), a prototype $\gamma\gamma$ coincidence spectrometer, as shown in the inset of Fig. 1b, has been constructed at the NIST Center for Neutron Research using high-purity germanium γ-ray detectors and state-of-the-art digital instrumentation. This system will extend to quantitative analyses the general approaches used by nuclear spectroscopists employing state-of-the-art signal processing procedures.

Gamma-ray spectra with significant reductions in background components have been attained with the coincidence spectrometer at NIST. Figure 1 illustrates the effect of coincidence gating on a γ-ray spectrum. Figure 1a shows a portion of an ungated, conventional singles γ-ray spectrum for SRM 1598a Animal Serum, with the Cs-134 605-keV peak labeled. In contrast, Fig. 1b shows a coincidence γ-ray spectrum, gated on the Cs-134 796-keV transition, over the same energy range as Fig. 1a.

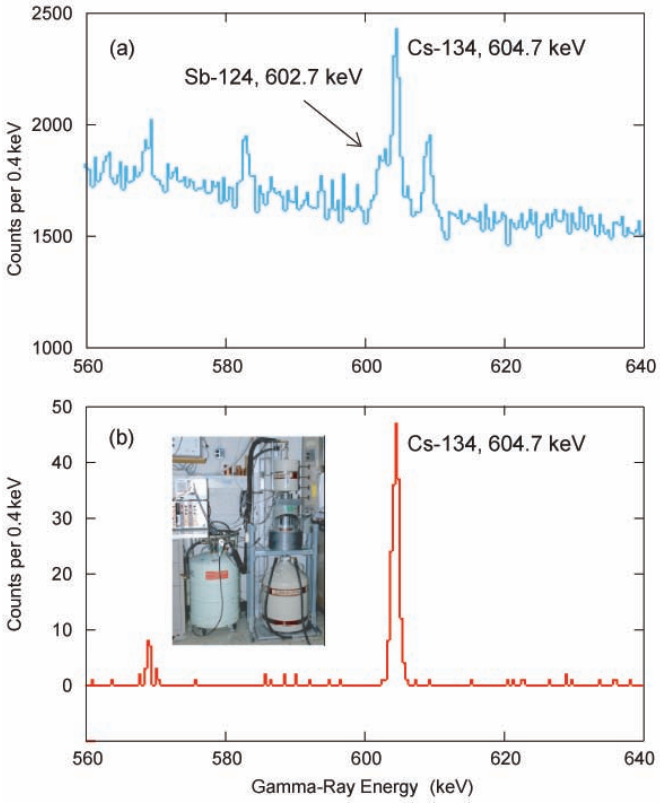

FIGURE 1: Inset: the NIST prototype $\gamma\gamma$ coincidence spectrometer. (a) A representative singles γ-ray spectrum. (b) A representative γ-ray gated coincidence spectrum.

The coincidence spectrum demonstrates both a reduction in the overall spectral background, as well as, the elimination of the overlapping Sb-124 γ-ray peak which causes the distorted peak shape in Fig. 1a.

The application of $\gamma\gamma$ coincidence spectrometry to NAA here at NIST will extend our capabilities for quantifying trace elements in a broad array of reference materials and other critical samples. The newly constructed prototype $\gamma\gamma$ coincidence spectrometer has been found to provide significant enhancements in γ-ray counting sensitivity and selectivity. Based on these positive results, it is fully expected that $\gamma\gamma$ coincidence NAA will make a considerable contribution to the Analytical Chemistry Division's SRM program. Work is presently underway employing the coincidence spectrometer to characterize a number of trace elements in a new bovine liver SRM.

References

[1] W. D. Ehmann and D. M. McKown, Anal. Lett. **2**, 49 (1969).

[1]Analytical Chemistry Division, National Institute of Standards and Technology, Gaithersburg, MD 20899

Reciprocal Space Neutron Imaging

D. A. Pushin and D. G. Cory[1]; M. Arif and D. L. Jacobson[2]; M. G. Huber[3]

Here we describe an interferometric method for coherent, reciprocal space neutron imaging which overcomes the spatial resolution limitations of existing neutron imaging methods based on position sensitive detectors. The method implements a spatial encoding of the neutron phase similar to that used in nuclear magnetic resonance imaging. By moving neutron imaging from real to reciprocal space we avoid the need for position sensitive detectors and improve the potential image resolution. Neutron imaging is complementary to other noninvasive imaging methods, such as x-ray imaging and magnetic resonance imaging. Neutrons are transparent to many high Z-number materials and are scattered by many light elements, primarily hydrogen. Examples of neutron imaging include density fluctuations of hydrogen in metals, density of polymeric overlayers, formation of water in hydrogen fuel cells, crystallography for structural biology, and magnetic domain distributions.

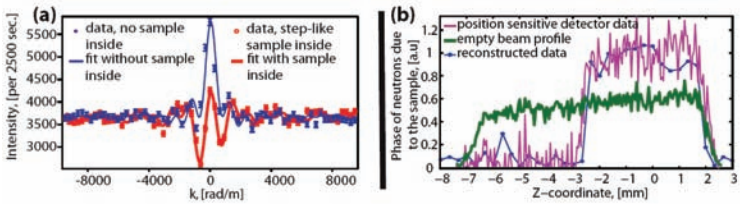

FIGURE 2: Step-like sample data. The sample is a thin (25 μm) fused silica slab that covers only part of the neutron beam. On the left (a) we show raw data with the sample (open red circles) and without the sample (filled blue circles). Reconstructed images are shown on the right (b). Open blue circles represent reconstructed image of the step-like sample, the purple line is the1D image of the sample obtained with a position sensitive detector, and the green dashed line is the beam profile on the position sensitive detector without a sample.

The essence of the reciprocal space measurement is to create in one leg of the interferometer a spatial linear phase grating with a controllable wave-number. Such a grating in the neutron phase over the neutron beam can be created by placing a prism in one leg of the interferometer as shown in Fig. 1. If a sample is placed in the second leg of the interferometer then the observed contrast will be dependent on the Fourier coefficient of the spatial distribution of the coherent cross-section of the sample at the wave-number selected by the grating. Since the grating wave-number is experimentally controllable we can map out the full reciprocal space description of the sample. This is easily and directly invertible to recover the image of the sample [1]. The method does not require a 2-D detector and thus has the potential to improve the spatial resolution significantly compared to the current limit of tens of micrometers. From the Nyquist theorem, the image resolution depends on the maximum measured wave number, $|\Delta r| = \pi/|k_{max}|$.

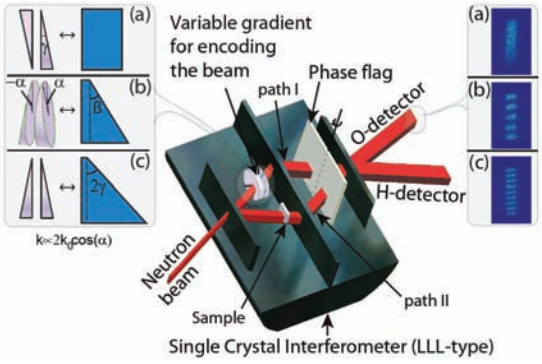

FIGURE 1: Schematic diagram of imaging experiment at NIST. A neutron beam, coming from the left, is coherently divided via Bragg diffraction in the first blade of the neutron interferometer into two beams. These beams travel along paths I and II. The phases which the neutron accumulates over each path are experimentally controlled by rotating the phase flag, which changes the optical path length due to the flag. After diffraction at the second blade these beams coherently recombine at the third blade and proceed to the O- or H- detector. In insets a, b and c are shown the wedges used to create a phase grating across the neutron beam and the corresponding images from a position sensitive detector. Each wedge is positioned perpendicular to the beam and produces gradients: $\boldsymbol{k}_{1,2} = \boldsymbol{z}k_0\cos\alpha_{1,2} + \boldsymbol{y}k_0\sin\alpha_{1,2}$, where k_0 is the maximal gradient which each wedge can produce in the vertical direction and α_1, α_2 - angles of rotation of the wedge around the neutron beam path. To create only vertical gradients we counter-rotate these two wedges: $\boldsymbol{k}_{tot} = \boldsymbol{k}_1 + \boldsymbol{k}_2 = 2\boldsymbol{z}k_0\cos\alpha$ ($\alpha_1 = -\alpha_2 = \alpha$), so the realizable vertical gradients vary from $-2k_0$ to $2k_0$. For imaging, the position sensitive detector is replaced by more sensitive ^{3}He detectors.

To achieve 5 μm resolution we need to use a maximum gradient of the order of 6.3×10^5 rad m^{-1} or a fused silica wedge with an 81° wedge angle. In our case the maximum gradient (2×10^4 rad m^{-1}) was produced by two 6° wedges corresponds to a resolution of 160 μm.

Figure 2 shows an example 1-D image of a step-like sample that reveals the resolving power of the method. The sample partially covers the top of the beam. On the left (a) we report the raw data and on the right (b) the reconstructed and measured images. The smooth curve in (a) is the best fit for the known step-like sample shape. The excellent quality of the data mirrors the quality of the beam characteristics (profile, momentum spread and divergence). Extensions of the method to 2-D are easily accomplished by rotating the sample or by rotating the grating [2].

References

[1] D. A. Pushin, M. Arif, D. L. Jacobson, C. K. Do, and D. Cory, Physica B **385-386**, 1402 (2006).

[2] D. A. Pushin, M. Arif, D. L. Jacobson, M. G. Huber, and D. Cory, Appl. Phys. Lett. **90**, 224104 (2007).

[1]Massachusetts Institute of Technology, Cambridge, MA 02139
[2]NIST Center for Neutron Research, National Institute of Standards and Technology, Gaithersburg, MD 20899
[3]Department of Physics, Tulane University, New Orleans, LA 70118

^{3}He Spin Filters for Polarized Neutron Scattering Experiments

W. C. Chen[1], J. A. Borchers[1], Y. Chen[1], R. Erwin[1], S. McKenney[1], I. Cabrera[1,2], C. Broholm[2], M. Kenzelmann[3], T. R. Gentile[4], and J. W. Lynn[1]

Polarized neutron scattering is a powerful probe for a wide range of research fields from physics to biology. Many of the newest neutron scattering spectrometers have increased beam angular divergences or wavelength bandwidths in the interest of larger on-sample neutron fluxes and increased detectable signal, but this has made it difficult to apply the standard techniques for polarized beam production and analysis using reflecting Heusler crystals or super-mirrors. This problem is now being solved using ^{3}He neutron spin filters (NSFs). These filters employ nuclear-spin-polarized ^{3}He gas, produced by optical pumping, and can be used to polarize or analyze neutron beams because of the strong spin dependence of the absorption cross section for neutrons by ^{3}He. Due to significant improvement in their performance during the last several years, including initial ^{3}He polarizations exceeding 70%, the use of NSFs has grown in the neutron scattering community worldwide. Compared to commonly used polarizers such as supermirrors and Heusler crystals, NSFs have these advantages: 1) they can polarize a broad wavelength band of neutrons effectively; 2) they can polarize large area and widely divergent neutron beams; 3) they are in-line add-on devices and 4) they can efficiently flip the neutron polarization by reversing the ^{3}He nuclear polarization [1]. This last capability allows integrating polarizer and flipper into a single device.

Building upon several years of research and development in the Physics Laboratory at NIST together with outside collaborations, the NCNR initiated a program in 2006 to support polarized neutron beam experiments using ^{3}He neutron spin filters. The goal of the program is to polarize and/or analyze beams for neutron scattering instruments where other neutron-polarizing techniques are inadequate. This goal has been met by applying polarized ^{3}He NSF devices to diffuse reflectometry [2], small-angle neutron scattering (SANS) [3], and thermal triple-axis spectrometry (TAS) [4].

For thermal TAS, ^{3}He spin filters in conjunction with a double focusing monochromator and analyzer can provide significantly better neutronic performance and greater versatility in the selection of energy and polarization compared to Heusler crystals. We have successfully performed several polarized beam experiments on the state-of-the-art BT-7 TAS using ^{3}He NSFs to polarize and analyze a 10 cm tall neutron beam. The general case involves measuring eight cross sections, four with incoming neutron polarization perpendicular to the momentum transfer wave vector Q and four parallel.

Figure 1 shows a result just obtained on this instrument for a multiferroic system—a material that is both magnetically ordered and ferroelectric. A recent important discovery in condensed matter physics is that magnetic ordering can actually induce ferroelectricity, for example when the magnetic order parameter breaks polar inversion symmetry. In such magnetoelectric materials it is anticipated that there are two distinct domains of magnetic order, each carrying opposite ferroelectric polarization. But how is one to distinguish these magnetic domains, which should be mirror images of one another?

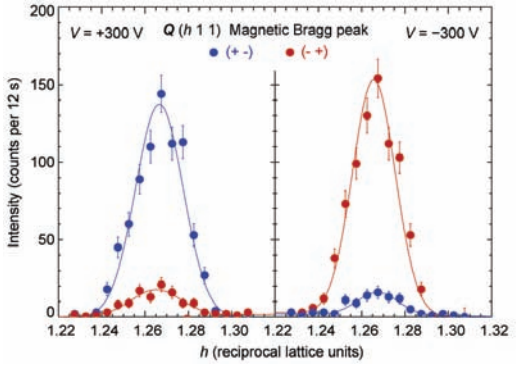

FIGURE 1: Magnetic Bragg scattering from $Ni_3V_2O_8$ is identified because the neutron spin reverses its direction upon scattering. One set of data is taken with the incident neutron spins parallel to the momentum transfer, (+, -), the other set of data is taken with the incident neutron spins antiparallel, (-, +). The direction of the ferroelectric domain is selected by applying a voltage of either +300 V or -300 V. The change in the character of the magnetic scattering with electric voltage directly and unambiguously demonstrates that the chiral magnetic order and the direction of the ferroelectricity are intimately linked in this multiferroic material.

Polarized neutrons are the answer. Each magnetic domain should have a definite handedness and this implies that diffraction from a single domain should polarize the neutron beam. Figure 1 shows that this is indeed the case for the magnetoelectric material $Ni_3V_2O_8$. Upon applying electric fields in opposite directions, opposite polarization conditions were indeed associated with the corresponding magnetic diffraction. This essential information about an important class of materials could only be obtained through the use of polarized neutrons.

For these experiments, the ^{3}He nuclear polarization is initially above 70 % and is stored in a very homogeneous field provided by a magnetically shielded solenoid. The decay time constant for an isolated cell is typically 300 h, which was the case for the analyzer, but due to stray magnetic field gradients the time constant at the polarizer was 140 h. We typically refresh polarized ^{3}He gas after 1 or 2 days on the beam line.

For polarization analysis in diffuse reflectometry, the ^{3}He spin filter allows much more efficient collection of off-specular scattering for a broad range of reciprocal space. The use of a ^{3}He spin filter makes polarization analysis practical in SANS. A recent experiment on a magnetic nanoparticle system showed full polarization analysis in SANS can be done using a ^{3}He spin filter as both spin analyzer and spin flipper. User-friendly data reduction software is also under development to interface with these ^{3}He NSFs.

References

[1] G. L. Jones *et al.*, Physica B **385-386**, 1131 (2006).
[2] W. C. Chen *et al.*, Rev. Sci. Instrum. **75**, 3256 (2004).
[3] T. R. Gentile *et al.*, J. Appl. Cryst. **33**, 771 (2000).
[4] W. C. Chen *et al.*, Physica B, Physica B **397**, 168 (2007).

[1]NIST Center for Neutron Research, National Institute of Standards and Technology, Gaithersburg, MD 20899
[2]Johns Hopkins University, Baltimore, MD 21218
[3]Swiss Federal Institute of Tchnology (ETH), Zurich, Switzerland
[4]Physics Laboratory, National Institute of Standards and Technology, Gaithersburg, MD 20899

Trace Fissionable Material Analysis: New Metrology Facility

R. M. Lindstrom, R. G. Downing[1]

Detecting clandestine fissile material like U-235 and Pu-239 is technically challenging in the lab or in the field because it emits little radiation, and that radiation is energetically weak. Shipments are easily concealed and very difficult to detect by conventional methods. However, when these materials are handled or transported, traces of uranium or plutonium in the form of particles smaller than grains of pollen can be left behind. Inspectors for the International Atomic Energy Agency (IAEA) have used wipe-cloth collection techniques to search for such evidence of handling and transport of clandestine treaty-monitored fissile materials. One of the most sensitive forensic techniques used to detect and measure the minute remnants of fissionable uranium and plutonium on these wipes is delayed neutron activation analysis (DNAA) (see cartoon above). DNAA works with excellent speed, sensitivity, and specificity, but few such systems exist worldwide. Overall, DNAA is well-tested, rapid, specific, matrix-independent, nondestructive, and sensitive. The technique is sensitive solely to nuclides that fission with delayed emission of neutrons to give an unambiguous indication of controlled material, e.g., ^{233}U, ^{235}U, ^{239}Pu, ^{241}Pu, ^{241}Am, ^{243}Cm, ^{244}Cm, ^{245}Cm, ^{252}Cf.

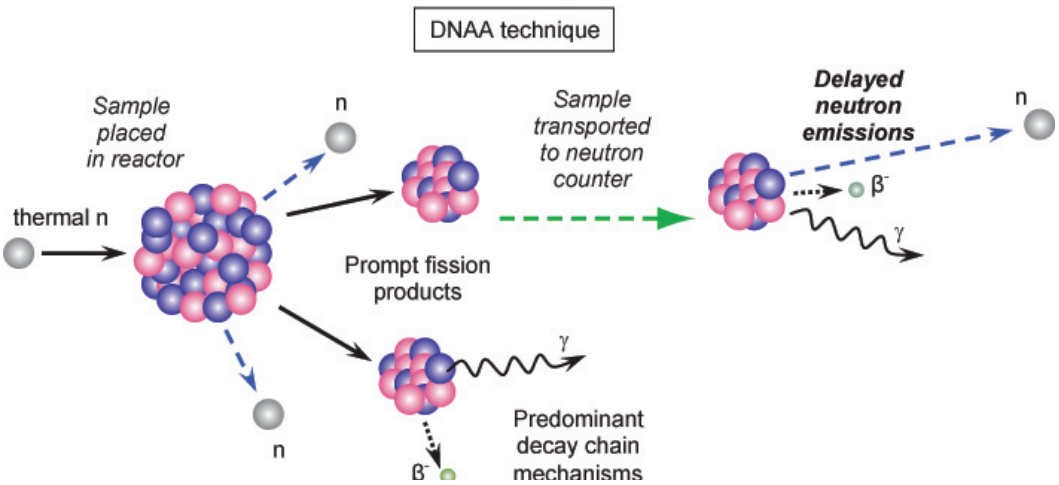

The Nuclear Methods Team in the Analytical Chemistry Division (ACD) recently installed a DNAA system at the NCNR. NCNR is an excellent facility to take advantage of this analytical method because of the intense thermal flux available with a minimal proportion of fast neutrons. These highly desirable characteristics mean that interference from fast-neutron reactions produced from the ubiquitous presence of thorium and oxygen are negligible. Consequently, the analysis process is greatly simplified and detection limits enhanced. At the NIST DNAA facility, less than one nanogram of fissile species can be detected, and the analysis requires less than 3 min. Furthermore the system can process a great variety of sample types that might host the fissionable particles hidden in volumes as large as 40 mL.

In the last year researchers from Oak Ridge National Laboratory (ORNL) and our team successfully demonstrated that the newly installed DNAA system response is strictly linear over at least a 25-fold concentration range of ^{235}U (Fig. 1). This demonstrated ability enabled the system to immediately be used for the analyses of samples from ORNL.

Just recently, the sample transfer system was automated, leading to increased sample throughput and improved sensitivity. As the technique is further developed it will be used to certify the trace uranium for reference materials and standard reference materials. With the completion and verification of the DNAA system, NIST has a readily accessible, rapid means of measuring traces of fissionable U and Pu in samples of forensic interest for homeland security and producing standard reference materials.

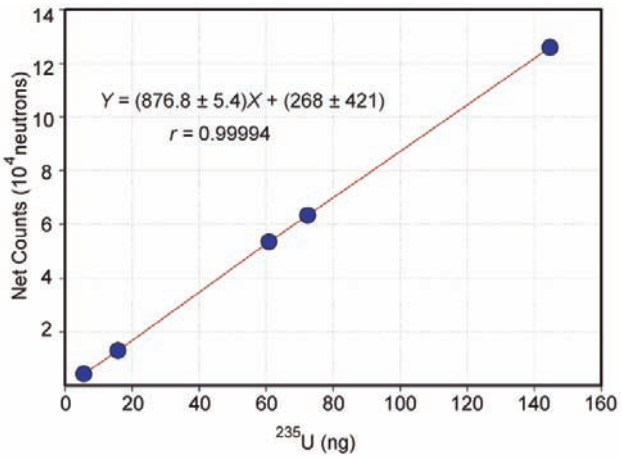

FIGURE 1: Plot of neutrons detected in the DNAA counter following 1 min irradiations as a function of uranium content in the standards.

[1]Analytical Chemistry Division, National Institute of Standards and Technology, Gaithersburg, MD 20899

Direct Measurement of the Vertical Coherence Length of Neutron Waves

D. A. Pushin and D. G. Cory[1]; M. Arif, D. L. Jacobson and D. S. Hussey[2]; M. G. Huber[3]

The coherence length in a neutron interferometer system describes the spatial extent over which quantum interference may be preserved for the interfering neutron beams. Increases in the coherence length improve the fringe visibility (contrast), thus increasing the precision of a measurement. In addition, longer vertical coherence lengths in neutron interferometry may allow useful implementations of Fourier Spectroscopy and reflectivity, with applications in condensed matter and biology [1].

In a neutron interferometer the measured coherence length is affected by the quality of the single crystal, the momentum distribution of the incoming neutron beam, and a variety of environmental contributions such as temperature gradients and vibrations. In this experiment we have explored the vertical coherence length in a system that is primarily determined by the incoming beam's transverse momentum spread. When this is the case, the coherence length (l_c) is limited by Heisenberg's uncertainty relation $l_c = 1/(2\delta k)$, where δk is momentum spread. To understand this limit, we study the contrast associated with a wave-packet composed of incident plane waves corresponding to a distribution of neutron transverse momentum components varied by selecting monochromator blades. The coherence length is a direct measurement of the transverse spatial extent of this wave-packet.

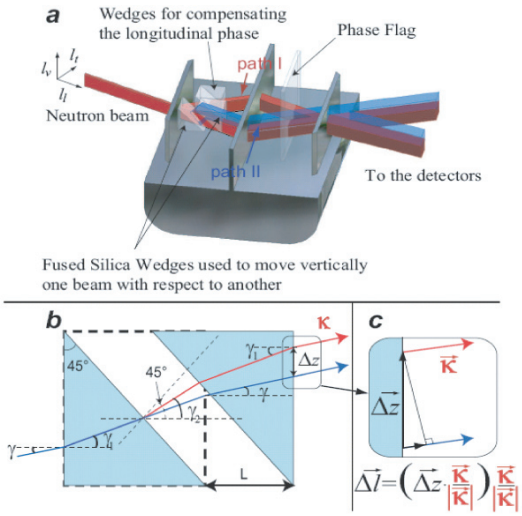

FIGURE 1: (a) A neutron beam, entering at left, is coherently divided via Bragg diffraction on the 1st blade of the neutron interferometer into paths I and II. The phases which the neutron accumulates over each path are experimentally controlled by rotating the phase flag. (b) In one of the paths we install two 45° prisms which form a cube when unseparated. By horizontally separating the prisms by L we shift the neutron beams in paths I and II vertically (Δz) with respect to each other. We observe a loss in contrast with displacement, which we measure with the help of phase shifter (shown in (a)). (c) Enlarged view of the neutron beam as it exits the prism.

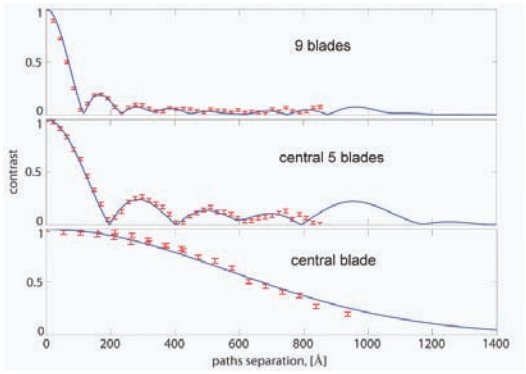

FIGURE 2: (a) the contrast with all nine Bragg reflecting pyrolitic graphite crystal blades of a focusing monochromator (not shown) contributing to the incident beam; (b) the contrast for the central five blades; and (c) the contrast for the central blade. The contrast length increases as we narrow the momentum distribution of the incoming neutron beam by reducing the number of blades. Notice that in the narrowest case the contrast remains up to 100 nm vertical separation of the beam paths. The solid lines are contrast curves obtained by approximating the wave-function of the neutrons as a plane wave and integrating over the vertical momentum distribution.

Measurements for the nine, five, and only the central blade configurations give us 0.70 nm, 1.2 nm, and 65 nm vertical coherence lengths, respectively, that are related to the vertical components of the momentum distributions of the incoming beams. In our measurement the coherence length is directly obtained by a simple projection and does not require any post-selection analysis used in earlier measurements done elsewhere [2].

References

[1] H. Rauch, Physica B **213-214**, 830 (1995).
[2] H. Rauch, H. Wölwitsch, H. Kaiser, R. Clothier, and S. A. Werner, Phys. Rev. A **53**, 902 (1996).

[1]Massachusetts Institute of Technology, Cambridge, MA 02139
[2]Physics Division, National Institute of Standards and Technology, Gaithersburg, MD 20899
[3]Tulane University, New Orleans, LA 70118